Izrada simulacijskog modela motora sa unutarnjim izgaranjem sa asinkronim starter motorom-generatorom u hibridnom električnom vozilu

Plavac, Filip

Master's thesis / Diplomski rad

2020

Degree Grantor / Ustanova koja je dodijelila akademski / stručni stupanj: **University of Zagreb, Faculty of Mechanical Engineering and Naval Architecture / Sveučilište u Zagrebu, Fakultet strojarstva i brodogradnje**

Permanent link / Trajna poveznica: https://urn.nsk.hr/urn:nbn:hr:235:979499

Rights / Prava: Attribution 4.0 International/Imenovanje 4.0 međunarodna

Download date / Datum preuzimanja: **2024-03-29**

Repository / Repozitorij:

Repository of Faculty of Mechanical Engineering and Naval Architecture University of Zagreb







UNIVERSITY OF ZAGREB
FACULTY OF MECHANICAL ENGINEERING AND NAVAL ARCHITECTURE

MASTER'S THESIS

Filip Plavac

Zagreb, 2020

UNIVERSITY OF ZAGREB
FACULTY OF MECHANICAL ENGINEERING AND NAVAL ARCHITECTURE

MASTER'S THESIS

Mentor:

Assoc. Prof. Danijel Pavković, PhD

Student:

Filip Plavac, BSc

Zagreb, 2020

IZJAVA

Izjavljujem da sam ovaj rad izradio samostalno koristeći znanja stečena tijekom studija i navedenu literaturu.

STATEMENT

I state that this thesis was made by my own effort utilizing on the knowledge obtained during my studies and the referenced literature.

ZAHVALA

Srdačno se zahvaljujem profesoru dr. sc. Danijelu Pavkoviću na prihvaćanju mentorstva, te korisnim savjetima i ispravkama koje mi je pružio tijekom izrade ovog rada. Također, zahvaljujem se mr. sc. Borislavu Klarinu na pruženoj prilici za pisanje diplomskog rada u tvrtki AVL – AST d.o.o., kao i mag. ing. mech. Marinu Miletiću, te mr.sc. Josipu Hozmecu na pruženoj pomoći.

Iskrenu zahvalu dajem svojoj majci Željki, ocu Mariu i bratu Josipu na njihovoj cijeloživotnoj potpori.

Konačno, zahvaljujem se svojoj djevojci Antoneli na lijepim riječima koje su me motivirale.

Filip Plavac

ACKNOWLEDGEMENT

I would like to wholeheartedly thank Assoc. Prof. Danijel Pavković, PhD for taking me under his mentorship and for the useful advice and corrections he has given me during the making of this master's thesis. Furthermore, I would like thank Borislav Klarin, MPhil for the opportunity to make this master's thesis within the company AVL – AST d.o.o. and to Marin Miletić, MSc, as well as to Josip Hozmec, MPhil for the assistance they have provided me with.

The sincere acknowledgment goes to my mother Željka, my father Mario and my brother Josip for their lifelong support.

Finally, I would like to thank my girlfriend Antonela for the kind words that have motivated me.

Filip Plavac

SVEUČILIŠTE U ZAGREBU
FAKULTET STROJARSTVA I BRODOGRADNJE
Središnje povjerenstvo za završne i diplomske ispite
Povjerenstvo za diplomske radove studija strojarstva za smjerove:
proizvodno inženjerstvo, računalno inženjerstvo, industrijsko inženjerstvo i menadžment, inženjerstvo materijala te mehatronika i robotika

Sveučilište u Zagrebu Fakultet strojarstva i brodogradnje	
Datum:	Prilog:
Klasa: 602 - 04 / 20 - 6 / 3	
Ur. broj: 15 - 1703 - 20 -	

DIPLOMSKI ZADATAK

Student: **FILIP PLAVAC** Mat. br.: 0035202879

Naslov rada na hrvatskom jeziku: **Izrada simulacijskog modela motora s unutarnjim izgaranjem s asinkronim starter motorom – generatorom u hibridnom električnom vozilu**

Naslov rada na engleskom jeziku: **Simulation model design for an internal combustion engine using induction motor starter – generator in a hybrid electric vehicle**

Opis zadatka:

Vehicle power-train hybridization is an effective measure to minimize road vehicle CO2 emissions. A relatively simple and cost-effective solution is based on a 48V electrical system utilizing an induction motor (BSG or belt starter generator) coupled via a timing belt to the internal combustion engine (ICE) crankshaft, as an integral part of the FEAD (front end accessory drive) system of a P0 hybrid vehicle used for ICE start-up, torque boosting, and kinetic energy recovery. The tasks of this master's thesis are as follows:
1) Describe the power-train of a hybrid vehicle in P0 configuration with emphasis FEAD system components.
2) Derive induction motor mathematical model and couple it with the FEAD two-mass elastic model comprising BSG rotor and the ICE crankshaft inertias, and implement the overall model in MATLAB/Simulink. BSG speed control system aimed at mitigating timing belt vibrations should be designed.
3) Design the more precise FEAD two-mass elastic model with a larger number of specialized discrete elements in AVL EXCITE Timing Drive multi-body dynamics simulation environment, and test the performance of the control system designed in 2) within EXCITE Timing Drive model. Performance testing is to be carried out by co-simulation between EXCITE and Matlab.
4) Integrate the BSG and control system models from Matlab into the existing model of a P0 hybrid vehicle using AVL CRUISE M system simulation environment by means of FMU (Functional Mock-up Unit) compiled co-simulation model using a standardized interface, with BSG torque transferred to the ICE crankshaft by means of rigid coupling.
5) Derive timing belt equivalent stiffness and damping in the FEAD model designed in 3) and parameterize the BSG rotor vs. ICE crankshaft elastic coupling in CRUISE M simulation. Compare the speed responses from the Matlab/Simulink and EXCITE Timing Drive model.
Student should note any help received during work on the thesis and literature used.

Zadatak zadan:	Rok predaje rada:	Predviđeni datum obrane:
5. ožujka 2020.	7. svibnja 2020.	11. svibnja do 15. svibnja 2020.

Zadatak zadao: Danijel Pavković

prof. dr. sc. Danijel Pavković

Predsjednica Povjerenstva:

prof. dr. sc. Biserka Runje

CONTENTS

CONTENTS I
LIST OF FIGURES IV
LIST OF TABLES IX
LIST OF SYMBOLS AND UNITS X
LIST OF ABBREVIATIONS XVIII
Sažetak XIX
Summary XX
Prošireni sažetak i
1. INTRODUCTION 1
1.1. Transport emissions in Europe 1
1.2. Passenger car emissions 2
1.3. Road to electrification 3
1.4. Hybrid vehicle functions 4
1.4.1. Engine idle stop/start 4
1.4.2. Electric torque assistance 5
1.4.3. Energy recuperation 6
2. 48V P0 MILD HYBRID 8
2.1. Reasons to opt for a 48V system 8
2.2. 48V electrical architecture 8
2.3. FEAD 10
3. ASYNCHRONOUS (INDUCTION) MOTOR 12
3.1. Principle of operation 12
3.2. Speed – torque curve of an induction motor 13
3.3. Induction motor types for BSG application 14
3.3.1. Slip – ring claw – pole induction motor 14

3.3.2. Squirrel – cage induction motor 15
4. MATHEMATICAL MODEL OF BSG AS A SQUIRREL-CAGE MACHINE 17
4.1. Vector control 17
4.1.1. Clarke transformation 19
4.1.2. Park transformation 21
4.1.3. Putting the significance of vector control into context by using an analogy with the DC machine 22
4.2. Mathematical model of BSG in its natural coordinate system 24
4.3. Mathematical model of BSG suitable for vector control 29
4.3.1. Transformation of BSG phase variables into space vectors 29
4.3.2. Transformation of BSG variables expressed as space vectors into a shared coordinate system 30
4.3.3. Voltage source inverter (VSI) 34
4.3.4. Decomposition of the BSG stator voltage model into its d and q components .. 35
5. DESIGN OF THE CONTROL SYSTEM FOR MITIGATION OF FEAD BELT VIBRATIONS 39
5.1. VSI fed squirrel-cage induction machine control scheme 39
5.2. Synthesis of BSG speed and current control system parameters 42
5.2.1. An introduction to the transfer function concept and pole placement method ... 42
5.2.2. Damping optimum criterion 44
5.2.3. Synthesis of BSG dq currents control system parameters 48
5.2.4. FEAD MATLAB model 51
5.2.5. Synthesis of BSG speed control system parameters 54
5.2.6. ICE crankshaft main bearing friction torque 57
5.3. Simulation results 61
5.3.1. Simulation results using the FEAD model with torsional dynamics of the belt 61
5.3.2. Comparison with the response of the system using the FEAD model with longitudinal dynamics of the belt 66

6. AVL EXCITE ™ FEAD MODEL 68
6.1. AVL EXCITE ™ 68
6.2. EXCITE ™ Timing Drive FEAD model 69
6.3. MATLAB cosimulation setup 74
6.4. EXCITE ™/MATLAB cosimulation results 77
7. AVL CRUISE ™ M SYSTEM SIMULATION 81
7.1. AVL CRUISE ™ M 81
7.2. CRUISE ™ M P0 hybrid vehicle model 84
7.2.1. The vehicle 84
7.2.2. The driveline 84
7.2.3. Driver and cockpit 86
7.2.4. Driving regimes 87
7.2.5. Stop/start and boost control logic 88
7.2.6. CRUISE ™ M simulation results 90
7.3. CRUISE™ M P0 hybrid vehicle model with elastic coupling between the BSG and the ICE 96
8. CONCLUSION 102
Bibliography 104

LIST OF FIGURES

Fig. 1 GHG Emissions per sector (left) and emission percentage of components making up the transport sector [1] 1
Fig. 2 Reduction of CO_2 in passenger cars by EU member state 2001 – 2017 [3]. 2
Fig. 3 Hybridization levels with corresponding electrification architectures [4] 3
Fig. 4 Renault 1.6 dCi engine equipped with a 12V electrical machine [5] 5
Fig. 5 Shifting and offsetting of the operating point of an ICE 6
Fig. 6 Hybrid vehicle power flow in recuperation mode 7
Fig. 7 48V electrical architecture in P0 configuration [7]. 9
Fig. 8 Decoupling tensioner positions according to BSG operation mode and tensioner types [9]. 10
Fig. 9 48 V induction BSG [7]. 12
Fig. 10 Induction motor speed - toque curve 13
Fig. 11 HECPG [14] 15
Fig. 12 Squirrel-cage induction motor 16
Fig. 13 Three-phase currents 18
Fig. 14 Resulting space vector of phase currents (8),(9),(10) 19
Fig. 15 Resulting space vector f as a vector sum of its 3-phase and 2-phase space variables 20
Fig. 16 Space vector f and its components in stationary and rotating 2-phase coordinate systems 21
Fig. 17 Armature and excitation circuit of a DC machine 22
Fig. 18 Induction machine in 3-phase coordinate system 24
Fig. 19 Rotating dq system synchronized with the rotor flux space vector ψr 30
Fig. 20 Bi-directional VSI 34
Fig. 21 PT_1 system response 34
Fig. 22 Control scheme based on VSI fed BSG [15] 39
Fig. 23 Scheme of the cascade BSG control structure and its mathematical model in rotating dq coordinate system 41
Fig. 24 Virtual d and q coils represented by their respective transfer functions 42
Fig. 25 BSG torque and FEAD dynamics represented by a tranfer function $GBSG, FEADs$ .. 43

Fig. 26 s-plane with the optimal damping line defined by the coefficient of relative damping $\zeta = 22$ 44
Fig. 27 Block diagram of a linear system described by transfer function (5.8) 44
Fig. 28 Arbitrary closed loop 45
Fig. 29 Subloop from figure 27 46
Fig. 30 Transformed subloop from figure 27 46
Fig. 31 Influence of different values of characteristic ratios Di to the response of a system with the damping optimum characterstic polynomial 47
Fig. 32 BSG current contol loop scheme 48
Fig. 33 Current control subloop block diagram 48
Fig. 34 Current control loop for quasi-continuous approach to controller parameter synthesis 49
Fig. 35 Response of the torque current control system tuned according to damping optimum 50
Fig. 36 Two-mass approximation of FEAD 51
Fig. 37 Scheme of the FEAD model with the longitudinal dynamics of the timing belt and its torsional equivalent 51
Fig. 38 FEAD block diagram with longitudinal belt dynamics 53
Fig. 39 FEAD block diagram with torsional belt dynamics 53
Fig. 40 Scheme of the vibrations damping cascade structure 54
Fig. 41 BSG speed control loop with discrete speed controller 54
Fig. 42 BSG speed control loop with continuous speed controller 55
Fig. 43 BSG speed control loop with continuous speed controler favorable for transfer function derivation 55
Fig. 44 Stribeck friction curve 58
Fig. 45 Simulink model of BSG speed/current cascade control structure, BSG mathematical model in dq coordinate system and accessory drive dynami 59
Fig. 46 BSG and ICE speed response with the control system tuned for vibrations damping. 61
Fig. 47 Torque/field current and rotor flux responses with the control system tuned for vibrations damping 61
Fig. 48 BSG electrical torque, belt torque and main bearing Stribeck friction torque responses with the control system tuned for vibrations damping 62
Fig. 49 BSG and ICE speed response with torque cut-off after reaching the referent speed... 63
Fig. 50 BSG speed control loop with continuous speed controller and rigid coupling between BSG and ICE crankshaft 63

Fig. 51 BSG and ICE speed response with the control system tuned as if the coupling between them was rigid 64
Fig. 52 Torque/field current response with the control system tuned as if the coupling between them was rigid 65
Fig. 53 BSG electrical torque, belt torque and main bearing Stribeck friction torque responses with the control system tuned as if the coupling between them was rigid 65
Fig. 54 Speed response comparison for the torsional vs. longitudinal model of the FEAD belt dynamics 66
Fig. 55 Current and rotor flux response comparison for the torsional vs. longitudinal model of the FEAD belt dynamics 66
Fig. 56 Torque response comparison for the torsional vs. longitudinal model of the FEAD belt dynamics 67
Fig. 57 Friction analysis in a 4-cyliner engine using EXCITE™ 68
Fig. 58 Global data 69
Fig. 59 Drive layout 69
Fig. 60 Pulley properties 70
Fig. 61 Tensioner geometry 70
Fig. 62 Belt geometry 70
Fig. 63 Belt mass properties 71
Fig. 64 Belt elasticity properties 71
Fig. 65 Stiffness, damping and tangential friction of belt and pulley front and back side contacts 72
Fig. 66 FEAD Multi Body Model – 2D View 73
Fig. 67 FEAD Multi Body Model – 3D View 73
Fig. 68 Friction characteristic of the crankshaft bearing 74
Fig. 69 Scheme of the model for EXCITE ™/MATLAB cosimulation 74
Fig. 70 EXCITE ™ interface block in Simulink 75
Fig. 71 Setup of Simulink model path in EXCITE ™ "Link to MATLAB" block 76
Fig. 72 Setup of elements to be connected to the interface with MATLAB and their respective connection types in EXCITE ™ "Link to MATLAB" block 76
Fig. 73 Cosimulation results 77
Fig. 74 Speed response comparison between EXCITE ™ and MATLAB 77
Fig. 75 Torque response comparison between EXCITE ™ and MATLAB 78

Fig. 76 Response comparison between EXCITE ™ and MATLAB of torque available for BSG acceleration 79
Fig. 77 Analysis of belt slippage by observing specialized finite "MASS" elements contacting the pulleys at given time periods 80
Fig. 78 Vehicle model in CRUISE ™ M featuring integrated models of different subsystems 81
Fig. 79 CRUISE ™ M P0 hybrid vehicle model 83
Fig. 80 Vehicle model with brakes and wheels 84
Fig. 81 Driveline model 85
Fig. 82 Cockpit and driver blocks 86
Fig. 83 Driving regime #1 87
Fig. 84 Driving regime #2 87
Fig. 85 Stop/start and boost control logic in CRUISE ™ M 89
Fig. 86 Driving regime #1 simulation results 90
Fig. 87 Detailed view of Driving regime #1 simulation results emphasizing stop/start function 91
Fig. 88 Detailed view of Driving regime #1 simulation results emphasizing boosting function 92
Fig. 89 BSG torque and speed response, along with its electromagnetic response during boosting periods 92
Fig. 90 Comparison of vehicle velocity and total torque at clutch for the cases with and without boosting 94
Fig. 91 Driving regime #2 simulation results 95
Fig. 92 Driveline model extended with an elastic shaft 96
Fig. 93 BSG and ICE speeds and torques during start-up period with the elasticity of the belt included in the driveline model 97
Fig. 94 Vehicle velocity, BSG and ICE torque responses on driving regime #1 desired velocity change, with the driveline of the system being elastic 98
Fig. 95 BSG and ICE speed responses on driving regime #1 desired velocity change, with the driveline of the system being elastic 98
Fig. 96 Detail views of BSG speed response, driver load signal, ICE torque and shaft torque 99
Fig. 97 BSG speed, BSG torque and ICE torque responses with compensation of shaft torque by the BSG 100
Fig. 98 Detail view of the driver load signal, ICE torque and shaft torque responses 100

Fig. 99 Speed response comparison of BSG and ICE during run-up in three different simulation environments 101

LIST OF TABLES

Table 1 Equivalence between DC and induction machine currents 23
Table 2 System parameters..... 60

LIST OF SYMBOLS AND UNITS

Symbol	Unit	Description
A_{ODO}	-	Damping optimum characteristic polynomial
a	-	Operator that transforms phase variables into space vectors
a_i	-	Transfer function denominator coefficients
b_i	-	Transfer function numerator coefficients
D_i	-	Damping optimum characteristic ratio
d_L	N s m^{-1}	Longitudinal damping coefficient of the belt
d_T	N m s rad^{-1}	Torsional damping coefficient of the belt
EA	N	Timing belt longitudinal stiffness
F_{belt}	N	Force transferred by the timing belt
$\bar{f}$	-	Arbitrary space vector
f_a	-	Arbitrary phase quantity of induction motor phase a
f_b	-	Arbitrary phase quantity of induction motor phase b
f_c	-	Arbitrary phase quantity of induction motor phase c
f_d	-	Timing belt damping factor
f_d	s	Field component of an arbitrary space vector
f_m	-	Amplitude of an arbitrary phase quantity
f_q	-	Torque component of an arbitrary space vector
f_α	-	Real component of an arbitrary space vector
f_β	-	Imaginary component of an arbitrary space vector

G	-	Transfer function
G_o	-	Open loop transfer function
G_c	-	Closed loop transfer function
I_m	A	Current amplitude
i_{ar}	A	Induction motor rotor phase a current
i_{as}	A	Induction motor stator phase a current
i_{bat}	A	Battery current
i_{belt}	-	Transmission ratio between the BSG and the ICE
i_{br}	A	Induction motor rotor phase b current
i_{bs}	A	Induction motor stator phase b current
i_{cr}	A	Induction motor rotor phase c current
i_{cs}	A	Induction motor stator phase c current
i_e	A	DC machine excitation current
$\mathrm{i_{mr}}$	A	Magnetizing current that generates the rotor magnetic field
i_{sd}	A	Stator field current
i_{sdR}	A	Stator field current reference
i_{sq}	A	Stator torque current
i_{sqR}	A	Stator torque current reference
J_{BSG}	kg m^2	Inertia of the BSG rotor
J_{ICE}	kg m^2	Inertia of the ICE crankshaft
J_{total}	kg m^2	Total inertia of the drive
K_{ci}	**Ω**	PI current controller gain
$K_{c\omega}$	$kgm^2\ s^{-1}\ H^{-1}\ A^{-1}$	PI speed controller gain
K_q	Ω^{-1}	Virtual q coil gain

k_L	N m^{-1}	Longitudinal stiffness coefficient of the belt
k_m	N m A^{-1}	Torque constant of an electrical machine
k_T	N m rad^{-1}	Torsional stiffness coefficient of the belt
k_t	N m A^{-1}	Torque constant of an induction motor
L	m	Length of the timing belt
L_{ar}	H	Induction motor rotor phase a inductance
L_{as}	H	Induction motor stator phase b inductance
L_{br}	H	Induction motor rotor phase b inductance
L_{bs}	H	Induction motor stator phase b inductance
L_{cr}	H	Induction motor rotor phase c inductance
L_{cs}	H	Induction motor stator phase c inductance
L_d	H	Induction of the virtual d coil
L_m	H	Magnetizing inductance
L_{mr}	H	Magnetizing rotor inductance
L_{ms}	H	Magnetizing stator inductance
L_{pr}	H	Induction motor rotor phase inductance
L_{ps}	H	Induction motor stator phase inductance
L_q	H	Induction of the virtual q coil
$L_{\sigma r}$	H	Rotor leakage inductance
$L_{\sigma s}$	H	Stator leakage inductance
M_C	N m	Coulumb static friction torque
M_{br}	N m	Induction machine breakaway torque
M_r	H	Mutual inductance between two rotor phases
M_s	N m	Induction machine starting torque

M_s	H	Mutual inductance between two stator phases
M_s	N m	Maximum value of static friction torque
M_{sr}	N m	Maximum mutual inductance between stator and rotor phases
m_{BSG}	N m	Torque generated by or transferred to the BSG
m_e	N m	Electrical torque of the induction machine
m_{ICE}	N m	Torque generated by or transferred to the ICE
m_L	N m	Load torque
m_{MB}	N m	ICE crankshaft main bearing torque
n	rpm	Rotational speed
n_s	rpm	Synchronous speed
P_{el}	W	Electrical power of the induction machine
P_{me}	W	Mechanical power of the induction machine
p	-	Number of machine pole pairs
R_{ar}	Ω	Induction motor rotor phase a resistance
R_{as}	Ω	Induction motor stator phase a resistance
R_{br}	Ω	Induction motor rotor phase b resistance
R_{bs}	Ω	Induction motor stator phase b resistance
R_{cr}	Ω	Induction motor rotor phase c resistance
R_{cs}	Ω	Induction motor stator phase c resistance
R_d	Ω	Resistance of the virtual d coil
R_r	Ω	Induction motor rotor winding resistance
R_s	Ω	Induction motor stator winding resistance
R_q	Ω	Resistance of the virtual q coil
r_{BSG}	m	Radius of the BSG pulley

r_{EM}	-	Frequency ratio of two-mass FEAD simplification
r_M	-	Ineritia ratio of two-mass FEAD simplification
r_{ICE}	m	Radius of the ICE pulley
s	-	Slippage coefficient
s	-	Laplace operator
s_{br}	-	Breakaway slippage
T	-	Sample time
T_{ci}	s	PI current controller time constant
$T_{c\omega}$	s	PI speed controller time constant
T_{ei}	s	Current control loop equivalent time constant
$T_{e\omega}$	s	Speed control loop equivalent time constant
T_{inv}	s	Inverter time constant
T_{n-i}	s	Cascade structure time constants
T_q	s	Rotor time constant
T_q	s	Virtual q coil time constant
$T_{\Sigma i}$	s	Parasitic time constant of the current control loop
$T_{\Sigma\omega}$	s	Parasitic time constant of the speed control loop
t	s	Time
$U0$	V	Battery maximum voltage
u_{ar}	V	Induction motor rotor phase a voltage
u_{as}	V	Induction motor stator phase a voltage
u_{br}	V	Induction motor rotor phase b voltage
u_{bat}	V	Battery voltage at terminals
u_{bs}	V	Induction motor stator phase b voltage

u_{cr}	V	Induction motor rotor phase c voltage
u_{cs}	V	Induction motor stator phase c voltage
u_{csd}	V	Available voltage for field current generation at virtual stator d coil
u_{csq}	V	Available voltage for torque current generation at virtual stator q coil
u_R	V	Discrete voltage reference
u_R^*	V	Extrapolated voltage reference
u_{sq}	V	Stator torque voltage
u_{sd}	V	Stator field voltage
v_{BSG}	m s^{-1}	Tangential velocity of BSG rotor
v_{ICE}	m s^{-1}	Tangential velocity of ICE crankshaft
x_{BSG}	m	Tangential displacement of BSG rotor
x_{ICE}	m	Tangential displacement of ICE crankshaft
x_i	-	System input
x_o	-	System output
y	-	System output
y_R	-	Referent variable
$\Delta\alpha$	rad	Torsional angle
$\Delta\omega$	rad s^{-1}	Torsional angular velocity
Δu_{sq}	V	Torque axis coupling term
Δu_{sd}	V	Field axis coupling term
Ω_0	rad s^{-1}	Natural frequency of the vibrations of the two-mass simplification of FEAD
Ω_{01}	rad s^{-1}	natural frequency of BSG side vibrations
Ω_{02}	rad s^{-1}	natural frequency of ICE side vibrations

α_{BSG}	rad	BSG rotational angle
α_{ICE}	rad	ICE rotational angle
δ	-	Stribeck coefficient
ϵ	rad	Angle between the stator and rotor coordinate systems
ζ	-	Coefficient of relative damping
σ	-	Leakage coefficient
σ_i	-	Real part of a complex system pole
Φ_a	Wb	Magnetic flux generated by the armature current of the DC machine
Φ_e	Wb	Magnetic flux generated by the excitation current of the DC machine
Ψ_r	Wb	Magnetic flux of the induction machine rotor
ψ_{ar}	Wb	Magnetic flux of induction motor rotor phase a
ψ_{as}	Wb	Magnetic flux of induction motor stator phase a
ψ_{br}	Wb	Magnetic flux of induction motor rotor phase b
ψ_{bs}	Wb	Magnetic flux of induction motor stator phase b
ψ_{cr}	Wb	Magnetic flux of induction motor rotor phase c
ψ_{cs}	Wb	Magnetic flux of induction motor stator phase c
θ_f	rad	Phase angle of an arbitrary phase quantity or a space vector
ρ	rad	Angle between the stator coordinate system and the d-q system
ω_{BSG}	rad s^{-1}	BSG angular velocity
ω_{ICE}	rad s^{-1}	ICE angular velocity
ω_i	-	Imaginary part of a complex system pole
ω_f	rad s^{-1}	Angular frequency an arbitrary phase quantity or a space vector

ω_{mr}	rad s^{-1}	Angular velocity of the rotor flux vector
ω_S	rad s^{-1}	Stribeck angular velocity

LIST OF ABBREVIATIONS

Abbreviation	Meaning
AC	Alternating Current
BSG	Belt Starter-Generator
DC	Direct Current
DoF	Degree of Freedom
EMF	Electromagnetic Force
FEAD	Front End Accessory Drive
FHEV	Full Hybrid Electric Vehicle
FOC	Field Oriented Control
FMU	Functional-Mockup Unit
HEV	Hybrid Electric Vehicle
HECPG	Hybrid Excited Claw Pole Generator
HECPSG	Hybrid Excited Claw Pole Starter Generator
HiL	Hardware-in-the-Loop
ICE	Internal Combustion Engine
MHEV	Mild Hybrid Electric Vehicle
NEDC	New European Driving Cycle
PHEV	Plug-in Hybrid Electric Vehicle
PI	Proportional-Integral
PWM	Pulse-Width-Modulation
SUI	(hrv. S Unutrašnjim Izgaranjem)
SoC	State of Charge
SoH	State of Health

Sažetak

Uslijed klimatskih promjena uzrokovanih stakleničkim plinovima, unutar kojih najveći udio ima CO_2, regulatorna tijela proizvođačima automobila postavljaju postepeno strože zahtjeve za smanjenjem emisija. Od 2021. ciljana prosječna emisija flote pojedinog proizvođača postaje <= 95 g CO_2/km što odgovara smanjenju od 27% u odnosu na prijašnjih 130 g CO_2/km. Ovi zahtjevi motivirali su proizvođače na razvoj novih tehnologija kako bi elektrificirali svoje flote, a povoljna tehnologija s gledišta cijene i jednostavnosti integracije jest 48 V električna arhitektura s asinkronim motorom kao aktuatorom. Asinkroni motor koji ima funkciju startera i generatora je remenom povezan na radilicu motora SUI (s unutarnjim izgaranjem), a u literaturi se može naći pod akronimom BSG (eng. Belt Starter Generator). Cilj ovog rada jest projektirati sustav za prigušenje vibracija elastičnog remena koji povezuje remenice BSG-a i radilice motora SUI, te ga ispitati na mikro razini (sustav FEAD, eng. Front End Accessory Drive) i na sistemskoj razini (vozilo). U tu svrhu izrađen je matematički model asinkronog motora u programskom paketu MATLAB/SIMULINK, unutar kojeg je implementiran regulacijski sustav podešen prema optimumu dvostrukog odnosa, a FEAD je izveden kao dvomaseni sustav karakteriziran oprugom i prigušnicom. Kako bi se dobio vjerniji odziv, u simulacijskom okruženju AVL EXCITE ™ Timing Drive izrađen je FEAD model, gdje je elastični remen diskretiziran većim brojem specijalnih elemenata u odnosu na dvomasenu simplifikaciju iz MATLAB-a. Performanse upravljačkog sustava na ovakvom modelu ispitane su preko kosimulacije između EXCITE ™ Timing Drive-a i MATLAB-a. Nadalje, u svrhu provedbe sistemske simulacije u simulacijskom okruženju AVL CRUISE ™ M u postojeći model hibridnog vozila P0 konfiguracije implementiran je model BSG-a i upravljački sustav iz MATLAB-a kao FMU (eng. Functional Mock-up Unit). Upravljački sustav podešen je tako da omogućuje pokretanje i potpomognuti rad motora SUI po potrebi, a prijenos okretnog momenta s vratila BSG-a na radilicu motora SUI ostvaren je krutom vezom. Konačno, kako bi se u sistemskoj simulaciji uključila dinamika elastičnog prijenosa, proračunata je ekvivalentna torzijska krutost i prigušenje FEAD sustava iz EXCITE ™ Timing Drive-a, te je njima parametrirana sprega između rotora BSG-a i radilice motora SUI unutar CRUISE ™ M modela.

Summary

Due to climate change caused by greenhouse gases, with CO_2 making up the biggest share, regulatory bodies are imposing gradually stricter demands for reduction of emissions on car manufacturers. Starting from 2021., the average emissions target for a manufacturer's fleet is set to 95 g CO_2/km, which corresponds to the reduction of 27% compared to the former target of 130 g CO_2/km. These demands have motivated car manufactures to develop novel technologies in order to electrify their fleets and a favorable technology from the standpoint of cost and simplicity of integration is the 48 V electrical architecture utilizing an induction motor actuator. The induction motor, which operates both as a starter and a generator, is coupled via the timing belt with the crankshaft of an internal combustion engine (ICE) and is referenced in the literature as BSG (Belt Starter Generator). The goal of this thesis was to design a vibration damping system for the belt which couples the BSG pulley with the ICE crankshaft pulley and to test the aforementioned system on the micro level (FEAD system, i.e. Front End Accessory Drive), as well as on the system level (vehicle). To this end, a mathematical model of an induction motor was made in MATLAB/SIMULINK simulation environment, within which the control system based on the damping optimum criterion has been implemented and FEAD defined as two masses coupled via spring and a damper. In order to obtain a more accurate system response, a FEAD model utilizing the elastic belt comprised of a larger number of specialized discrete elements compared to the two mass MATLAB simplification has been designed in the AVL EXCITE ™ Timing Drive. The performance of the control system on this model was tested by means of EXCITE ™ and MATLAB cosimulation. Furthermore, the induction motor model and the corresponding control systems from MATLAB have been compiled as an FMU (Functional Mock-up Unit) and integrated into the existing P0 hybrid vehicle model in AVL CRUISE ™ M in order to perform a system level simulation. The control system has been set up to enable "on demand" start-up and boosting of the ICE, with the BSG torque being transferred to the ICE crankshaft by means of rigid coupling. Finally, in order to capture the dynamics of the elastic belt in CRUISE ™ M system simulation, the equivalent torsional stiffness and damping of the FEAD system from EXCITE ™ Timing Drive have been calculated and used to parametrize the coupling between the BSG rotor and ICE crankshaft in CRUISE ™ M model.

Prošireni sažetak

Proizvođači automobila okreću se razvoju novih tehnologija kako bi elektrificirali svoje flote uslijed postepeno strožih zahtjeva za smanjenjem emisije stakleničkih plinova. Povoljno rješenje s gledišta cijene i jednostavnosti implementacije jest hibridno vozilo sa električnom arhitekturom maksimalnog napona od 48 V. Ovakvo vozilo naziva se MHEV (eng. Mild-hybrid Electric Vehicle) i karakterizirano je P0 konfiguracijom pogonskog sustava, kod kojeg je motor SUI putem elastičnog remena povezan sa asinkronim BSG-om. Cilj ovog diplomskog rada bio je dizajnirati sustav regulacije brzine vrtnje za BSG s naglaskom na prigušenje vibracija remena, koje se manifestiraju kao torzijske (kutne) vibracije BSG-a i koljenastog vratila motora SUI. Vladanje regulacijskog sustava ispitano je na mikro razini (razini sustava FEAD) i makro razini (sistemskoj razini) koristeći simulacijska okruženja EXCITE ™ Timing Drive i CRUISE ™ M tvrtke AVL – AST d.o.o. Diplomski rad podijeljen je u 8 poglavlja, sažetak kojih je:

1. **UVOD –** Prikazuje se koliki udio u globalnom zagađenju stakleničkim plinovima ima transportni sektor, konkretno cestovni promet, navode se aktualni podaci o ograničenju emisija flote vozila pojedinog proizvođača. Opisuju se funkcionalnosti MHEV-a poput stop/start mogućnosti, potpomaganja motora SUI okretnim momentom elektromotora i rekuperacije energije.

2. **48 V P0 "MILD HYBRID" –** Iznose se argumenti interesantni proizvođačima automobila za odabir razvoja 48 V MHEV-a kao strategije za postizanje propisane prosječne emisije CO_2 njihovih flota. Opisuje se P0 konfiguracija pogonskog sustava hibridnog vozila koju čini 48 V električna arhitektura i FEAD sustav.

3. **ASINKRONI (INDUKCIJSKI) MOTOR –** Objašnjava se načelo rada asinkronog stroja i njegova specifična karakteristika momenta. Uspoređuju se asinkroni motor s takozvanim „kandžastim" polovima i kavezni asinkroni motor sa stajališta primjene u FEAD sustavu i mogućnosti izvoda matematičkog modela pogodnog za vektorsko upravljanje.

4. **MATEMATIČKI MODEL ASINKRONOG STROJA –** Objašnjava se koncept vektorskog upravljanja dovodeći ga u analogiju sa istosmjernim strojem kod kojeg se magnetskim poljem i momentom stroja upravlja odvojeno. Izvodi se matematički model asinkronog stroja u stacionarnom trofaznom sustavu, te se putem Clarke i Park transformacija prevodi u rotirajući ortogonalni $d-q$ sustav. Izlaže se pojednostavljeni model dinamike invertera. Izvodi se linearni model asinkronog stroja u $d-q$ sustavu pogodan za primjenu linearnih metoda regulacije poput podešavanja polova sustava prema optimumu dvostrukog odnosa.

5. **DIZAJN UPRAVLJAČKOG SUSTAVA S NAGLASKOM NA PRIGUŠENJE VIBRACIJA –** Daje se shema kaskadnog regulacijskog sustava brzine vrtnje i struje BSG-a. Objašnjava se metoda podešavanja polova prema optimumu dvostrukog odnosa. Izvodi se pojednostavljenje dinamike elastičnog FEAD sustava kao dvomasenog sustava s elastičnom vezom, te se izražavaju ekvivalentna torzijska krutost i prigušenje remena. Provodi se sinteza parametara PI regulatora struje i PI regulatora brzine vrtnje BSG-a podešavanjem polova sustava zatvorenog regulacijskog kruga prema optimumu dvostrukog odnosa. Uspoređuju se rezultati simulacije napravljene u MATLAB-u, za slučaj podešenja regulacijskog sustava koji uzima u obzir efekte elastičnosti pri sintezi parametara i slučaja kada je sinteza izvršena kao da je sustav spregnut krutom vezom. Uspoređuju se odzivi sustava koji sadrži longitudinalni dvomaseni FEAD model s onim koji sadrži ekvivalenti torzijski dvomaseni model.

6. **MODEL FEAD-A U EXCITE ™ TIMING DRIVE-U –** Izrađuje se precizniji model FEAD sustava koristeći specijalizirane konačne elemente unutar alata EXCITE ™ Timing Drive, koji za razliku od dvomasene simplifikacije korištene u MATLAB-u uzima u obzir fizičke fenomene poput klizanja remena po remenicama (eng. slip). Podešava se kosimulacija s MATLAB-om, te se komentiraju rezultati.

7. **SISTEMSKA SIMULACIJA U CRUISE ™ M SIMULACIJSKOM OKRUŽENJU -** Objašnjava se načelo sistemske simulacije, te se opisuju pojedine komponente u modelu. Komentiraju se režimi vožnje odabrani za ispitivanje stop/start funkcionalnosti i asistiranja momentom BSG-a pri ubrzavanju vozila. Izlaže se shema kontrolne logike za start/stop i potpomaganje okretnim momentom (eng. boosting). Daje se osvrt na rezultate simulacije. U sistemsku simulaciju se uključuje blok koji uvodi efekt elastičnosti u spregu između BSG-a i motora SUI, definiranu ekvivalentnom torzijskom krutosti i prigušenjem remena iz EXCITE

™ Timing Drive-a, odnosno MATLAB-a. Odzivi brzina vrtnje BSG-a i motora SUI se uspoređuju s onima iz MATLAB-a i EXCITE ™ Timing Drive-a

8. **ZAKLJUČAK –** Daje se cjelokupni osvrt na sve izloženo u prethodnim poglavljima, te se iznosi zaključak. Predlažu potencijalni smjerovi u kojima bi se rad mogao proširiti.

1. INTRODUCTION

1.1. Transport emissions in Europe

Almost a quarter of Europe's greenhouse gas emissions contributions are associated with transport, which is also the main cause of air pollution in cities. Emissions in this sector have only started to decrease in 2007, however they still remain higher than those from 1990. Air pollutants from transportation harm our health and need to be drastically reduced in order to ensure the wellbeing of European citizens. By 2050, the GHG (greenhouse gas) emissions from transportation will need to be at least 60% lower than those observed in 1990 and firmly on the path towards zero. Within this sector, road transportation is the highest emitter of GHG, totaling at over 70% of all emissions [1].

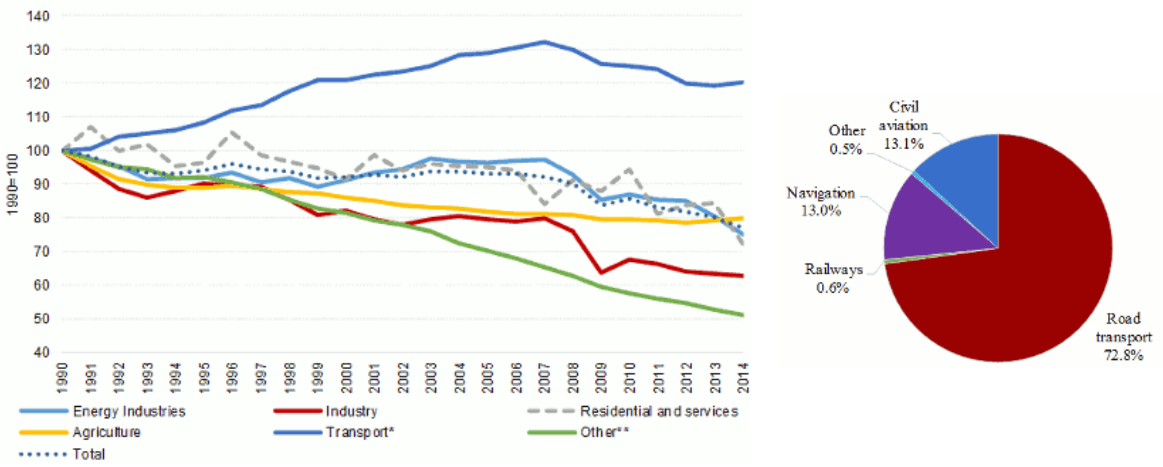


Fig. 1 GHG Emissions per sector (left) and emission percentage of components making up the transport sector [1].

With the global shift to low carbon economy, Europe's answer to emission reduction challenge in the transport sector is in the form of an irreversible shift to low-emission mobility. This strategy will benefit European citizens by improving the air quality, reducing noise levels, lowering congestion levels and improving safety [1]. In order to come through with this strategy, the European Commission has outlined three priority areas of action:

1) Increasing the efficiency of the transport system
2) Speeding up the deployment of low-emission alternative energy for transport

3) Moving towards zero-emission vehicles

Since this thesis considers the design and simulation of the control system for an electrical system intended to reduce GHG emissions and fuel consumption level in passenger cars, the next chapter will put into perspective emissions originating from the passenger car category.

1.2. Passenger car emissions

Passenger cars are responsible for around 12%, of total EU emissions of carbon dioxide, the main greenhouse gas. Between the years 2015 and 2019 the target manufacturers fleet-wide average emission was 130 g CO_2/km, which corresponds to 5.6 l/km of petrol and 4.9 l/km diesel respectively. This target was reached in 2013, two years ahead of schedule. According to data, the average level of emissions of new cars registered in 2018 in EU and Iceland were 120.4 g CO_2/km, which yields 14.2% decrease in emissions since 2010. Starting from 2021, the EU fleet-wide emission target for new cars will be 95 g CO_2/km (based on NEDC certification driving cycle). These emission targets are set for manufacturers according to the average mass of their vehicles, which means that manufacturers of heavier cars are allowed higher emissions than manufacturers of lighter cars [2]. The insight into CO_2 reduction in passenger cars since 2001 to 2017 by EU member state is given on figure 2.

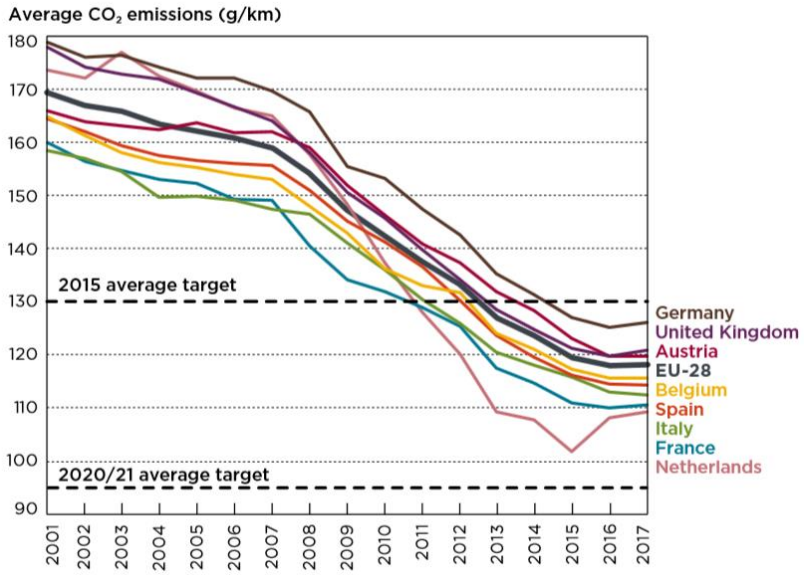


Fig. 2 Reduction of CO_2 in passenger cars by EU member state 2001 – 2017 [3].

In order to comply with aforementioned demands on emissions reduction, car manufacturers have developed a number of novel technologies to facilitate the electrification of their respective fleets.

An overview of such technologies represented by different hybridization levels characterized by different electrification architectures is given in the following chapter.

1.3. Road to electrification

Since vehicle electrification on global scale is not only an endeavor in technology development, but also has an impact on economy and infrastructure of the world, intermediate steps have been put in place in order to ease the transition of the world from ICE powered vehicles to fully electric ones. This intermediation consists of developing and introducing to the market several architectures of hybrid vehicles, that is, vehicles characterized by at least two sources of power for propulsion: the internal combustion engine and an electric motor. The powertrain of a HEV (Hybrid Electric Vehicle) is quite complex because it contains all the components of an ICE vehicle and a number of additional components depending on the level of hybridization. Figure 3 gives a concise overview of existing hybridization levels with corresponding electrification architectures, with respect to environmental impact they have.

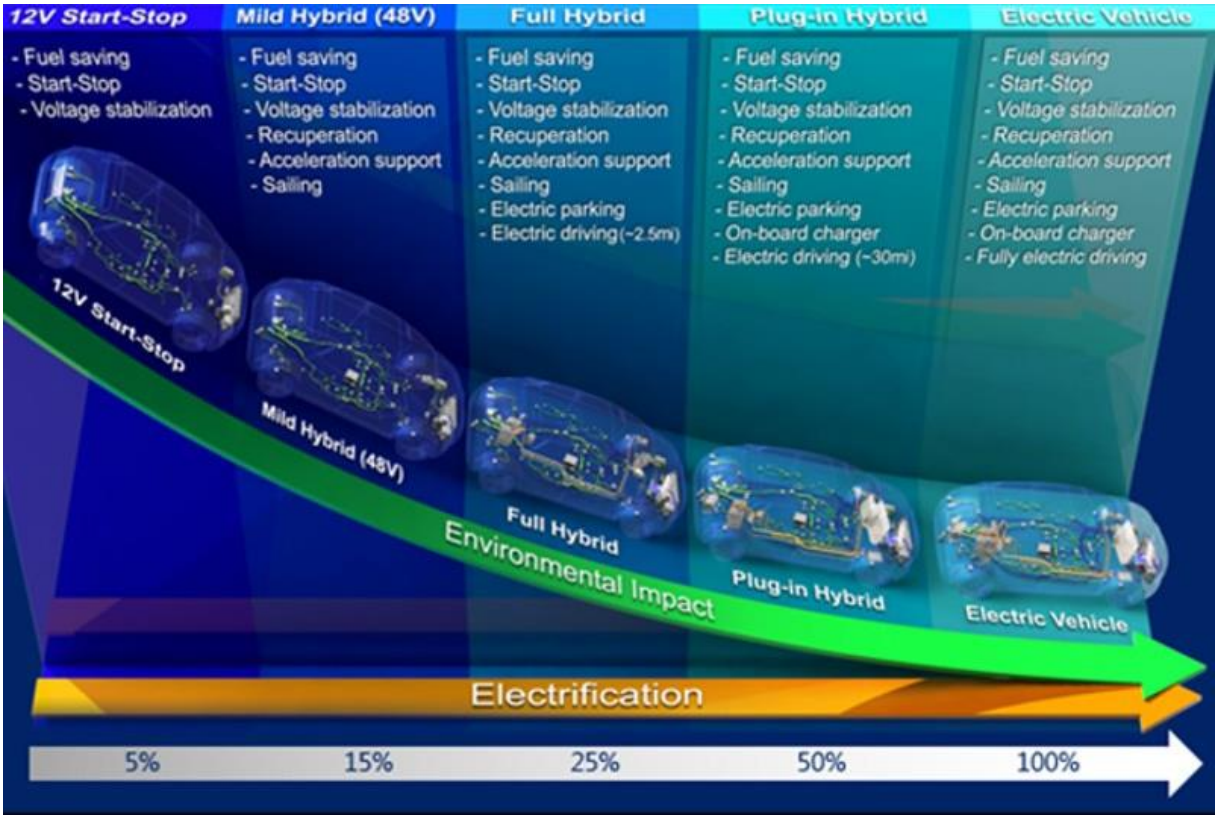


Fig. 3 Hybridization levels with corresponding electrification architectures [4].

Hybridization of a conventional powertrain gives the following advantages [5](minding that the utilization of these advantages varies with the level of hybridization):

- Because of the torque assistance provided, the ICE can work in the vicinity of the most fuel-efficient operating point (in the optimal point of the speed torque curve).
- The ICE can be downsized, while at the same time retaining constant overall torque and power output of the vehicle powertrain, owing to the electric motor assistance.
- The kinetic energy of the vehicle during braking can be recovered and stored in the high voltage battery, with the help of the electric machine operating as a generator.
- The torque response of the powertrain can be improved because of the instant torque delivery of the electric motor.
- The gear ratios of the transmission can be lowered, to keep the engine at lower speed operating points (better fuel efficiency), because the electric motor can deliver instant torque following the drivers request.

These advantages are obtained through a number of functions a hybrid vehicle can perform. Insight into some of these functions is given in the next chapter.

1.4. Hybrid vehicle functions

1.4.1. Engine idle stop/start

When the vehicle is stationary the stop/start function switches of the ICE without the command of the driver through the ignition key or ignition button. The effects of this function are reduced fuel consumption and emissions of the vehicle [5]. When the signal coming from the driver implies intention to drive (clutch pedal pressed or brake pedal released) the engine is restarted automatically. Hybrids with stop/start system are additionally equipped with an energy management system which optimizes the consumption of low voltage (12V) battery energy [5]. Energy management system ensures that the battery supplies electrical consumers with energy even if the engine is running. The benefit of this functionality is reduced fuel consumption because the load torque of the alternator in this case is nearly zero. Vehicles that have stop/start and energy management functions are called micro hybrids.

Figure 4 shows the micro - hybridized 1.6 dCi Renault engine.

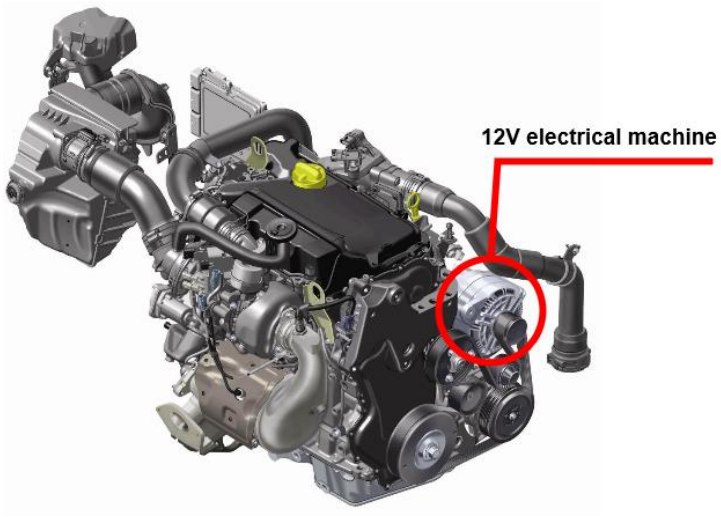


Fig. 4 Renault 1.6 dCi engine equipped with a 12V electrical machine [5].

1.4.2. Electric torque assistance

The function of a hybrid vehicle with the greatest impact on drivability is the torque assistance to the ICE engine provided by the electrical machine. There are two types of torque assistance: torque filling and torque boosting.

Torque filling is aimed at reducing the delay present when the driver presses the accelerator pedal requesting more torque from the powertrain in order to accelerate the vehicle. An ICE engine has a pronounced delay in delivering torque which may be caused by the inertia of mechanical moving parts, inertia of the air in the intake manifold and the torque limitation (to prevent smoke in the exhaust) [5]. In order to compensate for the torque response delay in such situations, the electrical machine provides additional torque and shifts the engine operating point into the area of higher torque, enabling the vehicle to be accelerated at the drivers request.

Torque boosting is an operation mode of an electrical machine used when the ICE engine has reached its maximum torque output defined by the engine speed. By adding the torque of the electrical motor, upon to the engine torque, the maximum overall torque of the powertrain is increased [5]. Availability of torque boosting is dependent on the state-of-charge (SoC) of the battery and is only available in short periods in order to prevent battery depletion.

Electric torque assistance can be provided by mild hybrid electric vehicles (MHEV), full hybrid electric vehicles (FHEV) and plug-in hybrid electric vehicles (PHEV). Figure 5 visualizes the shifting of ICE engine operating point during torque filling and offsetting during torque boosting.

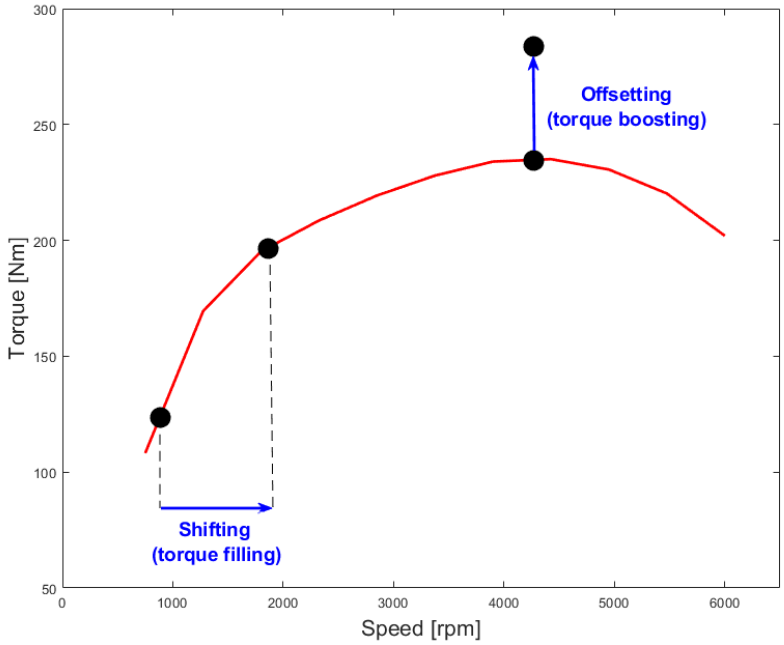


Fig. 5 Shifting and offsetting of the operating point of an ICE

1.4.3. Energy recuperation

Energy recuperation in a hybrid vehicle is directly tied to the braking process. In order to decelerate the vehicle, braking torque is required. Braking torque can be achieved in several ways:

1) Through the hydraulic brakes
2) Through the powertrain
3) Through the hydraulic brakes plus the powertrain

Powertrain braking in a vehicle with a conventional powertrain, i.e. one that is only run by an ICE engine, occurs when the driver releases the accelerator pedal and thus interrupts the fuel injection. The engine overruns (engine braking) and the amount of engine brake is equal to the total power losses of the engine (friction torque + pumping losses + auxiliary devices). Therefore, no energy is recuperated.

However, in a hybrid vehicle, energy can always be recuperated during braking irrespective of the level of hybridization. The reason for this is the inherent nature of the electrical machine: it can operate both as a motor and a generator. During braking, the electrical machine is in generator mode. The kinetic energy of the vehicle spins the rotor of the generator, overcoming its negative torque and generates electrical energy which is then stored in the

battery. The amount of electrical energy generated (harvested) during braking depends on the power of the electrical machine [5]. Figure 6 shows the power flow in a hybrid vehicle when in energy recuperation mode.

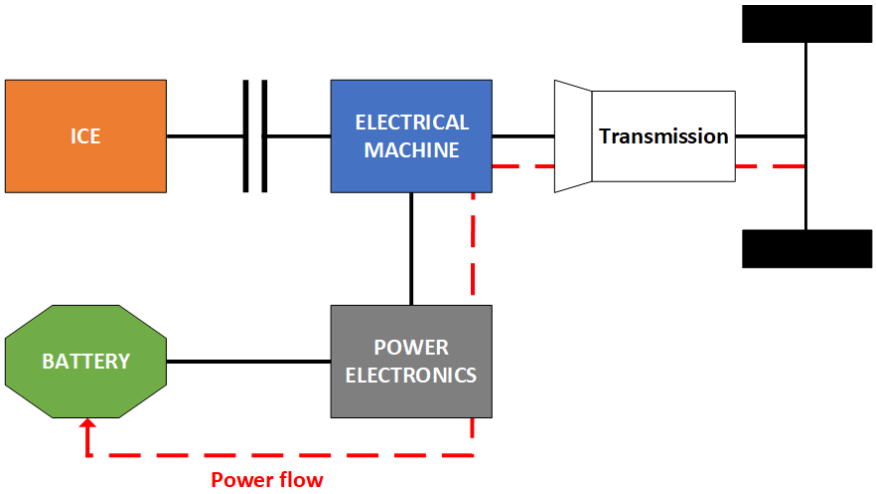


Fig. 6 Hybrid vehicle power flow in recuperation mode

There are more functions a hybrid vehicle can perform, for instance, fully electrical driving and charging the battery from the grid, but these operating modes won't be referred to here because they are characteristic to FHEV or PHEV. Mild hybrid electric vehicle (MHEV), which is considered in the scope of this thesis, performs stop/starting, electrical torque assistance and energy recuperation described in this chapter by utilizing on a 48V electrical architecture, which is described in the following chapter.

2. 48V P0 MILD HYBRID

2.1. Reasons to opt for a 48V system

With the new 95 g CO_2/km fleet emissions target coming into force in 2021, many manufacturers are turning to the 48V mild hybrid technology to help them meet the new regulations [4]. There are several advantages 48 V MHEV has over other electrification architectures:

- The system is relatively simple and cost-effective to engineer or even retrofit to existing platforms, especially if BSG is fitted into P0 configuration
- Good costs versus benefit ratio, with between 12% to 20% emissions saving
- The technology can be integrated using all MHEV configurations from P0 to P4

Furthermore, using a 48 V system maximizes the system voltage without the significant cost burden associated with increased safety regulations (ECE – R 100) associated with using a voltage system in excess of 60V DC [6]. A 48V system also enables e-machines with power range of up to 20 kW [6] or even up to 30 kW to be used [7], which offer significant energy recuperation potential, having in mind that the maximum amount of energy that can be recuperated is directly proportional to the power of the electrical machine.

2.2. 48V electrical architecture

Another benefit of a 48 V hybrid system is that it consists of only a few core components. These are: an electric motor of induction (asynchronous) type, an inverter, an energy storage system with high dynamic capability and a DC/DC converter [8]. As mentioned before, the main function of an asynchronous motor is to harvest energy during deceleration phases (recuperation) and to support the ICE with additional torque, as well as to run the ICE crankshaft up to speed at which combustion starts during stop/start mode of operation. Since an induction motor used for BSG purpose needs 3-phase alternating current in order to operate, an inverter is integrated into the electric motor. The inverter converts the 48V DC current supplied by the battery into 3-phase AC current for the motor by means of pulse-width-modulation (PWM). In

order to supply the electrical consumers with energy from the 48 V system, the 12 V single direction (buck) DC-DC converter is used to safely transfer energy from the 48 V to the 12 V level. When the 48 V system is implemented in P0 configuration of MHEV, additional components are needed to make the system operational, namely, the timing belt and the tensioner. The belt has to be designed to meet very high torque requirements and must be kept evenly tensioned by the tensioner, irrespectively of the operation mode or running direction. Figure 7 shows the electrical scheme of the 48V system with an induction motor connected via belt to the crankshaft pulley (P0 configuration).

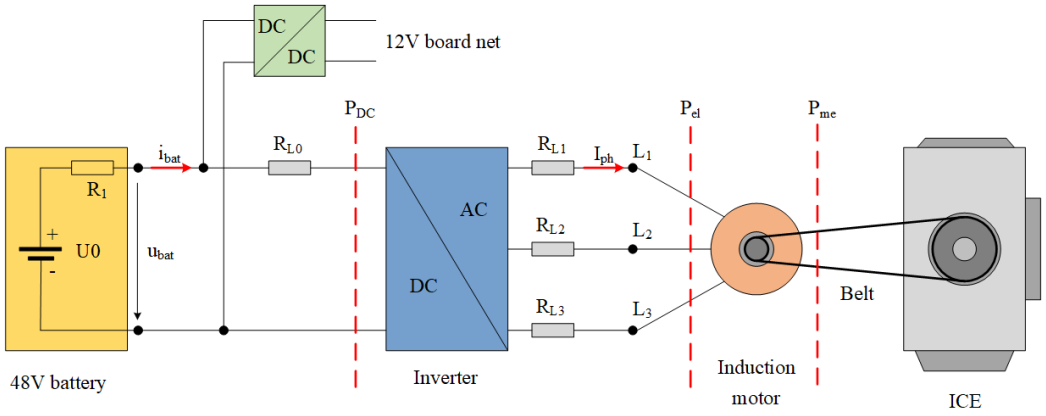


Fig. 7 48V electrical architecture in P0 configuration [7].

The SIMULINK model of the 48 V system in this work will be simplified, insofar that it captures the dynamics necessary to design the controller for the mitigation of timing belt vibrations. That is, the battery SoC dynamics will not be modelled, as well as its aging effects (i.e. battery state-of-health, SoH). However, the 48 V maximum voltage limit will be imposed on the system by limiting the current controller output to that value, which is the voltage command input for the inverter. The inverter dynamics will also be simplified in the simulation, taking form of a first-order lag model or PT_1 term defined by the inverter time constant. The stress will be on obtaining the induction motor mathematical model, design of the control system for mitigation of belt vibrations, and on the modelling of the FEAD system, which will firstly be modeled as a two – mass approximation and later on replaced by the EXCITE ™ Timing Drive model. Lastly, before proceeding to the modelling of the induction machine, the next chapter gives a brief description of the FEAD system.

2.3. FEAD

Front end accessory drive is a system of timing belt connected pulleys that transfers power from the crankshaft of the ICE or rotor of the BSG to auxiliary consumers (air conditioning, water pump). As mentioned in the last chapter, the belt has to meet very high torque demands and has to be kept tensioned at all times by the tensioner. Depending on whether the starter generator is operated for generating power or as a motor, feeding torque into the belt drive, the tight and slack spans alternate and the tensioner function is needed in different sections of the belt [9]. The simplest way to satisfy this requirement is to implement two separate tensioning elements, one positioned before and the other after the pulley of the BSG. An alternative can be the combination of both tensioning pulleys into a twin tensioner, in which a spring connects both arms of the tensioner. The optimal design is in the form of a decoupling tensioner, which changes its working position following the change of torque direction, which means the tensioner arms are in different positions whether the BSG is motoring or generating. This enables the pre-tensioning force to be optimal for the respective operating point [9]. The change of decoupling tensioner position according to BSG operation mode, as well as tensioner types discussed, are shown on figure 8.

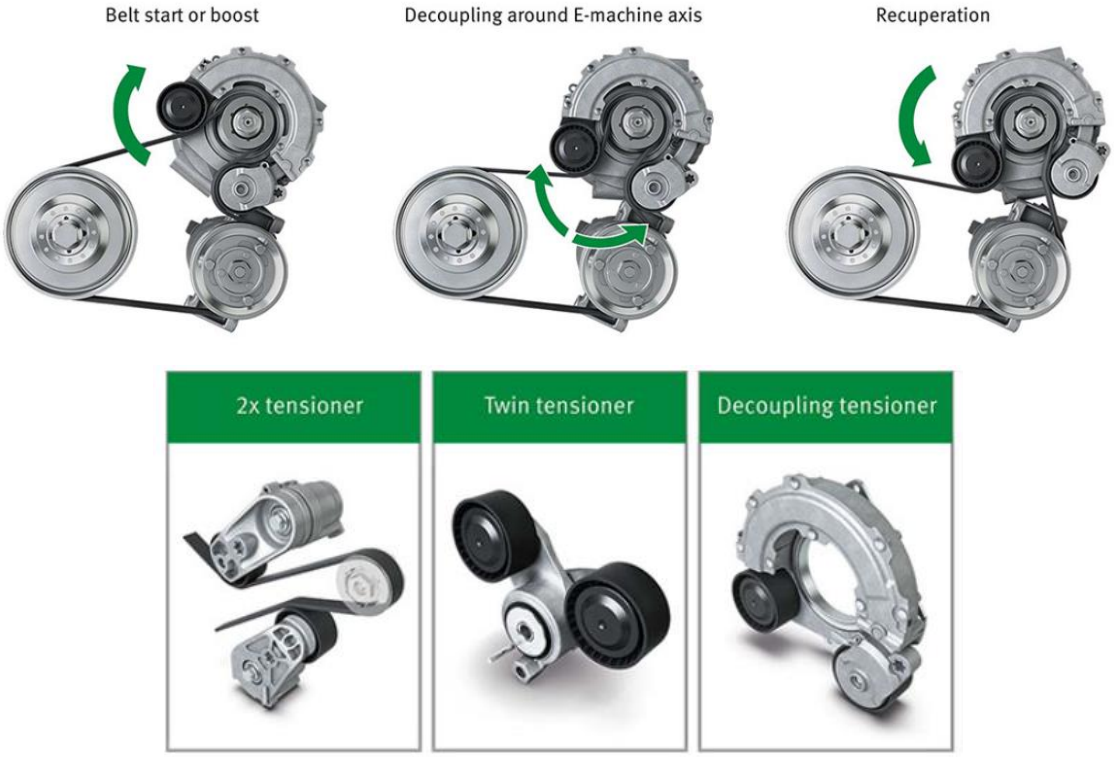


Fig. 8 Decoupling tensioner positions according to BSG operation mode and tensioner types [9].

Within the scope of this thesis the tensioner will be modelled in EXCITE ™ Timing Drive as a passive element, which means the amount of tension in the belt will be set through initial conditions, and no tensioning action will be performed during the cosimulation. The reason for this is to obtain a fairly simple and stable cosimulation model in order to minimize the possibility of errors arising from two different solvers working together. This model can later on be extended to include an active tensioner.

As to the dynamics of the FEAD system, it was simplified in order to analytically tune the BSG speed controller according to the damping optimum criterion, which is focused on mitigating the vibrations of the belt. This simplification observes the accessory drive only as two masses, i.e. the BSG rotor and ICE crankshaft, coupled via spring-damper element. Speed controller tuned in such manner is firstly going to be tested in MATLAB/SIMULINK on a two – mass accessory drive simplification, for which it was tuned, and then by means of cosimulation using the EXCITE ™ Timing Drive model, which contains a more accurate description of the belt drive utilizing on specialized finite elements.

As mentioned before, the BSG is almost always of the induction type. The next chapter gives a detailed description of an induction motor and its mathematical model.

3. ASYNCHRONOUS (INDUCTION) MOTOR

3.1. Principle of operation

Asynchronous motors operate on AC current with the speed of their rotor being load dependent and different from the synchronous speed, where synchronous speed is the electrical angular velocity corresponding to the fundamental frequency of the stator variables [10]. Asynchronous machines are mostly designed as three-phase low or mid power machines and predominantly used as motors, as opposed to synchronous machines, which are mostly high power and used as generators [11]. Figure 9 shows an induction BSG used in a 48 V electrical architecture.



Fig. 9 48 V induction BSG [7].

To make an asynchronous motor rotate, electrical power needs to be supplied only to the stator, as opposed to the DC motor whose rotor and stator windings both need to be power-supplied. When voltage is supplied to the stator of an asynchronous motor, the stator magnetic flux is generated due to the flow of current in the stator winding, which is essentially a coil. The magnetic flux from the stator crosses the short-circuited winding of the rotor, inducing an EMF due to Faraday's law of electromagnetic induction, which in turn results in current flow within rotor windings. With the current flowing through the rotor winding, another magnetic flux is generated, that of the rotor. Consequently, two magnetic fluxes exist, one of the stator windings

and one of the rotor windings, with the rotor flux lagging in respect to the stator flux. This is why these machines were named asynchronous. Because of the interaction between these two magnetic fluxes, the rotor will experience a torque which will compel it to rotate in the direction of the stator's rotating magnetic field. This is the working principle of both single and three phase asynchronous motors, which are often referred to as induction motors due to their operating principle being one of electromagnetic induction.

3.2. Speed – torque curve of an induction motor

Induction motor speed – torque curve, which is an important aspect in system design, is depicted on figure 10.

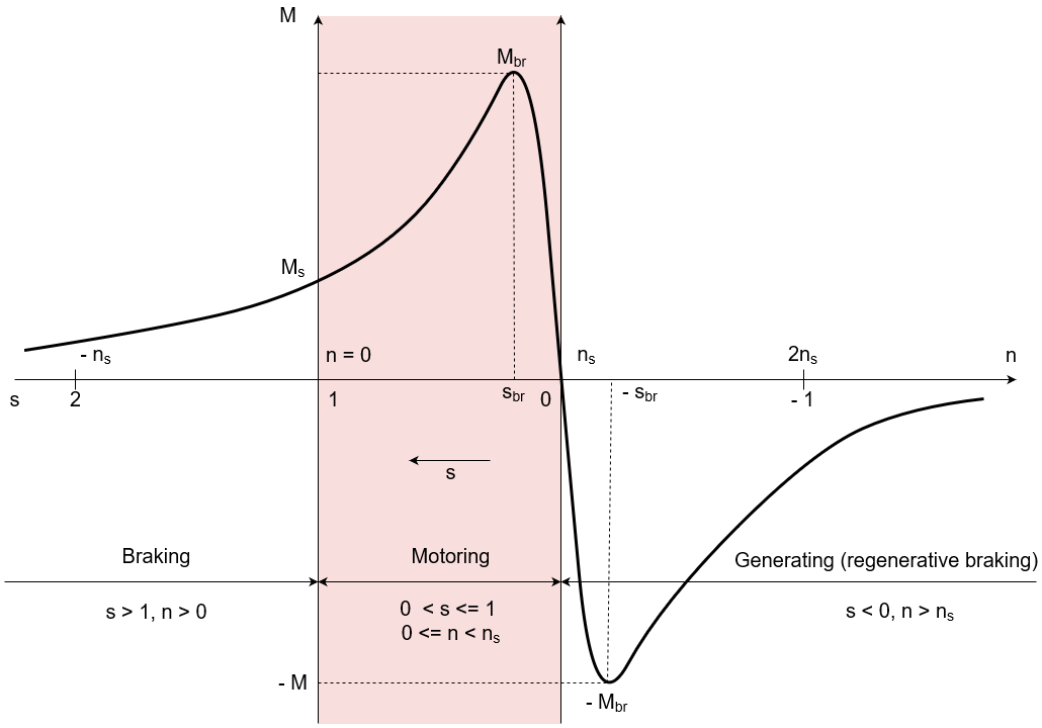


Fig. 10 Induction motor speed - toque curve

It can be observed from figure 10 that there are three operation modes an induction machine can appropriate: motoring, braking and generating (regenerative braking). The parameters defining each operation mode are torque M, rotor speed n and slippage s. Slippage is the measure of the difference between rotor speed and the speed of the rotating magnetic field of the stator, which is expressed in percentage [11]. In accordance with this, expression *(3.1)* defines the slippage for an arbitrary induction machine:

$$s = \frac{n_s - n}{n_s} \quad (3.1)$$

Since the BSG will be in motoring operation mode while performing stop/start and torque boosting functions, only the red shaded region of the speed – torque curve is of interest in the scope of this thesis.

Motoring region encompasses the region of speed – torque curve from zero speed ($n = 0$), in which the induction machine after being connected to an external power source develops starting torque M_s, which starts rotating the rotor. This marks the start of motor run – up during which the maximum torque is reached somewhere in between 70 – 90% synchronous speed n_s [11]. This maximum torque value is called breakaway torque M_{br}. After reaching breakaway torque the motor enters the stable region of operation, meaning that the running speed doesn't change much with load variation.

From the standpoint of torque boosting it is essential to keep the machine operating point in the high torque region so sufficient torque can be delivered. This is ensured by an automatic transmission which shifts gears when the induction machine enters the low torque – high speed region. It is important to note that gear shifting procedure is a compromise between the ICE and the induction machine in the respect of torque output, which will be shown in the later chapters.

As indicated by the literature [11], an induction motor can be of two types in the respect of rotor winding design:

1) Squirrel – cage type
2) Slip – ring type

In accordance with BSG application, the squirrel – cage induction motor [12] and a special slip – ring induction motor with claw poles [13] are considered in the next chapter.

3.3. Induction motor types for BSG application

3.3.1. Slip – ring claw – pole induction motor

The slip – ring claw – pole induction motor is a modification of a conventional alternator so it supports both motoring and generating modes of operation. The popularity of this type of induction machine is mainly due to its high pole pair number which results in increased torque density and its robust structure allowing for high speed operation [13]. The machine is equipped with the rotor winding supplied by the slip rings. Slip rings are used to close the electrical circuit of the rotor winding using external resistors with variable resistance. During start up, the

resistances are set to the highest values and when the rated speed is reached, the resistors are switched off and the winding is short-circuited.

The slip-ring claw-pole induction motor is hybrid excited, meaning that both the stator and rotor windings are supplied with voltage, so it is referred to as HECPG (Hybrid Excited Claw - Pole Generator) [14], only in this case it would be referred to as HECPSG (Hybrid Excited Claw – Pole Starter – Generator). Figure 11 shows the constitutive elements of a HECPSG.

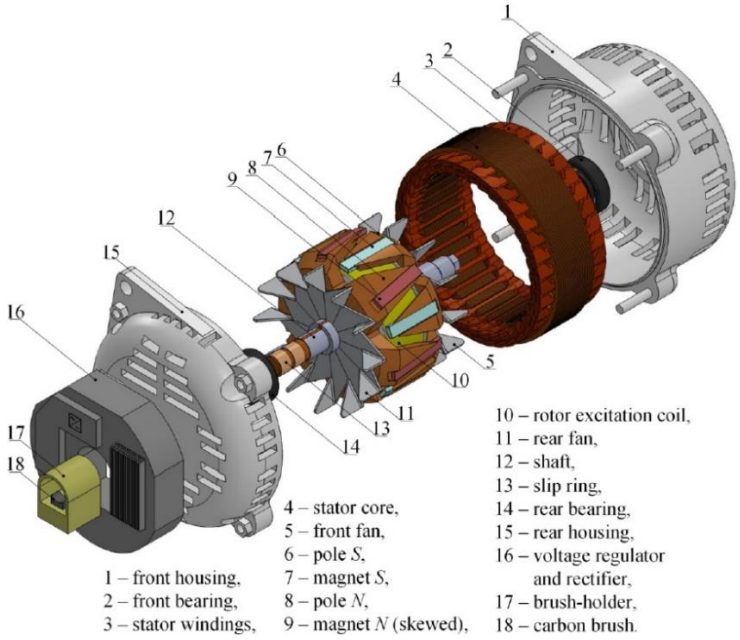


Fig. 11 HECPG [14]

Due to the uncertainty of the effect of hybrid excitation on the mathematical model of the induction machine, with the mathematical model being an integral part needed to design the control system for mitigation of timing belt vibrations, along with the unavailability of the appropriate scientific literature, the author of this thesis has made the decision to opt for an induction machine of squirrel – cage type. Developed control methods founded on the familiar mathematical model of the squirrel – cage motor, featured in a number of papers and other works, such as [10], [15], [16], [17], [18], [19] and [20] along with some research already done in the direction of the design of a squirrel – cage BSG [12] have facilitated this decision.

3.3.2. Squirrel – cage induction motor

The rotor winding of the squirrel-cage induction motor is designed as a cage, as opposed to the copper wire design found in the slip-ring version of the machine. Squirrel-cage induction motor doesn't use slip rings to close the rotor electrical circuit, which consequently makes the

rotor winding short-circuited at all times. The absence of slip rings implies the absence of slip ring contacts with the rotor shaft, which means there is no mechanical wear. The only mechanical parts of the squirrel-cage machine enduring wear are the bearings of the rotor shaft. Owning to such design, the squirrel-cage machine is the simplest, the cheapest, the lightest, the most reliable, and therefore the most widely used electrical machine [11].

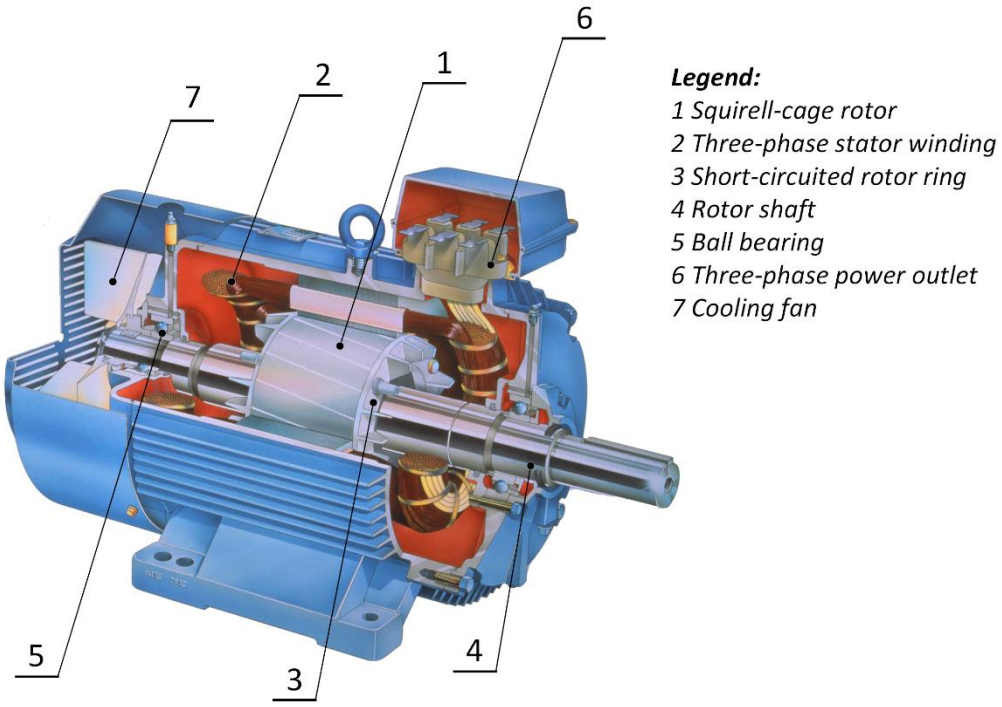


Fig. 12 Squirrel-cage induction motor

In this chapter the operating principle of the induction machine has been explained and insight into its design variants given, followed with the discussion concerning the utilization of the squirrel-cage machine for BSG application. In the upcoming chapter, the mathematical model of a squirrel-cage induction machine is derived after which the control system the mitigation of FEAD belt vibrations will be designed.

4. MATHEMATICAL MODEL OF BSG AS A SQUIRREL-CAGE MACHINE

4.1. Vector control

Vector control or field-field oriented control (FOC) is a control concept which enables the magnetic flux and torque of the induction machine to be controlled independently. Vector control was developed due to the inability of scalar control, which is based on the static model of the induction machine, to ensure that the magnetic flux of the machine, and also the torque, remain constant [20]. The following derivation of the vector control algorithm along with the mathematical model of the induction machine is well known and can be found in the literature referenced by [15], [16], [17], [18], [19], [20], [21].

The name vector control stems from the fact that any physical quantity rotating in a symmetrical three-phase system can be represented by an equivalent space vector carrying information about the amplitude, phase shift and angular frequency of that physical quantity. The three-phase system is considered to be symmetric if the total sum of its phase quantities (in this case a, b and c in a given time instant is equal to 0.

$$f_a(t) + f_b(t) + f_c(t) = 0, \tag{4.1}$$

where f is a symbol for an arbitrary phase quantity such as current, voltage, magnetic flux etc. Therefore, the phase-shifted physical quantities in a three-phase system are represented by the following expressions:

$$f_a = f_m \cos(\omega_f t), \tag{4.2}$$

$$f_a = f_m \cos\left(\omega_f t - \frac{2\pi}{3}\right), \tag{4.3}$$

$$f_a = f_m \cos\left(\omega_f t - \frac{4\pi}{3}\right), \tag{4.4}$$

where f_m is the amplitude of the physical quantity. Every three-phase variable is fully defined by its amplitude, frequency and phase shift. Every set of three-phase variables f_a, f_b and f_c can be represented by the resulting space vector $\bar{f}$. The resulting space vector $\bar{f}$ is obtained by means of vector addition of the phase variables in a given time instant:

$$\bar{f} = \frac{2}{3}(f_a + af_b + a^2 f_c) = f_a + e^{j\frac{2\pi}{3}} f_b + e^{j\frac{4\pi}{3}} f_c, \quad (4.5)$$

where a is an operator which transforms the 3-phase variables f_a, f_b and f_c from the time domain into a space vector,

$$a = e^{j\frac{2\pi}{3}} = -\frac{1}{2} + j\frac{\sqrt{3}}{2}, \quad (4.6)$$

$$a = e^{j\frac{4\pi}{3}} = -\frac{1}{2} - j\frac{\sqrt{3}}{2}. \quad (4.7)$$

To help illustrate this transformation, figure 13 shows the time instant corresponding to the angle of $\omega t = 45° = \frac{\pi}{4}$, that is $t = \frac{\pi}{4\omega}$ at which the phase values of the currents have been taken. Figure 14 shows the resulting space vector containing information about the amplitude, frequency and phase shift of the phase currents from figure 13. The angular frequency is $\omega = 1$ rad/s.

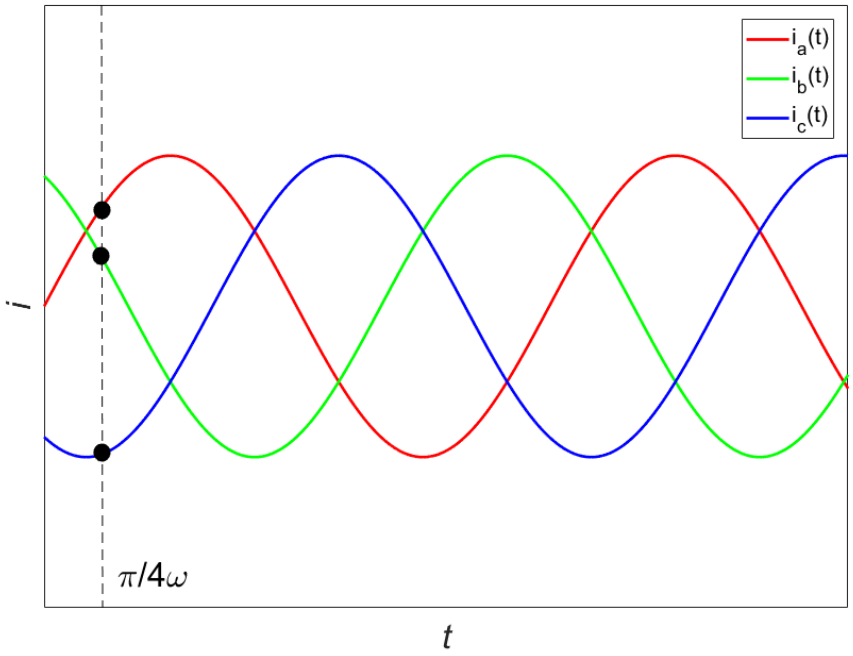


Fig. 13 Three-phase currents

$$i_a\left(\frac{\pi}{4\omega}\right) = \sqrt{2}I\cos\left(\frac{\pi}{4}\right) = I_m \quad (4.8)$$

$$i_b\left(\frac{\pi}{4\omega}\right) = \sqrt{2}I\cos\left(\frac{\pi}{4} - \frac{4\pi}{3}\right) = -0.966\sqrt{2}I_m \quad (4.9)$$

$$i_c\left(\frac{\pi}{4\omega}\right) = \sqrt{2}I\cos\left(\frac{\pi}{4} - \frac{4\pi}{3}\right) = -0.966\sqrt{2}I_m \quad (4.10)$$

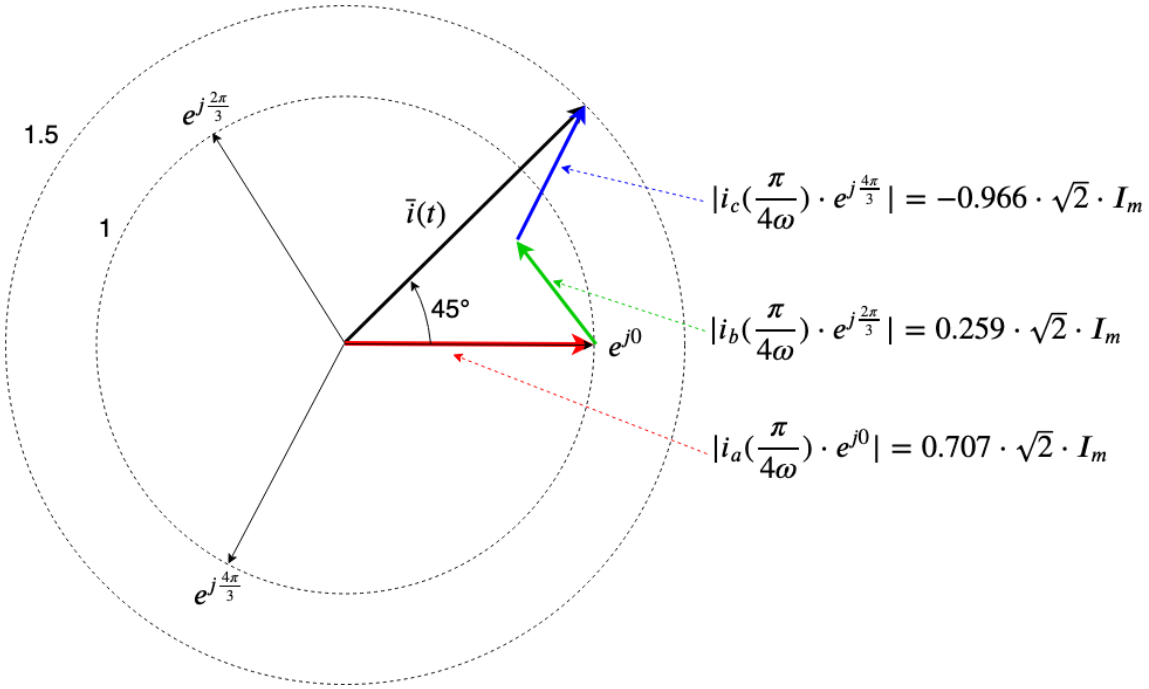


Fig. 14 Resulting space vector of phase currents (8),(9),(10)

Now, returning to the arbitrary notation (f instead of i), it is important to say that the resulting space vector $\bar{f}$ can be expressed in a two-dimensional orthogonal complex plane since its form given by *(4.5)* can be separated into the real and imaginary part:

$$\bar{f} = \frac{2}{3}(f_a + af_b + a^2 f_c) = f_\alpha + jf_\beta \ . \qquad (4.11)$$

This effectively reduces the three-phase system to a two-phase system without any loss of information. By equating the terms from the left and right side of the expression *(11)*, the relation between the 3-phase and 2-phase variables is obtained:

$$f_\alpha = \frac{2}{3}\left[f_a - \frac{1}{2}(f_b + f_c)\right], \qquad (4.12)$$

$$f_\beta = \frac{1}{\sqrt{3}}(f_b - f_c). \qquad (4.13)$$

4.1.1. Clarke transformation

The procedure of transforming variables from a 3-phase system to their 2-phase representations is called Clarke transformation. The importance of Clarke transformation is that it reduces the order of the mathematical model of an induction machine and enables the realization of the vector control algorithm [20] . Figure 15 shows arbitrary 3-phase variables transformed from their natural coordinate system into a 2-phase orthogonal complex plane by means of Clarke transformation, with the amplitude, angular frequency and phase shift identical to phase currents from figures 13 and 14. It can be clearly observed on figure 15 that the

resulting space vector $\bar{f}$ is at the same time the vector sum of its 3-phase space variables, as well as of its 2-phase space variables.

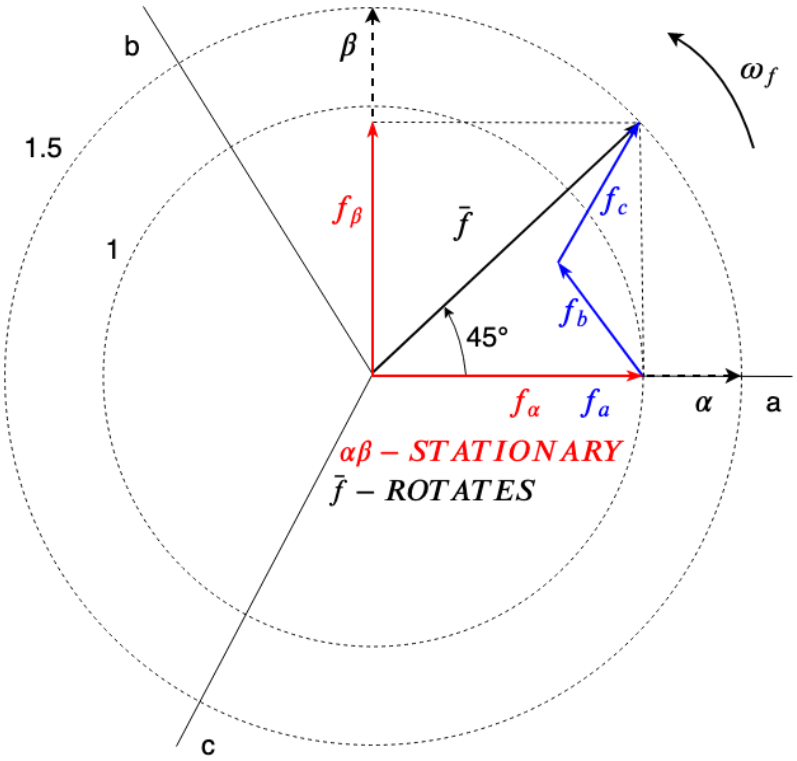


Fig. 15 Resulting space vector $\bar{f}$ as a vector sum of its 3-phase and 2-phase space variables

Expressions *(4.12)* and *(4.13)* can be written in matrix form

$$\begin{bmatrix} f_\alpha \\ f_\beta \end{bmatrix} = \frac{2}{3}\begin{bmatrix} 1 & -\frac{1}{2} & -\frac{1}{2} \\ 0 & \frac{\sqrt{3}}{2} & -\frac{\sqrt{3}}{2} \end{bmatrix}\begin{bmatrix} f_a \\ f_b \\ f_c \end{bmatrix}, \qquad (4.14)$$

which implies that the inverse Clarke transformation can be obtained,

$$\begin{bmatrix} f_a \\ f_b \\ f_c \end{bmatrix} = \frac{2}{3}\begin{bmatrix} 1 & 0 \\ -\frac{1}{2} & \frac{\sqrt{3}}{2} \\ -\frac{1}{2} & -\frac{\sqrt{3}}{2} \end{bmatrix}\begin{bmatrix} f_\alpha \\ f_\beta \end{bmatrix}. \qquad (4.15)$$

The 2-phase orthogonal $\alpha - \beta$ coordinate system is stationary and contains the resulting space vector $\bar{f}$, which rotates as its vector components obtain different magnitudes and orientation following the sin wave from figure 13. This consequently means that the phase variables f_α and f_β are still harmonic quantities, exactly like f_a, f_b and f_c and therefore can't be controlled by linear control methods.

4.1.2. Park transformation

Park transformation solves the problem of 2-phase $\alpha\beta$ variables being harmonic components, which makes them difficult to handle, and therefore unfavorable for control purposes. The Park transformation utilizes the fact that the rotating space vector such as $\bar{f}$ can be observed in a rotating coordinate system of an arbitrary angular velocity ω [20].

Furthermore, if the angular velocity ω of the rotating coordinate system, referred to as $d-q$ system, is equal to the angular velocity ω_f of the rotating space vector $\bar{f}$, then by decomposing the rotating space vector $\bar{f}$ in the $d-q$ coordinate system, one obtains the DC components of the space vector $\bar{f}$. The term DC is used here in a more unconstrained manner and it essentially means that the space vector components are time-independent when observed in the rotating coordinate system $d-q$ with an angular velocity $\omega = \omega_f$.

All input and output variables for the speed and current controllers of the induction machine will be referred in the $d-q$ system because they are time independent in respect to it, that is, they cease to be nonlinear harmonic variables, and thus become favorable for control operations. This is the core principle of vector control.

Figure 16 show the rotating space vector $\bar{f}$ decomposed on its harmonic components in the stationary $\alpha-\beta$ 2-phase orthogonal system and on its DC components in the rotating $d-q$ coordinate system, which rotates at an angular velocity of $\omega = \omega_f$.

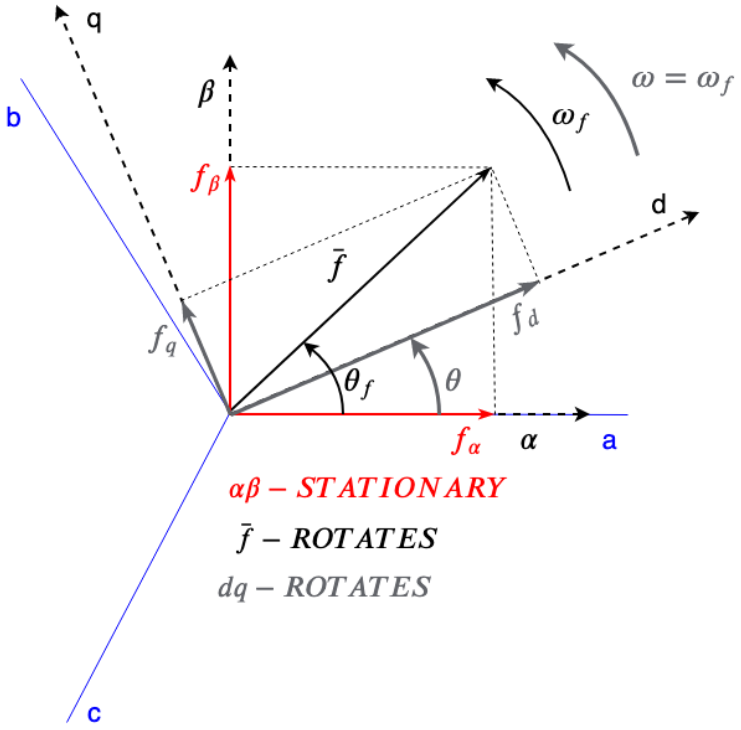


Fig. 16 Space vector $\bar{f}$ and its components in stationary and rotating 2-phase coordinate systems

The Park transformation which translates the 2-phase space vector components from the stationary $\alpha\beta$ system to the rotating $d-q$ system is expressed by:

$$\begin{bmatrix} f_d \\ f_q \end{bmatrix} = \begin{bmatrix} \cos\theta & \sin\theta \\ -\sin\theta & \cos\theta \end{bmatrix} \begin{bmatrix} f_\alpha \\ f_\beta \end{bmatrix}, \tag{4.16}$$

Where f_d is the real component of the space vector, f_q the imaginary component and θ the angle between the d axis of the $d-q$ system and the α axis of the $\alpha-\beta$ system. The inverse Park transformation can also be obtained:

$$\begin{bmatrix} f_\alpha \\ f_\beta \end{bmatrix} = \begin{bmatrix} \cos\theta & -\sin\theta \\ \sin\theta & \cos\theta \end{bmatrix} \begin{bmatrix} f_d \\ f_q \end{bmatrix}. \tag{4.17}$$

It is important to note that if the angular velocity ω of the $d-q$ system is not equal to the angular velocity ω_f of the space vector $\bar{f}$, its real component f_d and its imaginary component f_q are harmonic signals, whose angular frequency is a function of the difference between ω and ω_f, and thus are not viable for control applications. This implies that the necessary condition for the vector control algorithm to work is the correct information about the value of ω_f.

4.1.3. Putting the significance of vector control into context by using an analogy with the DC machine

The DC machine magnetic flux Φ_e generated by the excitation current i_e is perpendicular in respect to the magnetic flux Φ_a generated by the armature current i_a [20], as indicated by figure 17.

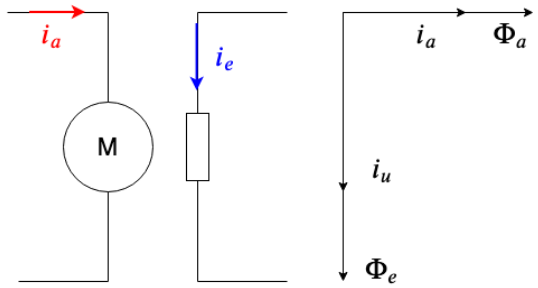


Fig. 17 Armature and excitation circuit of a DC machine

The torque of the DC machine is expressed as

$$m_{DC} = k_m i_a \Phi_e = k'_m i_a i_e. \tag{4.18}$$

Perpendicular phase quantities in the context of an electrical machine are considered decoupled, which for the DC machine means that the excitation current i_e effects only the excitation flux Φ_e and the armature current i_a effects only the armature flux Φ_a. This phenomenon enables

the excitation and armature fluxes to be controlled without respect to each other, which essentially means that the torque of the DC machine can be controlled independently of the magnetic field needed to excite the machine. The described system in which the excitation flux and torque of the electrical machine are controlled independently can be fully obtained with an induction machine by using the vector control algorithm.

This fact combined with the properties of the squirrel-cage induction machine being the simplest, the cheapest, the lightest, and the most reliable has led to the DC machine being almost completely abandoned by the industry in the low to mid-power segment. The torque expression for and induction machine reads as follows

$$m_{IM} = k_m i_{sq} \Psi_r = k'_m i_{sq} i_{sd}, \qquad (4.19)$$

where i_{sd} is the stator field current (i_d – fiel**d**), Ψ_r the magnetic flux of the rotor and i_{sq} stator torque current (i_q - tor**q**ue). It can be observed from expressions *(4.18)* and (*4.19)* that there is an equivalence between the currents which is denoted by the table 1

Table 1 Equivalence between DC and induction machine currents

	Field component	Torque component
DC machine	i_e	i_a
Induction machine	i_{sd}	i_{sq}

The equivalence of currents in table 1 implies the equivalence of machine torque expressions that those currents comprise from the standpoint of control. Expressions *(4.18)* and *(4.19)* represent linear physical systems on which linear control methods based on PI control may be used.

The designed control system will have have to include three PI controllers, one for BSG speed, one for the stator filed current i_{sd} and one for stator torque current i_{sq}. The reason why the rotor flux Ψ_r controller has been omitted will be explained later on. In order to tune the PI controllers analytically, the mathematical model of the induction machine needs to be derived.

The mathematical model of an induction machine is not appropriate for analytical tuning when represented in its natural 3-phase coordinate system. This is due to the model being non-linear and of high order. Using the tools described in chapter 4.1. this model will be transformed into its linear form which facilitates analytical tuning necessary to obtain a system which

mitigates BSG vibrations, and therefore timing belt vibrations. In the following chapter the mathematical model of BSG as a squirrel-cage machine is derived.

4.2. Mathematical model of BSG in its natural coordinate system

The mathematical model of an induction machine is comprised of algebraic and differential equations describing electromagnetic and mechanical phenomena in the machine. For the purposes of using the vector control method the following assumptions are made [15]:

- the phase windings are symmetrical
- saturation and iron core losses are neglectable
- the magnetic flux in the air gap is of the sinusoidal waveform
- machine temperature is constant

In accordance with given assumptions, the induction machine stator and rotor voltage equations are firstly given in the three-phase $a-b-c$ coordinate system, which is the natural coordinate system of the machine. Figure 18 shows the three axes of the stator phase variables making up the three-phase stator coordinate system, as well as the three axes of the rotor phase variables defining the 3-phase rotor coordinate system. The coordinate systems of stator and rotor variables are phase shifted by an electrical angle ε.

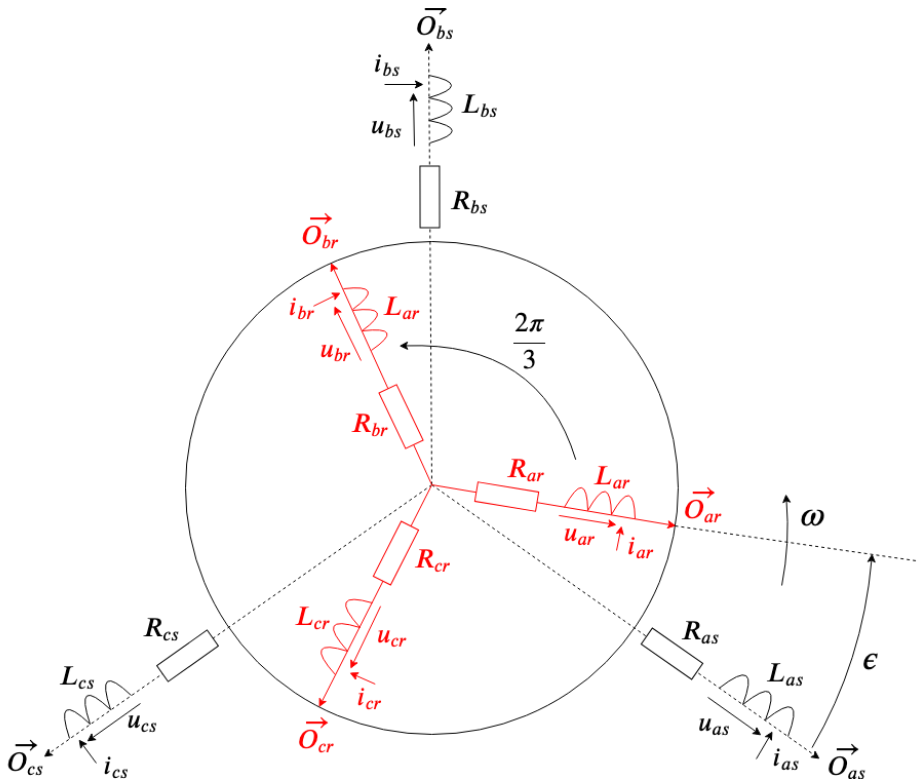


Fig. 18 Induction machine in 3-phase coordinate system

Since rotor and stator phase windings are symmetrical the following is true:

$$i_{as} + i_{bs} + i_{cs} = 0, \tag{4.20}$$

$$i_{ar} + i_{br} + i_{cr} = 0. \tag{4.21}$$

Additionally, the stator and rotor phase resistances, as well as inductances are equal:

$$R_{as} = R_{bs} = R_{cs} = R_s, \tag{4.22}$$

$$R_{ar} = R_{br} = R_{cr} = R_r, \tag{4.23}$$

$$L_{as} = L_{bs} = L_{cs} = L_{ps}, \tag{4.24}$$

$$L_{ar} = L_{br} = L_{cr} = L_{pr}. \tag{4.25}$$

In accordance with this, the differential equations describing the electrical circuit of each stator and rotor phase read as follows:

$$\begin{bmatrix} u_{as} \\ u_{bs} \\ u_{cs} \end{bmatrix} = R_s \begin{bmatrix} i_{as} \\ i_{bs} \\ i_{cs} \end{bmatrix} + \frac{d}{dt} \begin{bmatrix} \psi_{as} \\ \psi_{bs} \\ \psi_{cs} \end{bmatrix}, \tag{4.26}$$

$$\begin{bmatrix} u_{ar} \\ u_{br} \\ u_{cr} \end{bmatrix} = R_r \begin{bmatrix} i_{ar} \\ i_{br} \\ i_{cr} \end{bmatrix} + \frac{d}{dt} \begin{bmatrix} \psi_{ar} \\ \psi_{br} \\ \psi_{cr} \end{bmatrix}. \tag{4.27}$$

The magnetic flux in each phase is generated by interaction between all the stator and rotor currents. Stator fluxes form *(4.26)* read as follows:

$$\psi_{as} = L_{ps} i_{as} + M_s i_{bs} + M_s i_{cs} + M_{sr}\left(cos(\epsilon) i_{ar} + cos\left(\epsilon + \tfrac{2\pi}{3}\right) i_{br} + cos\left(\epsilon - \tfrac{2\pi}{3}\right) i_{cr}\right), \tag{4.28}$$

$$\psi_{bs} = L_{ps} i_{bs} + M_s i_{cs} + M_s i_{as} + M_{sr}\left(cos(\epsilon) i_{br} + cos\left(\epsilon + \tfrac{2\pi}{3}\right) i_{cr} + cos\left(\epsilon - \tfrac{2\pi}{3}\right) i_{ar}\right), \tag{4.29}$$

$$\psi_{cs} = L_{ps} i_{cs} + M_s i_{as} + M_s i_{bs} + M_{sr}\left(\cos(\epsilon) i_{cr} + \cos\left(\epsilon + \tfrac{2\pi}{3}\right) i_{ar} + \cos\left(\epsilon - \tfrac{2\pi}{3}\right) i_{br}\right), \tag{4.30}$$

where L_{ps} is the stator inductance of each phase comprised of the magnetizing stator inductance L_{ms} and leakage stator inductance $L_{\sigma s}$:

$$L_{ps} = L_{ms} + L_{\sigma s}\ . \tag{4.31}$$

The mutual inductance of two stator phases M_s is expressed as:

$$M_s = L_{ms}\, cos\left(\tfrac{2\pi}{3}\right) = -\tfrac{1}{2} L_{ms}\ , \tag{4.32}$$

and M_{sr} is the maxumum mutual inductance of stator and rotor phases achieved when the corresponding stator and rotor phases are colinear ($\epsilon = 0\, rad$).

Basically, equations *(4.28)-(4.30)* state that the magnetic flux of each stator phase (applies also to the rotor phases) is generated due to three different interactions, as shown on *(4.28)*:

$$\psi_{as} = \underbrace{L_{ps} i_{as}}_{Self\ inductance} + \underbrace{M_s i_{bs} + M_s i_{cs}}_{Mutual\ inductance\ between\ stator\ phases} + \underbrace{M_{sr}\left(cos(\epsilon) i_{ar} + cos\left(\epsilon + \frac{2\pi}{3}\right) i_{br} + cos\left(\epsilon - \frac{2\pi}{3}\right) i_{cr}\right)}_{Mutual\ inductance\ betwen\ \ stator\ and\ rotor\ \ phases}.$$

Equations *(4.28)-(4.30)* can be written in matrix form taking *(4.31)* into account:

$$\begin{bmatrix} \psi_{as} \\ \psi_{bs} \\ \psi_{cs} \end{bmatrix} = \begin{bmatrix} L_{ps} & -\frac{1}{2}L_{ms} & -\frac{1}{2}L_{ms} \\ -\frac{1}{2}L_{ms} & L_{ps} & -\frac{1}{2}L_{ms} \\ -\frac{1}{2}L_{ms} & -\frac{1}{2}L_{ms} & L_{ps} \end{bmatrix} \begin{bmatrix} i_{as} \\ i_{bs} \\ i_{cs} \end{bmatrix} + M_{sr} T(\epsilon) \begin{bmatrix} i_{ar} \\ i_{br} \\ i_{cr} \end{bmatrix}, \qquad (4.33)$$

where $T(\epsilon)$ is:

$$T(\epsilon) = \begin{bmatrix} cos(\epsilon) & cos\left(\epsilon + \frac{2\pi}{3}\right) & cos\left(\epsilon - \frac{2\pi}{3}\right) \\ cos\left(\epsilon - \frac{2\pi}{3}\right) & cos(\epsilon) & cos\left(\epsilon + \frac{2\pi}{3}\right) \\ cos\left(\epsilon + \frac{2\pi}{3}\right) & cos\left(\epsilon - \frac{2\pi}{3}\right) & cos(\epsilon) \end{bmatrix}. \qquad (4.34)$$

Due to the symmetry of the windings, expressions *(4.28) - (4.30)* can be simplified by applying the following equations stemming from *(4.20)* and *(4.21):*

$$i_{as} = -i_{bs} - i_{cs}\ , \qquad i_{ar} = -i_{br} - i_{cr}\ , \qquad (4.35)$$

$$i_{bs} = -i_{as} - i_{cs}\ , \qquad i_{br} = -i_{ar} - i_{cr}\ , \qquad (4.36)$$

$$i_{cs} = -i_{as} - i_{bs}\ , \qquad i_{cr} = -i_{ar} - i_{br}\ . \qquad (4.37)$$

After applying *(4.35)* to *(4.28)*, *(4.36)* to *(4.29)* and *(4.37)* to *(4.30)* the following simplification is obtained, expressed in the matrix form:

$$\begin{bmatrix} \psi_{as} \\ \psi_{bs} \\ \psi_{cs} \end{bmatrix} = L_s \begin{bmatrix} i_{as} \\ i_{bs} \\ i_{cs} \end{bmatrix} + M_{sr} T(\epsilon) \begin{bmatrix} i_{ar} \\ i_{br} \\ i_{cr} \end{bmatrix}, \qquad (4.38)$$

where L_s is defined by:

$$L_s = L_{ps} + \frac{1}{2}L_{ms} = \frac{3}{2}L_{ms} + L_{\sigma s}\,. \tag{4.39}$$

The described procedure is repeated on the flux equations of the rotor windings:

$$\psi_{ar} = L_{pr}i_{ar} + M_r i_{br} + M_r i_{cr} + M_{sr}\left(cos(\epsilon)i_{as} + cos\left(\epsilon + \frac{2\pi}{3}\right)i_{bs} + cos\left(\epsilon - \frac{2\pi}{3}\right)i_{cs}\right), \tag{4.40}$$

$$\psi_{br} = L_{pr}i_{br} + M_r i_{cr} + M_r i_{ar} + M_{sr}\left(cos(\epsilon)i_{bs} + cos\left(\epsilon + \frac{2\pi}{3}\right)i_{cs} + cos\left(\epsilon - \frac{2\pi}{3}\right)i_{as}\right), \tag{4.41}$$

$$\psi_{cr} = L_{pr}i_{cr} + M_r i_{ar} + M_r i_{br} + M_{sr}\left(cos(\epsilon)i_{cs} + cos\left(\epsilon + \frac{2\pi}{3}\right)i_{as} + cos\left(\epsilon - \frac{2\pi}{3}\right)i_{bs}\right), \tag{4.42}$$

where L_{pr} is the rotor inductance of each phase comprised of the magnetizing rotor inductance L_{mr} and leakage rotor inductance $L_{\sigma r}$:

$$L_{pr} = L_{mr} + L_{\sigma r}\,, \tag{4.43}$$

The matrix form of equations *(4.40)-(4.42)* is then obtained:

$$\begin{bmatrix}\psi_{ar}\\ \psi_{br}\\ \psi_{cr}\end{bmatrix} = \begin{bmatrix} L_{pr} & -\frac{1}{2}L_{mr} & -\frac{1}{2}L_{mr}\\ -\frac{1}{2}L_{mr} & L_{pr} & -\frac{1}{2}L_{mr}\\ -\frac{1}{2}L_{mr} & -\frac{1}{2}L_{mr} & L_{ps}\end{bmatrix}\begin{bmatrix}i_{ar}\\ i_{br}\\ i_{cr}\end{bmatrix} + M_{sr}T^T(\epsilon)\begin{bmatrix}i_{ar}\\ i_{br}\\ i_{cr}\end{bmatrix} \tag{4.44}$$

Expressions *(4.40)-(4.42)* can be simplified by applying *(4.35)-(4.37)* in the same manner as for the stator, which yields the following matrix form:

$$\begin{bmatrix}\psi_{ar}\\ \psi_{br}\\ \psi_{cr}\end{bmatrix} = L_r\begin{bmatrix}i_{ar}\\ i_{br}\\ i_{cr}\end{bmatrix} + M_{sr}T^T(\epsilon)\begin{bmatrix}i_{as}\\ i_{bs}\\ i_{cs}\end{bmatrix}, \tag{4.45}$$

where L_r is defined by:

$$L_r = L_{pr} + \frac{1}{2}L_{mr} = \frac{3}{2}L_{mr} + L_{\sigma r}\,. \tag{4.46}$$

This concludes the derivation of the mathematical model of the BSG in its natural 3-phase system which is comprised of 12 differential equations of the first order describing electromagnetic phenomena in the machine. When the equation desribing the rotor dynamics is added, the total order of the system becomes 13. To conclude this chapter, the aformentioned model without rotor dynamis is given in the following page.

BSG model in 3-phase coordinate system:

$$\begin{bmatrix} u_{as} \\ u_{bs} \\ u_{cs} \end{bmatrix} = R_s \begin{bmatrix} i_{as} \\ i_{bs} \\ i_{cs} \end{bmatrix} + \frac{d}{dt} \begin{bmatrix} \psi_{as} \\ \psi_{bs} \\ \psi_{cs} \end{bmatrix}, \tag{4.47}$$

$$\begin{bmatrix} u_{ar} \\ u_{br} \\ u_{cr} \end{bmatrix} = R_r \begin{bmatrix} i_{ar} \\ i_{br} \\ i_{cr} \end{bmatrix} + \frac{d}{dt} \begin{bmatrix} \psi_{ar} \\ \psi_{br} \\ \psi_{cr} \end{bmatrix}, \tag{4.48}$$

$$\begin{bmatrix} \psi_{as} \\ \psi_{bs} \\ \psi_{cs} \end{bmatrix} = L_s \begin{bmatrix} i_{as} \\ i_{bs} \\ i_{cs} \end{bmatrix} + M_{sr} T(\epsilon) \begin{bmatrix} i_{ar} \\ i_{br} \\ i_{cr} \end{bmatrix}, \tag{4.49}$$

$$\begin{bmatrix} \psi_{ar} \\ \psi_{br} \\ \psi_{cr} \end{bmatrix} = L_r \begin{bmatrix} i_{ar} \\ i_{br} \\ i_{cr} \end{bmatrix} + M_{sr} T^T(\epsilon) \begin{bmatrix} i_{as} \\ i_{bs} \\ i_{cs} \end{bmatrix}, \tag{4.50}$$

$$T(\epsilon) = \begin{bmatrix} cos(\epsilon) & cos\left(\epsilon + \frac{2\pi}{3}\right) & cos\left(\epsilon - \frac{2\pi}{3}\right) \\ cos\left(\epsilon - \frac{2\pi}{3}\right) & cos(\epsilon) & cos\left(\epsilon + \frac{2\pi}{3}\right) \\ cos\left(\epsilon + \frac{2\pi}{3}\right) & cos\left(\epsilon - \frac{2\pi}{3}\right) & cos(\epsilon) \end{bmatrix}, \tag{4.51}$$

$$L_s = L_{ps} + \frac{1}{2} L_{ms} = \frac{3}{2} L_{ms} + L_{\sigma s}\,, \tag{4.52}$$

$$L_r = L_{pr} + \frac{1}{2} L_{mr} = \frac{3}{2} L_{mr} + L_{\sigma r}\,. \tag{4.53}$$

In the following chapter the BSG model described by equations *(4.47)* - *(4.53)* is transformed using Clarke and Park transformations presented in chapter 4.1. into a form suitable for the analytical tuning of the speed and current control systems based on vector control.

4.3. Mathematical model of BSG suitable for vector control

4.3.1. Transformation of BSG phase variables into space vectors

To start things off, the rotating space vector concept $\bar{f}$, that is, the Clarke transformation is applied to all phase variables of the BSG model *(4.47)* - *(4.53)*. This results in all of the phase variable being expressed as space vectors like *(5)*:

$$\bar{u}_s = \frac{2}{3}\left(u_{as} + u_{bs}e^{j\frac{2\pi}{3}} + u_{cs}e^{j\frac{4\pi}{3}}\right), \quad (4.54)$$

$$\bar{\imath}_s = \frac{2}{3}\left(i_{as} + i_{bs}e^{j\frac{2\pi}{3}} + i_{cs}e^{j\frac{4\pi}{3}}\right), \quad (4.55)$$

$$\bar{\psi}_s = \frac{2}{3}\left(\psi_{as} + \psi_{bs}e^{j\frac{2\pi}{3}} + \psi_{cs}e^{j\frac{4\pi}{3}}\right), \quad (4.56)$$

$$\bar{u}_r = \frac{2}{3}\left(u_{ar} + u_{br}e^{j\frac{2\pi}{3}} + u_{cr}e^{j\frac{4\pi}{3}}\right), \quad (4.57)$$

$$\bar{\imath}_r = \frac{2}{3}\left(i_{ar} + i_{br}e^{j\frac{2\pi}{3}} + i_{cr}e^{j\frac{4\pi}{3}}\right), \quad (4.58)$$

$$\bar{\psi}_r = \frac{2}{3}\left(\psi_{ar} + \psi_{br}e^{j\frac{2\pi}{3}} + \psi_{cr}e^{j\frac{4\pi}{3}}\right), \quad (4.59)$$

and using these space vectors, the mathematical model of BSG in space vector notation is obtained:

$$\bar{u}_s = R_s\bar{\imath}_s + \frac{d\bar{\psi}_s}{dt}, \quad (4.60)$$

$$\bar{u}_r = R_r\bar{\imath}_r + \frac{d\bar{\psi}_r}{dt}, \quad (4.61)$$

$$\bar{\psi}_s = L_s\bar{\imath}_s + L_m\bar{\imath}_r e^{j\epsilon}, \quad (4.62)$$

$$\bar{\psi}_r = L_r\bar{\imath}_r + L_m\bar{\imath}_s e^{-j\epsilon}. \quad (4.63)$$

,

where L_m is the stator – rotor inductive coupling defined by

$$L_m = \frac{3}{2}M_{sr}\,. \quad (4.64)$$

Although being space vectors, expressions *(4.60)* and *(4.62)* are referred to the stationary 2-phase $\alpha\beta$ orthogonal coordinate system of the stator, while *(4.61)* and *(4.63)* are referred to that of the rotor. This means that *(4.60)* and *(4.62)* are decoupled from *(4.61)* and *(4.63)*, while simultaneously describing electromagnetic occurrences in the same machine. To couple them in a single mathematical model they need to be transformed into a shared coordinate system. The following is done by means of Park transformation.

4.3.2. Transformation of BSG variables expressed as space vectors into a shared coordinate system

To recapitulate, the objective of transforming the two models described by *(4.60)* - *(4.63)* in a shared, rotating $d-q$ coordinate system is to obtain a model of an induction machine suitable for vector control. As mentioned in chapter 4.1.2., if the angular velocity ω of the rotating $d-q$ system is equal to the angular velocity ω_f of an arbitrary space vector $\bar{f}$, then the $d-q$ components of that space vector are DC-valued, i.e. time invariant under steady-state conditions, and thus suitable utilization of linear control methods such as PI control. When $\omega = \omega_f$ it is said that the $d-q$ system is synchronized with the space vector $\bar{f}$.

Vector control method states that the rotating $d-q$ system should be synchronized with the space vector of the rotor magnetic flux $\bar{\psi}_r$, that is of the rotor magnetic filed. It now becomes clear why this method is also known as field-oriented control (FOC). The synchronization of the $d-q$ system with the rotor flux vector $\bar{\psi}_r$ implies that the abscissa of the rotating system (the **d** axis, fiel**d** axis) is set coaxially in respect to it, as can be observed on Figure 19.

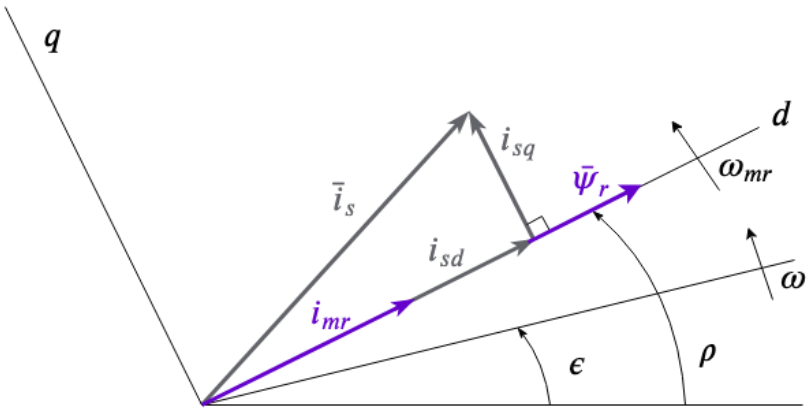


Fig. 19 Rotating dq system synchronized with the rotor flux space vector $\bar{\psi}_r$

ρ	angle between the stator coordinate system and the dq system
$\rho - \epsilon$	angle between the rotor coordinate system and the dq system
ϵ	angle betweent the stator and rotor coordinate systems
ω	angular velocity of the rotor
ω_{mr}	angular velocity of the rotor flux vector $\bar{\psi}_r$ / rotating $d-q$ system
i_{mr}	Magnetizing current that generates the rotor magnetic field

Since rotor flux vector $\bar{\psi}_r$ is set on the real axis of the $d-q$ coordinate system it can be defined

as follows:

$$\bar{\psi}_r = \psi_{rd} + j0\,, \tag{4.65}$$

which means that magnetizing current space vector $\bar{\imath}_{mr}$ is defined as

$$\bar{\imath}_{mr} = \frac{\bar{\psi}_r}{L_m} = \frac{\psi_{rd}}{L_m} + j0 = \frac{\psi_{rd}}{L_m}. \tag{4.66}$$

In order to transform an arbitrary rotating space vector $\bar{f}$ from the $\alpha - \beta$ stationary coordinate system into the rotating $d - q$ coordinate system, the following operation is applied:

$$\bar{f}_k = \bar{f} e^{-j\beta} \tag{4.67}$$

where $\bar{f}_k$ denotes an arbitrary space vector referred to the rotating $d - q$ system and β is the angle between the stationary coordinate system of the space vector $\bar{f}$ and the rotating $d - q$ system. In the case of the induction machine, angle β can obtain two values depending on whether space vectors belonging to the stator or to the rotor are being transformed into the $d - q$ system:

$$\beta_{stator} = \rho, \tag{4.68}$$

$$\beta_{rotor} = \rho - \epsilon\,. \tag{4.69}$$

As mentioned in this chapter the rotating $d - q$ frame needs to be synchronized with the rotor flux vector $\bar{\psi}_r$ which defines the angle ρ as:

$$\omega_{mr} = \frac{d\rho}{dt}\,. \tag{4.70}$$

This implies that the necessary condition for the vector control algorithm to work is the correct estimation of angle ρ. Now, by applying *(4.67)* to *(4.54) – (4.59)* the space vectors belonging to the stationary stator and rotor coordinate systems are referred to the $d - q$ system:

$$\bar{u}_{sk} = \bar{u}_s e^{-j\rho}\,, \tag{4.71}$$

$$\bar{\imath}_{sk} = \bar{\imath}_s e^{-j\rho}\,, \tag{4.72}$$

$$\bar{\psi}_{sk} = \bar{\psi}_s e^{-j\rho}\,, \tag{4.73}$$

$$\bar{u}_{rk} = \bar{u}_r e^{-j(\rho-\varepsilon)}\,, \tag{4.74}$$

$$\bar{\imath}_{rk} = \bar{\imath}_r e^{-j(\rho-\varepsilon)}\,, \tag{4.75}$$

$$\psi_{rk} = \bar{\psi}_r e^{-j(\rho-\varepsilon)}\,, \tag{4.76}$$

Using *(4.71) – (4.76)* the mathematical model of the both stator and the rotor of an induction machine referring to the same $d-q$ coordinate system synchronized with the rotor flux vector $\bar{\psi}_r$ is obtained. The fact that $\bar{u}_r = 0$ for the case of the squirrel-cage machine is also taken into consideration:

$$\bar{u}_{sk} = \bar{\imath}_{sk} R_s + \frac{d\bar{\psi}_{sk}}{dt} + j\bar{\psi}_{sk}\omega_{mr} \,, \tag{4.77}$$

$$0 = \bar{\imath}_{rk} R_s + \frac{d\bar{\psi}_{rk}}{dt} + j\bar{\psi}_{rk}(\omega_{mr} - \omega) \,, \tag{4.78}$$

$$\bar{\psi}_{sk} = L_s \bar{\imath}_{sk} + L_m \bar{\imath}_{rk} \,, \tag{4.79}$$

$$\bar{\psi}_{rk} = L_r \bar{\imath}_{rk} + L_m \bar{\imath}_{sk} \,, \tag{4.80}$$

where $j\bar{\psi}_{sk}\omega_k$ and $j\bar{\psi}_{rk}(\omega_k - \omega)$ terms represent the electromotive force EMF. To complete the mathematical model the electric torque of the machine needs to be defined. The torque of an induction machine is expressed as a vector product of the stator current $\bar{\imath}_{sk}$ and the stator flux $\bar{\psi}_{sk}$ resulting space vectors or of the rotor current $\bar{\imath}_{rk}$ and the rotor flux $\bar{\psi}_{rk}$ resulting space vectors. These two expressions yield the resulting torque vectors of the same magnitude, but of opposite orientations:

$$\bar{m}_e = -\frac{3}{2} p\bar{\psi}_{sk} \times \bar{\imath}_{sk} = \frac{3}{2} p\bar{\psi}_{rk} \times \bar{\imath}_{rk} \,, \tag{4.81}$$

and after taking into account *(4.79)* and *(4.80)* the torque is expressed as a vector product of the stator and rotor current resulting space vectors:

$$\bar{m}_e = -\frac{3}{2} p L_m \bar{\imath}_{rk} \times \bar{\imath}_{sk} = \frac{3}{2} p L_m \bar{\imath}_{sk} \times \bar{\imath}_{rk} \,. \tag{4.82}$$

After adding the rotor dynamics equation

$$J\frac{d\omega}{dt} = m_e - m_t \,, \tag{4.83}$$

and the relation between the mechanical angular velocity of the rotor and electrical angular velocity of the rotor flux:

$$\omega = p\omega_m \,, \tag{4.84}$$

the model of the machine which couples the stator and rotor electrical and mechanical description in a shared rotating coordinate system synchronized with the rotor flux $\bar{\psi}_r$ space vector can be considered completed. The model is summarized in on the following page.

BSG model in a shared coordinate system synchronized with the rotor flux vector:

Differential equations:

$$\bar{u}_{sk} = \bar{\imath}_{sk} R_s + \frac{d\bar{\psi}_{sk}}{dt} + j\bar{\psi}_{sk}\omega_{mr} \,, \tag{4.85}$$

$$0 = \bar{\imath}_{rk} R_s + \frac{d\bar{\psi}_{rk}}{dt} + j\bar{\psi}_{rk}(\omega_{mr} - \omega) \,, \tag{4.86}$$

$$J\frac{d\omega}{dt} = m_e - m_t \,, \tag{4.87}$$

Algebraic equations

$$\bar{\psi}_{sk} = L_s\bar{\imath}_{sk} + L_m\bar{\imath}_{rk} \,, \tag{4.88}$$

$$\bar{\psi}_{rk} = L_r\bar{\imath}_{rk} + L_m\bar{\imath}_{sk} \,, \tag{4.89}$$

$$\bar{m}_e = -\frac{3}{2}pL_m\bar{\imath}_{rk} \times \bar{\imath}_{sk} = \frac{3}{2}pL_m\bar{\imath}_{sk} \times \bar{\imath}_{rk} \,, \tag{4.90}$$

$$\omega = p\omega_m \,. \tag{4.91}$$

Now, having referred the stator and rotor voltage equations to the same coordinate system, they can be decomposed into their d and q components, which is the final step in the procedure for obtaining the induction machine model favorable for analytical tuning of the control system for the mitigation of FEAD vibrations. However, due to the rotor of the squirrel-cage machine being short circuited, its voltage is 0, as indicated by *(4.86)*, which means that rotor flux $\bar{\psi}_r$ and machine torque $\bar{m}_e$ will be controlled via the stator voltage d and q components, that is u_{sd} and u_{sq} respectively. After the stator voltage equation *(4.85)* has been decomposed into its u_{sd} and u_{sq} components, the decoupled nature of rotor magnetic flux and machine torque control, just like in the case of the DC machine, will become apparent. Before performing this decomposition, a short discussion concerning the hardware enabling this type of control is presented in the following chapter.

4.3.3. Voltage source inverter (VSI)

The voltage source inverter (VSI) is the hardware required in order to control the magnetic flux of the rotor $\bar{\psi}_r$ and torque $\bar{m}_e$ of the squirrel-cage induction machine with the d and q component of its stator voltage $\bar{u}_{sk}$ [15]. The conventional voltage source inverter is a DC-AC buck converter, which means that the output voltage is limited below the voltage of the DC source [12], in this case of the 48 V battery powering the BSG of a MHEV. The topology of a conventional VSI is shown on figure 20.

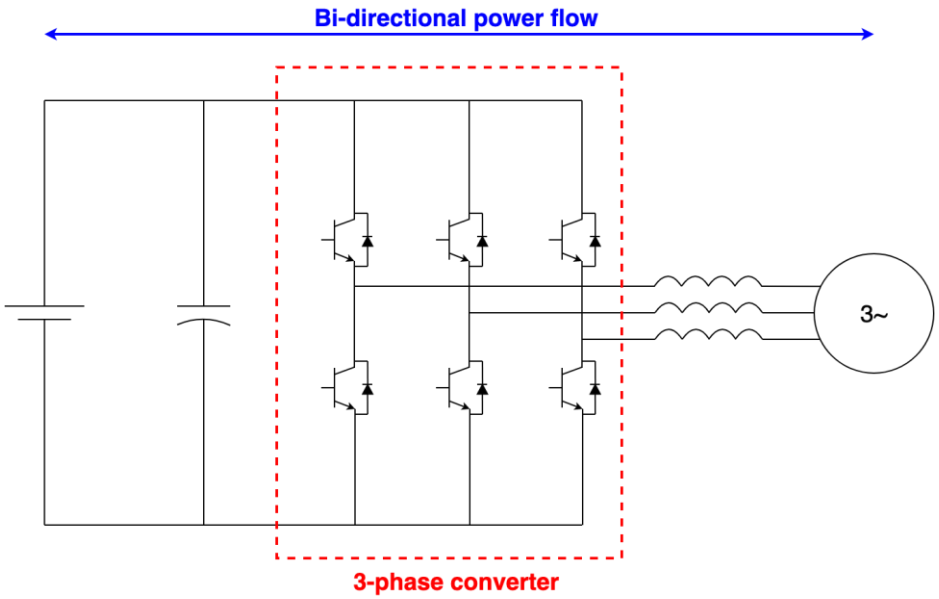


Fig. 20 Bi-directional VSI

The VSI voltage response dynamics with respect to the reference will be modelled in this thesis by an approximation in the form of a PT_1 (first-order lag) term characterized by the inverter voltage response lag (time constant). The response of and arbitrary PT_1 term is shown in figure 21.

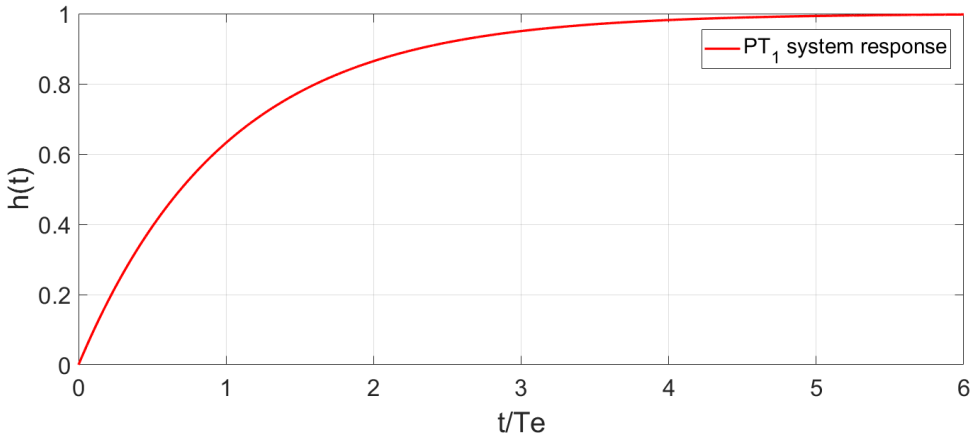


Fig. 21 PT_1 system response

The actual model of a 3-phase inverter control system is based on the following [21]:

- transformation of the phase variables from their natural coordinate system in the rotating $d-q$ system
- dual PI current controllers and dual PI active and reactive power controllers
- system for the synchronization with the 3-phase load based on the $d-q$ PLL algorithm

The modelling of such a system is not above the authors skill level, however it would require time invested into research. From the aspect of making the deadline of this thesis, the decision has been made to proceed with the PT_1 approximation of the inverter control system dynamics.

With this being clarified, the following chapter returns to the decomposition of the stator voltage differential equation *(4.85)* into its d and q components in order to control rotor flux and machine torque separately.

4.3.4. Decomposition of the BSG stator voltage model into its d and q components

Firstly, the rotor current can be expressed from *(4.89)*:

$$\bar{\imath}_r = \frac{1}{L_r}\bar{\psi}_r - \frac{L_m}{L_r}\bar{\imath}_s \,, \tag{4.92}$$

noting that the index *k* has been omitted in the favor of simplicity of expressions. This notation for the model of an induction machine referred to the rotating coordinate system without index *k* will be used from this point on. When *(4.92)* is introduced into the stator flux equation *(4.88)* the following is obtained:

$$\bar{\psi}_s = L_s\bar{\imath}_s + L_m\bar{\imath}_r = L_s\bar{\imath}_s + \left(\frac{L_m}{L_r}\bar{\psi}_r - \frac{L_m^2}{L_r}\bar{\imath}_s\right). \tag{4.93}$$

By utilizing on *(4.93)* the stator voltage $\bar{u}_s$ is obtained as a function of stator current $\bar{\imath}_s$ and rotor flux $\bar{\psi}_r$:

$$\bar{u}_s = \bar{\imath}_s R_s + \frac{d\bar{\psi}_s}{dt} + j\bar{\psi}_s\omega_k \,, \tag{4.94}$$

$$\bar{u}_s = \bar{\imath}_s R_s + \frac{d}{dt}\left[L_s\bar{\imath}_s + \left(\frac{L_m}{L_r}\bar{\psi}_r - \frac{L_m^2}{L_r}\bar{\imath}_s\right)\right] + j\bar{\psi}_s\omega_{mr}\left(L_s\bar{\imath}_s + \left(\frac{L_m}{L_r}\bar{\psi}_r - \frac{L_m^2}{L_r}\bar{\imath}_s\right)\right), \tag{4.95}$$

$$\bar{u}_s = \bar{\imath}_s R_s + \left(L_s\left(1 - \frac{L_m^2}{L_r L_s}\right)\frac{d}{dt}\bar{\imath}_s + \frac{L_m^2}{L_r}\frac{d}{dt}i_{mr}\right) + j\omega_{mr}\left(L_s\left(1 - \frac{L_m^2}{L_r L_s}\right)\bar{\imath}_s + \left(\frac{L_m^2}{L_r}i_{mr}\right)\right), \tag{4.96}$$

where the induction leakage coefficient is defined by

$$\sigma = 1 - \frac{L_m^2}{L_r L_s}. \tag{4.97}$$

The term $\frac{d}{dt} i_{mr}$ from *(4.96)* is an unknown, however it can be obtained by knowing the information about the stator filed current i_{sd}. The stator field current can be derived from the rotor voltage equation (4.86), minding that $\bar{\psi}_r = \psi_{rd}$ due to the rotor flux space vector being collinear with the d axis:

$$0 = \frac{R_r}{L_r}\psi_{rd} + \frac{R_r L_m}{L_r}\bar{\imath}_s + \frac{d\psi_{rd}}{dt} + j\psi_{rd}(\omega_{mr} - \omega)\ , \qquad (4.98)$$

and after decomposing the stator current space vector $\bar{\imath}_s$ in its real d and imaginary q components,

$$0 = \frac{R_r}{L_r}\psi_{rd} + \frac{R_r L_m}{L_r}\left(i_{sd} + j i_{sq}\right) + \frac{d\psi_{rd}}{dt} + j\psi_{rd}(\omega_{mr} - \omega), \qquad (4.99)$$

where the rotor time constant is defined as

$$T_r = \frac{L_r}{R_r}. \qquad (4.100)$$

By applying *(4.100)* on *(4.99)* along with

$$\psi_{rd} = L_m i_{mr}\ , \qquad (4.101)$$

which stems from *(4.66)*, the following equation is obtained

$$0 = \frac{L_m}{T_r} i_{mr} + \frac{L_m}{T_r}\left(i_{sd} + j i_{sq}\right) + L_m \frac{d i_{mr}}{dt} + j L_m i_{mr}(\omega_k - \omega)\ . \qquad (4.102)$$

After separating *(4.102)* on its real and imaginary parts, the expression for $\frac{d}{dt} i_{mr}$ is found.

Real:

$$0 = \frac{L_m}{T_r} i_{mr} - \frac{L_m}{T_r} i_{sd} + L_m \frac{d i_{mr}}{dt} \,/\cdot \frac{T_r}{L_m} \qquad (4.103)$$

$$\frac{d i_{mr}}{dt} = -\frac{1}{T_r} i_{mr} + i_{sd} \qquad (4.104)$$

Imaginary

$$\frac{L_m}{T_r} i_{sq} = L_m i_{mr}(\omega_k - \omega)\ , \qquad (4.105)$$

$$\omega_{mr} = \omega + \frac{1}{T_r i_{mr}} i_{sq}\ . \qquad (4.106)$$

Finally, by applying *(4.97)* and *(4.104)* on *(4.96)* the stator voltage expression suitable for vector control is obtained:

$$\bar{u}_s = \bar{\imath}_s R_s + \left(L_s \sigma \frac{d}{dt}\bar{\imath}_s + \frac{L_m^2}{L_r}\frac{i_{sd} - i_{mr}}{T_r}\right) + j\omega_{mr}\left(L_s \sigma \bar{\imath}_s + \left(\frac{L_m^2}{L_r} i_{mr}\right)\right). \qquad (4.107)$$

The expression (4.107) can also be separated into its real and imaginary part:

$$\bar{u}_s = u_{sd} + j u_{sq}\ , \qquad (4.108)$$

$$\bar{u}_s = \left(i_{sd} + ji_{sq}\right)R_s + \left(L_s\sigma\frac{d}{dt}\left(i_{sd} + ji_{sq}\right) + \frac{L_m^2}{L_r}\frac{i_{sd}-i_{mr}}{T_r}\right) + j\omega_{mr}\left(L_s\sigma\left(i_{sd} + ji_{sq}\right) + \left(\frac{L_m^2}{L_r}i_{mr}\right)\right). \quad (4.109)$$

Real part of *(4.109)*:

$$u_{sd} = \left(R_s + \frac{L_m^2}{L_r^2}\right)i_{sd} + \sigma L_s\frac{di_{sd}}{dt} - \left(\frac{1}{T_r}\frac{L_m^2}{L_r}i_{mr} + \omega_{mr}\sigma L_s i_{sq}\right). \quad (4.110)$$

Imaginary part of *(4.109)*:

$$u_{sq} = R_s i_{sq} + \sigma L_s\frac{di_{sq}}{dt} + \left(\omega_{mr}\frac{L_m^2}{L_r}i_{mr} + \omega_{mr}\sigma L_s i_{sd}\right). \quad (4.111)$$

The real component of the stator voltage, u_{sd}, will be used to control the rotor magnetic flux and the imaginary part of the stator voltage, u_{sq}, will be used to control the output torque of the machine. However, it can be observed from *(4.110)* and *(4.111)* that the terms contained inside of brackets couple them with one another.

In order to independently control rotor flux and machine torque, these equations need to be decoupled. Favorable for us, they are expressed in a form that makes the decoupling procedure possible, which was the goal of chapter 4. The decoupling procedure consists of correctly estimating the decoupling signals defined as:

$$\Delta u_{sd} = \frac{1}{T_r}\frac{L_m^2}{L_r}i_{mr} + \omega_{mr}\sigma L_s i_{sq}\,, \quad (4.112)$$

$$\Delta u_{sq} = -\left(\omega_{mr}\frac{L_m^2}{L_r}i_{mr} + \omega_{mr}\sigma L_s i_{sd}\right). \quad (4.113)$$

Expressions *(4.110) – (4.113)* enable the separate control of induction motor torque and rotor magnetic flux, which is analogous to the case of the DC machine. This allows the implementation of independently and analytically tuned controllers. For the $d-q$ axes to remain decoupled it is important to accurately estimate the magnetization current i_{mr}, i.e. the rotor flux angle ρ. If this condition is true, then the following expression for the BSG torque applies:

$$m_{BSG} = k_t i_{sq}\psi_r = k_t' i_{sq} i_{sd}. \quad (4.114)$$

To conclude this chapter, mathematical model of the BSG in the form that allows for the independent control of rotor flux and machine torque and facilitates the analytical tuning of the field current i_{sd} and torque current i_{sq} controllers independently of one another is summarized on the following page.

BSG electrical model for independent control of flux and torque:

$$u_{sd} + \Delta u_{sd} = R_d i_{sd} + L_d \frac{di_{sd}}{dt} \quad (4.115)$$

$$u_{sq} + \Delta u_{sq} = R_q i_{sq} + L_q \frac{di_{sq}}{dt} \quad (4.116)$$

$$m_{BSG} = k_t i_{sq} \psi_r = k_t' i_{sq} i_{sd} \quad (4.117)$$

$$\Delta u_{sd} = \frac{1}{T_r} \frac{L_m^2}{L_r} i_{mr} + \omega_{mr} \sigma L_s i_{sq} \quad (4.118)$$

$$\Delta u_{sq} = -\left(\omega_{mr} \frac{L_m^2}{L_r} i_{mr} + \omega_{mr} \sigma L_s i_{sd} \right) \quad (4.119)$$

$$\frac{di_{mr}}{dt} = -\frac{1}{T_r} i_{mr} + i_{sd} \quad (4.120)$$

$$\omega_{mr} = \omega + \frac{1}{T_r i_{mr}} i_{sq} \quad (4.121)$$

$$\omega_{mr} = \frac{d\rho}{dt} \quad (4.122)$$

In the following chapter the model given by *(4.115) – (4.122)* is used to design the control system for the mitigation of FEAD belt vibrations by means of controlling both the speed of the BSG, as well as d and q currents using the cascade control approach. The speed and current control systems will be tuned according to the analytical, pole-placement-like method based on the damping optimum criterion.

5. DESIGN OF THE CONTROL SYSTEM FOR MITIGATION OF FEAD BELT VIBRATIONS

5.1. VSI fed squirrel-cage induction machine control scheme

As mentioned in the previous chapter, a voltage-source inverter is needed to control the flux of the rotor and torque of the BSG. Figure 22 shows the control scheme based on the VSI fed BSG, on which two different control branches can be observed, each with two controllers arranged into a cascade.

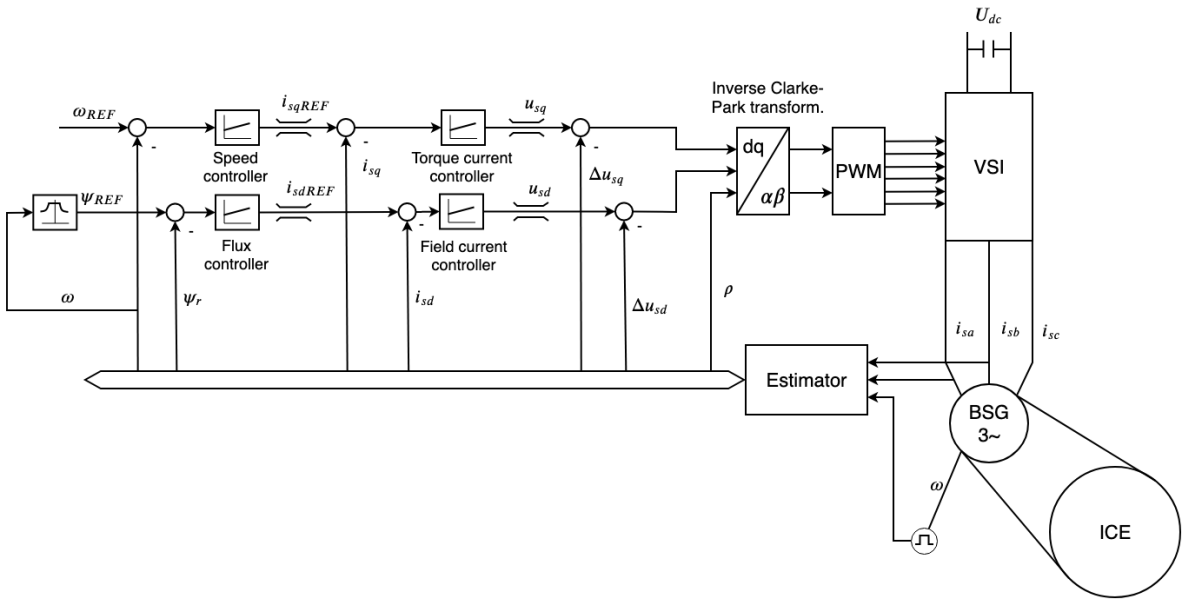


Fig. 22 Control scheme based on VSI fed BSG [15]

The cascade control arrangement is a multi-loop control structure that utilizes on information about the states of the subsystems, unlike single-loop control structures that register only the output of the system. In a single-loop control structure the controller reacts only when the effect of an external disturbance is registered in the output of the system, which results in poor performance compared to cascade control. In cascade control the controllers of the inner loops (subsystems) react before the effect of the disturbance is registered in the output, yielding

better performance in the respect to the compensation of external disturbances [22].
The cascade branch governing the field current i_{sd} will be modified since the following can be assumed:

- The speed of the BSG doesn't exceed the rated value when performing stop/start and boosting function, which is ensured by the automatic transmission.

If this assumption holds, then the magnetic flux of the rotor ψ_r is kept constant and the torque is controlled separately as before via the i_{sq} current. When the induction machine oversteps the nominal (rated) speed, it enters the flux-weakening region of operation [20], which manifests itself in respect to the control system as the reduction of flux controller reference, which can be observed on figure 22. The consequence of this is that the torque current reference i_{sqR} is lowered (e.g. by lowering the current limit of the machine). Consequently, the machine torque is also lowered, so that the machine doesn't overstep the rated power value. For the vehicle, this would mean less torque and therefore slower acceleration at speeds above the nominal value.

Considering the aforementioned assumption of BSG not exceeding rated speed, figure 23 shows the modified cascade control scheme and BSG mathematical model which will be used for simulations in this thesis. It can be observed that the rotor flux controller has been omitted due to the assumption of rated speed not being exceeded.

Before proceeding to the simulation of the system shown on figure 23, the parameters of speed and current PI controllers need to be determined and FEAD needs to be modeled. The synthesis of parameters of all three PI controllers using an analytical method based on damping optimum criterion, which will ensure the mitigation of FEAD belt vibrations, is described in the following chapter.

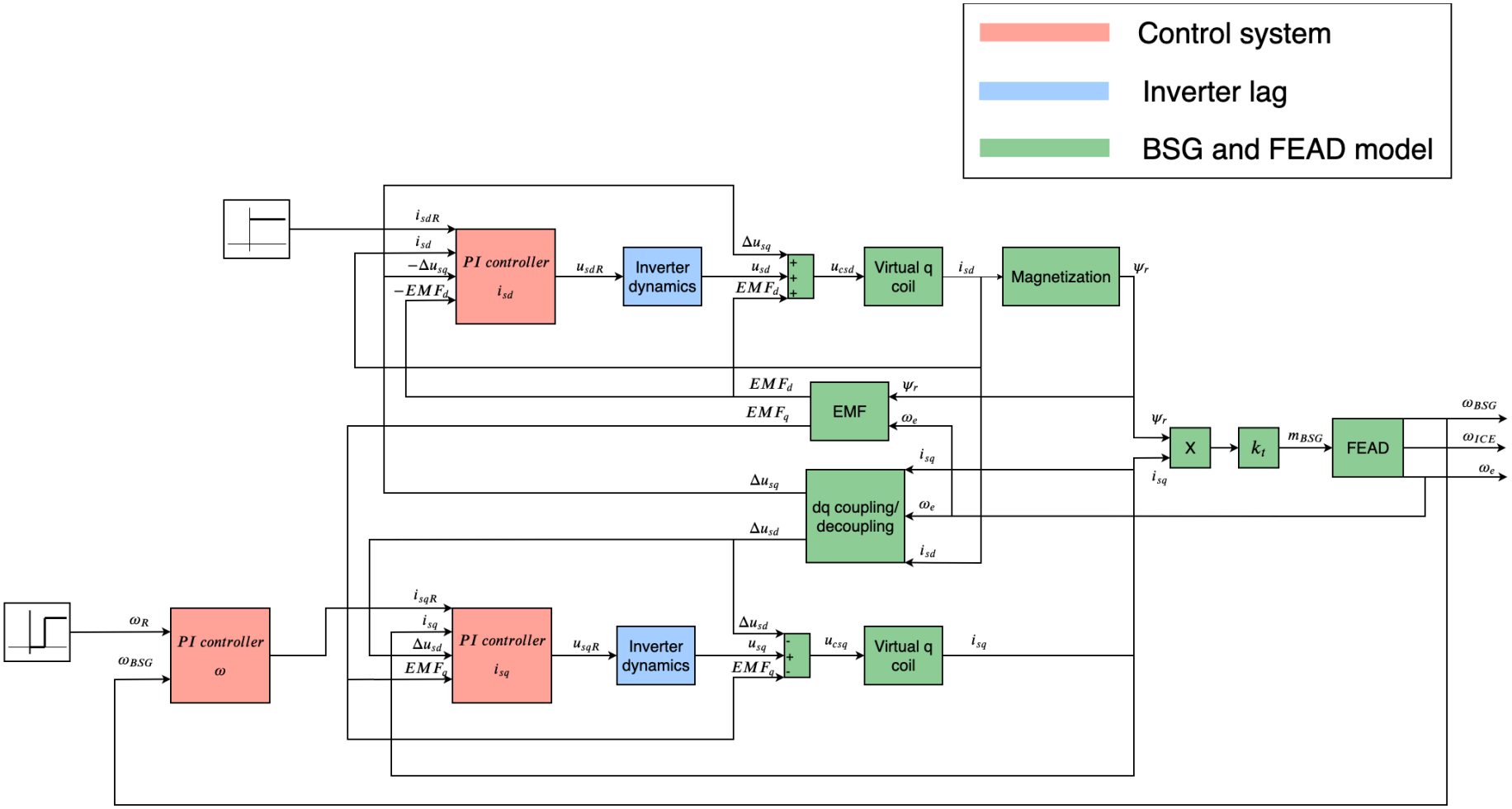


Fig. 23 Scheme of the cascade BSG control structure and its mathematical model in rotating dq coordinate system

5.2. Synthesis of BSG speed and current control system parameters

5.2.1. An introduction to the transfer function concept and pole placement method

The behavior of a continuous linear system is predominantly determined by its characteristic polynomial, i.e. the denominator of its transfer function. The transfer function is obtained by transforming the system model from time domain to *s*-domain by applying the Laplace transform:

$$F(s) = \int_0^\infty f(t)e^{-st}dt \qquad (5.1)$$

and then dividing the input variable with the output variable of the system in *s*-domain

$$G(s) = \frac{x_o(s)}{x_i(s)} \qquad (5.2)$$

Where $G(s)$ is an arbitrary transfer function of a system with an input variable $x_i(s)$ and an output variable $x_o(s)$. Systems with only one input and only one output are called SISO (single input single output) systems and can be described in the s-domain by a single transfer function $G(s)$. The virtual d and q coils from figure 23, which are essentially Krichoff's voltage law in *s*-domain, are SISO since those currents are controlled only by their respective voltages u_{csd} and u_{csq}, which is illustrated on figure 24.

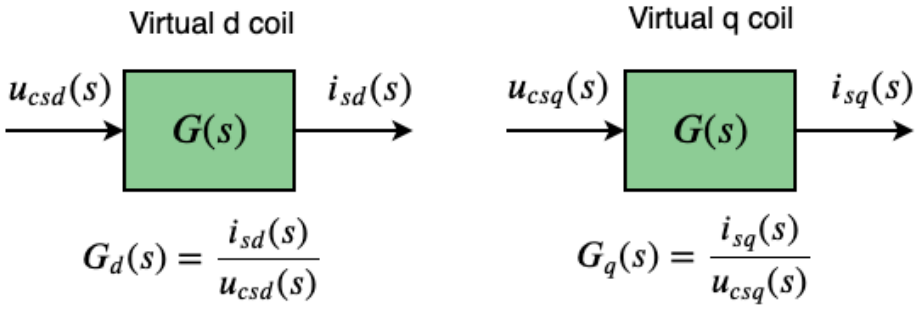


Fig. 24 Virtual d and q coils represented by their respective transfer functions

The system comprised of BSG torque equation coupled with FEAD dynamics is also SISO since the speed is controlled only by the torque current i_{sq}, due to the rotor flux ψ_r being kept constant because of the assumption made in chapter 5.1. This representation of BSG torque and FEAD dynamics is shown of figure 25.

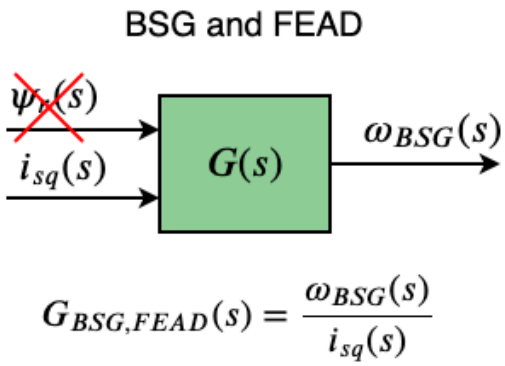


Fig. 25 BSG torque and FEAD dynamics represented by a tranfer function $G_{BSG,FEAD}(s)$

An arbitrary transfer function of the system of the n-th order has the following form

$$G(s) = \frac{x_o(s)}{x_i(s)} = \frac{B(s)}{N(s)} = \frac{b_m s^m + b_{m-1}s^{m-1} + b_{m-2}s^{m-2} + \cdots + b_1 s + b_0}{a_n s^n + a_{n-1}s^{n-1} + a_{n-2}s^{n-2} + \cdots + a_1 s + a_0} \quad (5.3)$$

The numerator $B(s)$ describes the dynamics of the system input $x_i(s)$, while the denominator $N(s)$ that of the output $x_o(s)$. The coefficients a_i and b_i are determined by parameters of the system. Every denominator $N(s)$ of an arbitrary transfer function is called the characteristic polynomial:

$$N(s) = a_n s^n + a_{n-1}s^{n-1} + a_{n-2}s^{n-2} + \cdots + a_1 s + a_0 \,. \quad (5.4)$$

When the characteristic polynomial is equated to 0 the characteristic equation of the system is obtained:

$$a_n s^n + a_{n-1}s^{n-1} + a_{n-2}s^{n-2} + \cdots + a_1 s + a_0 = 0 \,, \quad (5.5)$$

and after solving the characteristic equation the poles of the system are obtained:

$$s_i = \sigma_i + j\omega_i. \quad (5.6)$$

The poles of the system can be real or complex, and if the system is of the second order, its poles are directly tied to its damping and stability [22]. So, in order to get a second order system to behave in a satisfying manner, its poles need to be placed on certain positions in the complex s-plane by introducing the controller into the system and tuning its parameters. In order to get an optimally damped system, its poles need to be placed on the line of optimal damping, defined by the coefficient of relative damping $\zeta = \frac{\sqrt{2}}{2}$. The word optimal is used here in respect to the compromise between system response speed and vibrations damping, since one cannot have both. The s-plane, along with its regions and line of optimal damping is shown on figure 26.

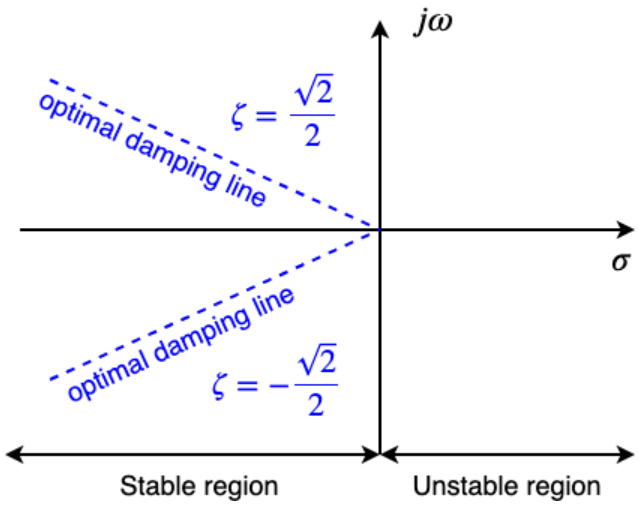


Fig. 26 s-plane with the optimal damping line defined by the coefficient of relative damping $\zeta = \frac{\sqrt{2}}{2}$

As mentioned, the coupling between the system poles and parameters indicating the behavior of the transient response, the relative damping factor ζ and the natural frequency ω_n, is only valid for the systems of the second order. This can be observed by looking at the characteristic polynomial of the general transfer function $G_2(s)$ for an arbitrary second order system:

$$G(s) = \frac{1}{\frac{1}{\omega_n^2}s^2 + \frac{2\zeta}{\omega_n s} + 1} \qquad (5.7)$$

The idea of the damping optimum criterion is to couple the poles of higher order systems with ζ and ω_0 [22], which is necessary to optimally tune BSG speed controller, since the speed control system is of fifth order.

5.2.2. Damping optimum criterion

In order to derive the damping optimum criterion, the transfer function of a linear system of n-th order will be used

$$G(s) = \frac{y(s)}{y_R(s)} = \frac{1}{a_n s^n + a_{n-1}s^{n-1} + a_{n-2}s^{n-2} + \cdots + a_1 s + a_0} \qquad (5.8)$$

which can be represented by an equivalent block diagram shown on figure 27.

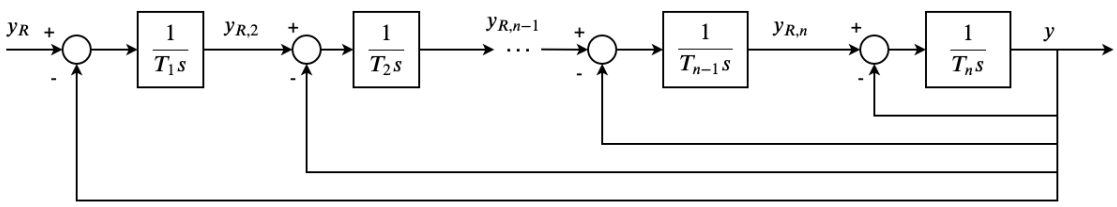


Fig. 27 Block diagram of a linear system described by transfer function (5.8)

The coupling of the poles of *(5.8)*, that is, the coefficients a_i with the time constants T_i from figure 27, requires that the transfer function of the block diagram from the same figure is derived. Transfer function $G_c(s)$ of an arbitrary closed loop shown on figure 28 is obtained by using the expression *(5.9)*

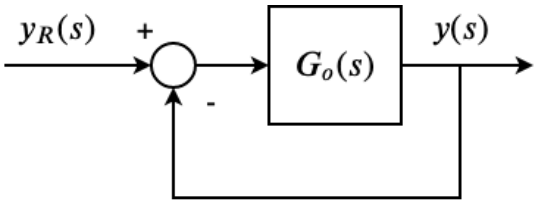


Fig. 28 Arbitrary closed loop

$$G_c(s) = \frac{y(s)}{y_R(s)} = \frac{G_o(s)}{1 + G_o(s)}, \tag{5.9}$$

where $G_o(s)$ is the open loop transfer function. Starting from the innermost loop and using the expression *(5.9)*, the transfer functions are as follows:

$$G_n(s) = \frac{y(s)}{y_{R,n}(s)} = \frac{1}{T_n s + 1}, \tag{5.10}$$

$$G_{n-1}(s) = \frac{y_{R,n}(s)}{y_{R-1}(s)} = \frac{1}{T_{n-1}T_n s^2 + T_{n-1}s + 1}, \tag{5.11}$$

$$G_{n-2}(s) = \frac{y_{R-1}(s)}{y_{R-2}(s)} = \frac{1}{T_{n-2}T_{n-1}T_n s^3 + T_{n-2}T_{n-1}s^2 + T_{n-2}s + 1}, \tag{5.12}$$

…

Stemming from this, the transfer function of the block diagram on figure 27 is obtained:

$$G(s) = \frac{y(s)}{y_R(s)} = \frac{1}{1 + \sum_{i=1}^{n}\prod_{j=1}^{i} T_j s^i}. \tag{5.13}$$

It is now evident that the coefficients a_i of the transfer function *(5.8)* are coupled to the time constants T_i, i.e. the coefficients of transfer function *(5.13)* in the following manner:

$$a_n = T_n T_{n-1} \dots T_1, \tag{5.14}$$

$$a_{n-1} = T_{n-1} T_{n-2} \dots T_1, \tag{5.15}$$

…

$$a_1 = T_1, \tag{5.16}$$

$$a_0 = 1, \tag{5.17}$$

or

$$T_i = \frac{a_i}{a_{i-1}}. \qquad (5.18)$$

The next step is to couple the time constants *(5.18)* to the parameters indicating the transient response behavior, i.e. the relative damping factor ζ and the natural frequency ω_n. This is done by considering the following subloop from figure 27 separately.

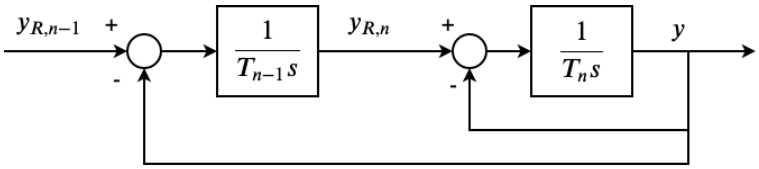


Fig. 29 Subloop from figure 27

The subloop from figure 29 can be transformed into the loop shown on figure 30,

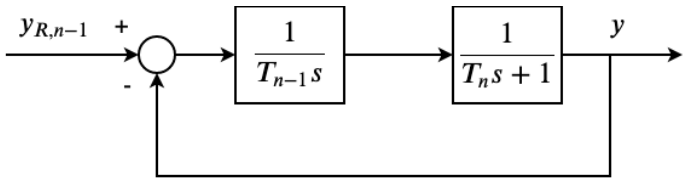


Fig. 30 Transformed subloop from figure 27

and its transfer function is:

$$G_{n-1}(s) = \frac{1}{\underbrace{T_{n-1}T_n s^2}_{\frac{1}{\omega_n^2}} + \underbrace{T_{n-1}s}_{\frac{2\zeta}{\omega_n s}} + 1}. \qquad (5.19)$$

The relationship between the coefficient of relative damping ζ and the time constants T_i now becomes clear:

$$\frac{T_n}{T_{n-1}} = \frac{1}{4\zeta^2}. \qquad (5.20)$$

Expression (5.20) indicates that the relative damping coefficient is determined by the ratio of time constants T_n and T_{n-1}. This ratio is called characteristic ratio D_n:

$$D_n = \frac{T_n}{T_{n-1}}. \qquad (5.21)$$

Every system with a relative damping coefficient $\zeta = \frac{\sqrt{2}}{2}$ results in a quasi-aperiodic response with 6% overshoot and rise time between 1.8-2.1 T_e, where T_e is the equivalent time constant of that system [23]. In order to get $\zeta = \frac{\sqrt{2}}{2}$ the characteristic ratio D_n needs to be:

$$D_n = \frac{T_n}{T_{n-1}} = \frac{1}{4\zeta^2} = 0.5 \qquad (5.22)$$

Considering that the time response of a system with $\zeta = \frac{\sqrt{2}}{2}$ from figure 29, i.e. figure 30, has an overshoot of only 6%, it can be approximated by the PT_1 term:

$$G_{n-1}(s) = \frac{1}{T_{n-1}T_n s^2 + T_{n-1}s + 1} \approx \frac{1}{T_{n-1}s + 1}. \quad (5.23)$$

The ability to make this approximation is significant from the aspect of control system tuning since it lowers the order of the system by one, meaning that one less free parameter (controller parameter) is needed to place the poles of the system on the line of optimal damping from figure 26. To put it precisely, simpler controllers can be used and one less system variable (displacement, speed, acceleration, voltage, current…) needs to be measured/estimated.

The procedure *(5.19)* - *(5.23)* can be repeated for every preceding subloop of the cascade structure from figure 27 and if every characteristic ratio is set to $D_i = 0.5$ then the damping optimum is achieved. In that case, every subloop in an arbitrary cascade structure has the relative damping factor $\zeta_i = \frac{\sqrt{2}}{2}$ and can be approximated by *(5.23)*.

Considering that every subloop of the cascade structure from figure 27 is of second order and considering that the poles of these second-order subloops have been by means of $D_i = 0.5$ placed on the line of optimal damping $\zeta_i = \frac{\sqrt{2}}{2}$, it can be said that the relationship between the system pole locations in the *s*-plane to its damping and stability has been generalized in respect to systems of higher order, which concludes the derivation of the damping optimum criterion. The value of characteristic ratios on the response of the system defined by the damping optimum characteristic polynomial of 5-th order can be seen of figure 31.

$$G(s) = \frac{1}{D_5 D_4^2 D_3^3 D_2^4 T_e^5 s^5 + D_4 D_3^2 D_2^3 T_e^4 s^4 + D_3 D_2^2 T_e^3 s^3 + D_2 T_e^2 s^2 + T_e s + 1} \quad (5.24)$$

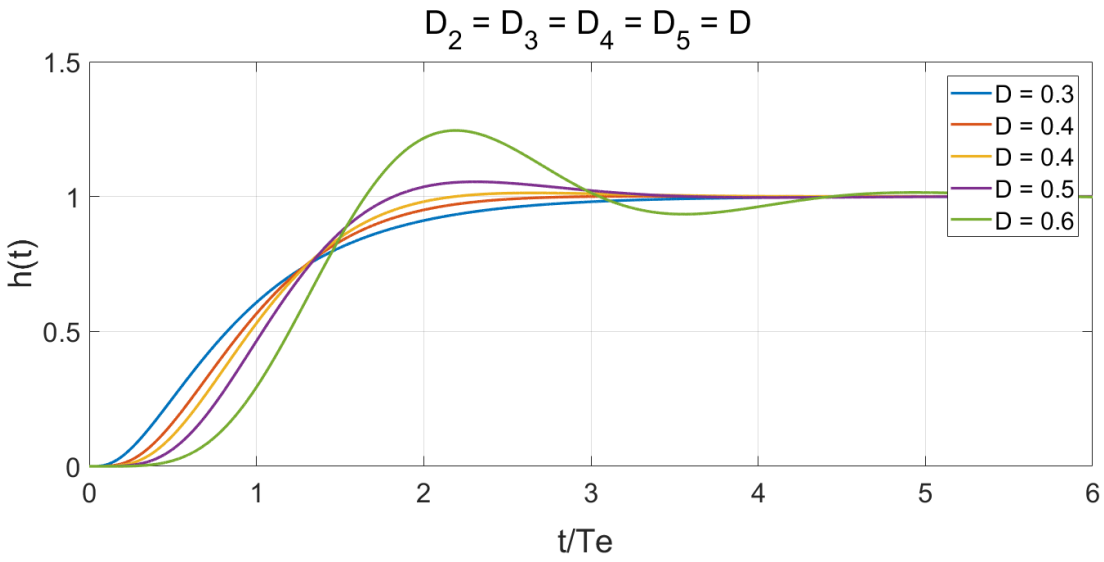


Fig. 31 Influence of different values of characteristic ratios D_i to the response of a system with the damping optimum characterstic polynomial

In the following chapters, the parameters of BSG field and torque current PI controllers, as well as of its speed PI controller, are determined analytically using the damping optimum criterion presented in this chapter.

5.2.3. Synthesis of BSG dq currents control system parameters

Since the torque of the BSG is controlled via the torque current i_{sq}, with the field current i_{sd} being kept constant, only the parameters of the i_{sq} PI controller will be determined using the damping optimum criterion and then those same parameters will be set as the parameters of the i_{sd} controller. The i_{sq} current control loop of the BSG is represented by the scheme on figure 32.

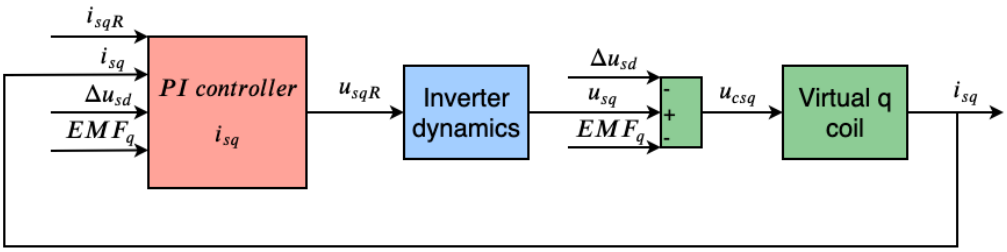


Fig. 32 BSG current contol loop scheme

Since the EMF and $d-q$ axes coupling are compensated for, as shown in figure 32, the following block diagram can be used to synthesize the controller parameters K_{ci} and T_{ci}.

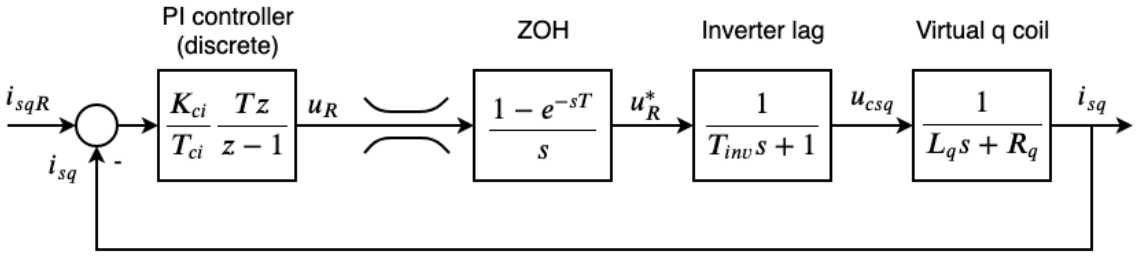


Fig. 33 Current control subloop block diagram

From figure 33 can be observed that the i_{sq} PI controller is discrete, hence the quasi-continuous approach is utilized to determine its parameters. Quasi-continuous approach lumps together the extrapolation delay and fast inverter dynamics to approximate them with the PT_1 term defined by the parasitic time constant $T_{\Sigma i}$ [23]. This enables the synthesis to be carried out using the continuous model of PI controller, as seen on figure 34.

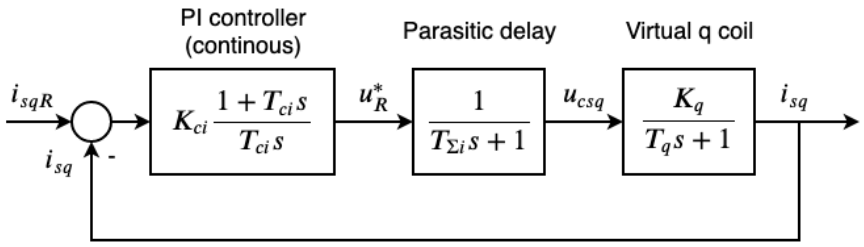


Fig. 34 Current control loop for quasi-continuous approach to controller parameter synthesis

The parasitic time constant $T_{\Sigma i}$ is defined by:

$$T_{\Sigma i} = \frac{T}{2} + T_{inv}. \tag{5.25}$$

In order to achieve a fast response of i_{sq} following the change of reference i_{sqR}, the controller time constant T_{ci} used to cancel out the dominant time constant of the system from figure 34, that is the virtual coil time constant T_q.

$$T_{ci} = T_q. \tag{5.26}$$

The closed loop transfer function of the current control subsystem can now be obtained:

$$G_{ci}(s) = \frac{1}{\frac{T_{ci}T_{\Sigma i}}{K_{ci}K_q}s^2 + \frac{T_{ci}}{K_{ci}K_q}s + 1}. \tag{5.27}$$

The controller parameters are synthesized by using the damping optimum criterion discussed in chapter 5.2.2. The characteristic polynomial of the transfer function (5.27) is equated with the second-order damping optimum characteristic polynomial with all characteristic ratios set to $D_i = 0.5$. The second-order damping optimum characteristic polynomial has the following form,

$$A_{ODO}(s) = D_2 T_{ei}^2 s^2 + T_e s + 1, \tag{5.28}$$

and after equating

$$\frac{T_{ci}T_{\Sigma i}}{K_{ci}K_q}s^2 + \frac{T_{ci}}{K_{ci}K_q}s + 1 = D_2 T_{ei}^2 s^2 + T_e s + 1, \tag{5.29}$$

the following expressions for i_{sq} PI controller parameters and current control system equivalent time constant are T_{ei}obtained,

$$T_{ei} = 2T_{\Sigma i}, \tag{5.30}$$

$$T_{ci} = T_q, \tag{5.31}$$

$$K_{ci} = \frac{T_{ci}}{T_{ei}K_q} = \frac{T_{ci}}{2T_{\Sigma i}K_q}, \tag{5.32}$$

The response of the current control system with parameters *(5.30)* - *(5.32)* can be observed in figure 35. The response on the step change of i_{sqR} is shown firstly, and then on an "arbitrary" change of i_{sqR} conditioned by the preceding control loop in the cascade structure.

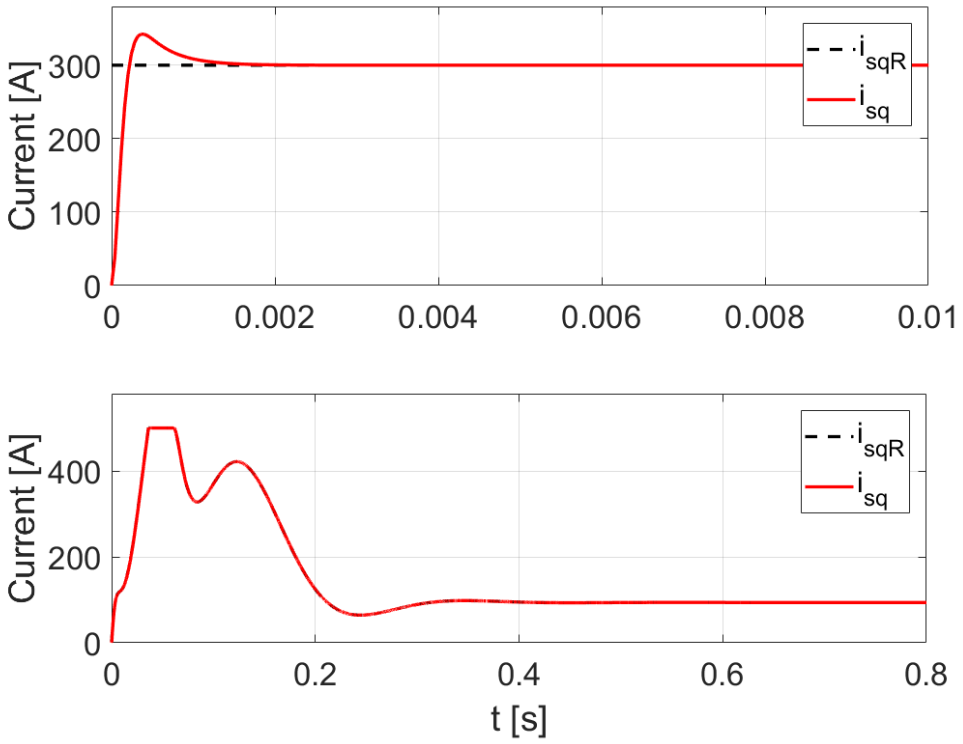


Fig. 35 Response of the torque current control system tuned according to damping optimum

The tuning of the current control system according to damping optimum criterion allows for it, as said in chapter 5.2.2., to be approximated with the PT_1 term defined defined by the current control loop equivalent time constant:

$$G_{ci}(s) = \frac{1}{T_{ei}s + 1}. \qquad (5.33)$$

This approximation will be used in the synthesis of BSG speed PI controller parameters, since it lowers the system order by one. Before proceeding to BSG speed control system tuning, the accessory drive model two-mass simplification needs to be clarified since it has a meaningful impact on speed control.

5.2.4. FEAD MATLAB model

The accessory drive is modelled as two masses, BSG and ICE crankshaft, coupled with a spring and a damper as shown on figure 36. Such model represents an approximation of the accessory drive in which the spring/damper joint, defined by its longitudinal stiffness k_L and longitudinal damping d_L, is supposed to approximate the elastic behavior of the timing belt.

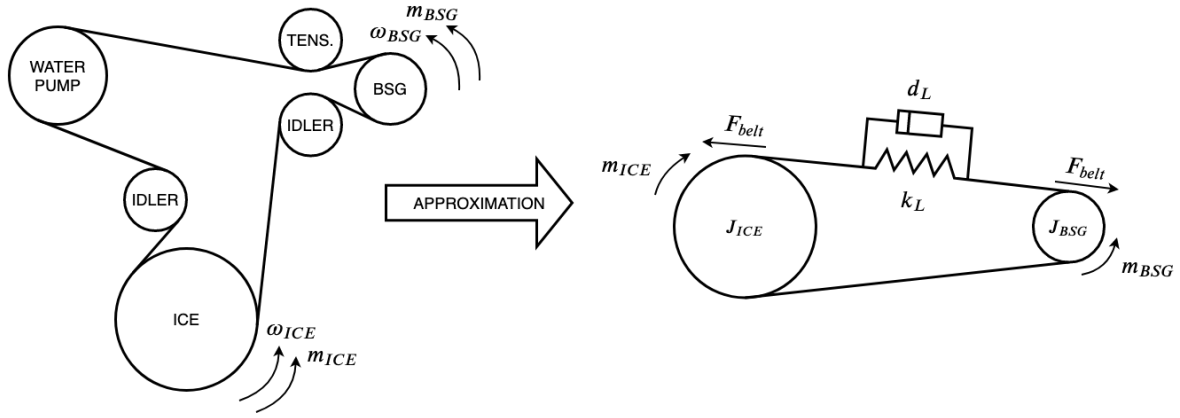


Fig. 36 Two-mass approximation of FEAD

The equations describing the rotational dynamics of accessory drive modeled as a two-mass elastic system, with the longitudinal model of belt dynamics from figure 36, are as follows:

$$J_{BSG}\frac{d\omega_{BSG}}{dt} = m_{BSG} - F_{belt}r_{BSG} \tag{5.34}$$

$$F_{belt} = k_L(x_{BSG} - x_{ICE}) + d_L(v_{BSG} - v_{ICE}), \tag{5.35}$$

$$J_{ICE}\frac{d\omega_{ICE}}{dt} = F_{belt}r_{ICE} - m_{ICE}, \tag{5.36}$$

where v_{BSG} and v_{ICE} are tangential velocities of BSG and ICE, which are both considered to be rigid bodies, measured relatively to the center of their rotation. Similarly, x_{BSG} and x_{ICE} are their tangential displacements. However, the BSG speed control system parameter synthesis procedure described in [24] considers the torsional coupling between the two inertia (in this case J_{BSG} and J_{ICE}), so the longitudinal model of the belt dynamics has to be transformed into its torsional equivalent as shown on figure 37.

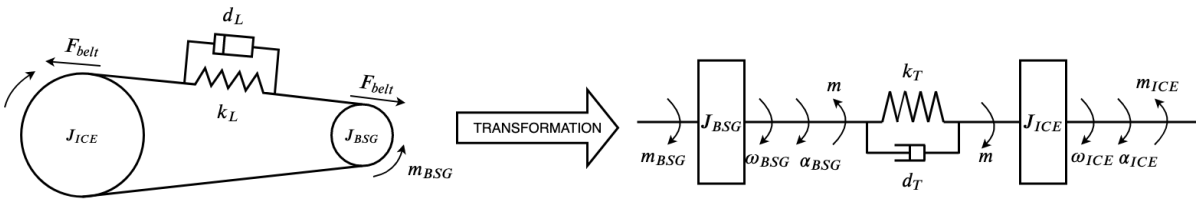


Fig. 37 Scheme of the FEAD model with the longitudinal dynamics of the timing belt and its torsional equivalent

The torsional dynamics of te belt is described by the following set of equations:

$$J_{BSG}\frac{d\omega_{BSG}}{dt} = m_{BSG} - \frac{m}{i_{belt}}, \quad (5.37)$$

$$m = k_T(\alpha_{BSG} - \alpha_{ICE}) + d_T\left(\frac{\omega_{BSG}}{i_{belt}} - \omega_{ICE}\right), \quad (5.38)$$

$$J_{ICE}\frac{d\omega_{ICE}}{dt} = m - m_t. \quad (5.39)$$

Figure 37 implies that the longitudinal stiffness k_L and damping k_L of the belt have to be transformed into their torsional equivalents k_T and d_T. This shall be done by observing the belt force F_{belt} on the ICE crankshaft pulley and multiplying it by the radius of the crankshaft r_{ICE} in order to obtain the torque driving the crankshaft, and then equating it torque to *(5.38)*. The contact between the belt and the pulley is not considered here. With this in mind, the following expression is obtained,

$$k_L(x_{BSG} - x_{ICE})r_{ICE} + d_L(v_{BSG} - v_{ICE})r_{ICE} = k_T(\alpha_{BSG} - \alpha_{ICE}) + d_T\left(\frac{\omega_{BSG}}{i_{belt}} - \omega_{ICE}\right), \quad (5.40)$$

from which stems the expression for equivalent torsional stiffness k_T,

$$k_T = k_L\frac{x_{BSG} - x_{ICE}}{\alpha_{BSG} - \alpha_{ICE}} = k_L\frac{\Delta x}{\Delta\alpha}r_{ICE}, \quad (5.41)$$

where

$$\frac{\Delta x}{\Delta\alpha} \approx r_{ICE}. \quad (5.42)$$

This yields:

$$k_T \approx k_L r_{ICE}^2. \quad (5.43)$$

The same is repeated for equivalent torsional damping d_T,

$$d_T = d_L\frac{v_{BSG} - v_{ICE}}{\omega_{BSG} - \omega_{ICE}} = d_L\frac{\frac{x_{BSG}}{t} - \frac{x_{ICE}}{t}}{\frac{\alpha_{BSG}}{t} - \frac{\alpha_{ICE}}{t}}r_{ICE} = d_L\frac{x_{BSG} - x_{ICE}}{\alpha_{BSG} - \alpha_{ICE}}r_{ICE} \approx d_L r_{ICE}^2, \quad (5.44)$$

The validity of approximation (5.42) will be shown by comparing the behavior of the control system (with parameters obtained through this approximation) when coupled with the FEAD model which includes longitudinal dynamics of the belt *(5.34) – (5.36)*, opposed to the FEAD model which includes the torsional dynamics of the belt *(5.37) – (5.39)*. These two models are show by block diagrams on figures 38 and 39 respectively.

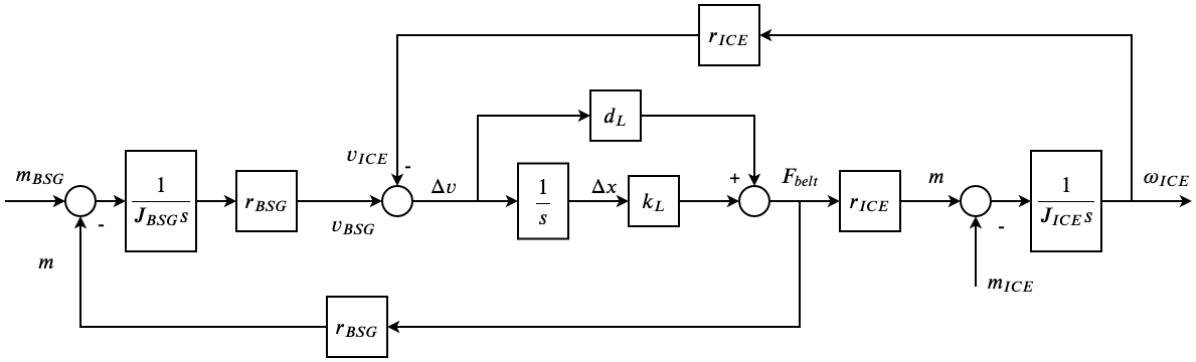


Fig. 38 FEAD block diagram with longitudinal belt dynamics

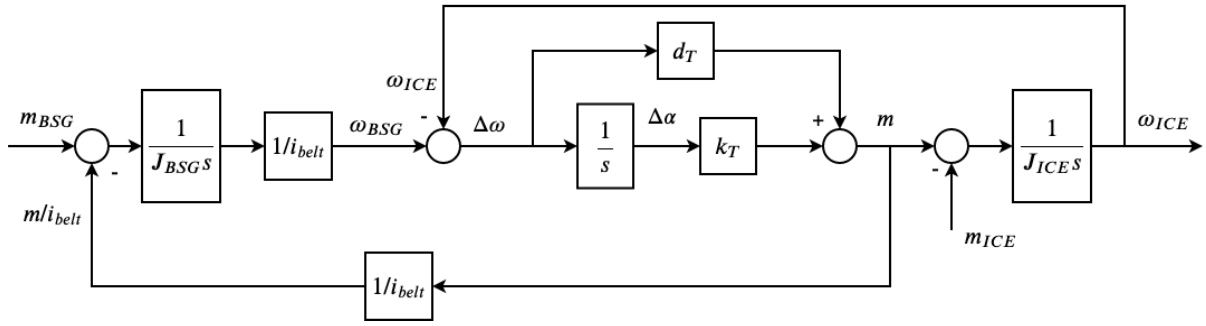


Fig. 39 FEAD block diagram with torsional belt dynamics

The FEAD with the torsional model of the belt dynamics from figure 39 will be used to synthesize the parameters of the BSG speed controller, which is superimposed with respect to the previously discussed PI torque current controller in the cascade control structure.

5.2.5. Synthesis of BSG speed control system parameters

The control system aimed at mitigation of accessory belt vibrations is a cascade structure comprised of BSG speed ω_{ISG} control loop superimposed to the torque current i_{sq} control loop, since the speed of the BSG is controlled by manipulating its torque. If the assumption of BSG not overstepping the rated speed made in chapter 5.1. were not valid, the belt vibrations control system would be comprised of a double cascade structure, in which there would be an additional rotor flux ψ_r controller superimposed to the field current controller, as can be observed from figure 22. The scheme of BSG speed cascade control structure for accessory drive vibrations damping is presented on figure 40, with the current control loop dynamics represented by a single block.

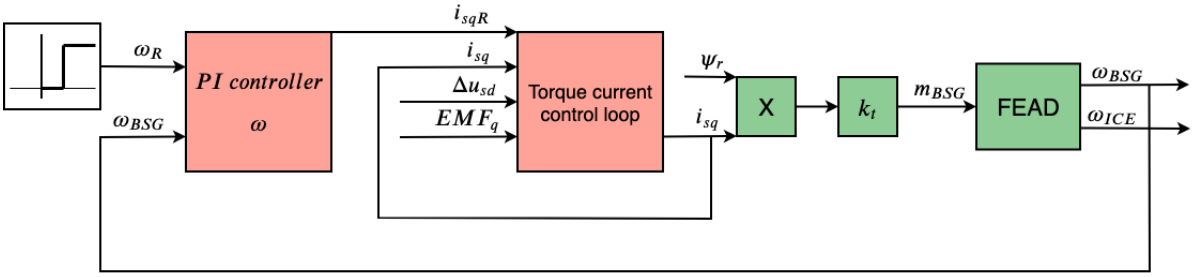


Fig. 40 Scheme of the vibrations damping cascade structure

The following block diagram can be used to synthesize the parameters of BSG speed controller. Due to simplicity, the damping factor d_T is not considered in this procedure [24].

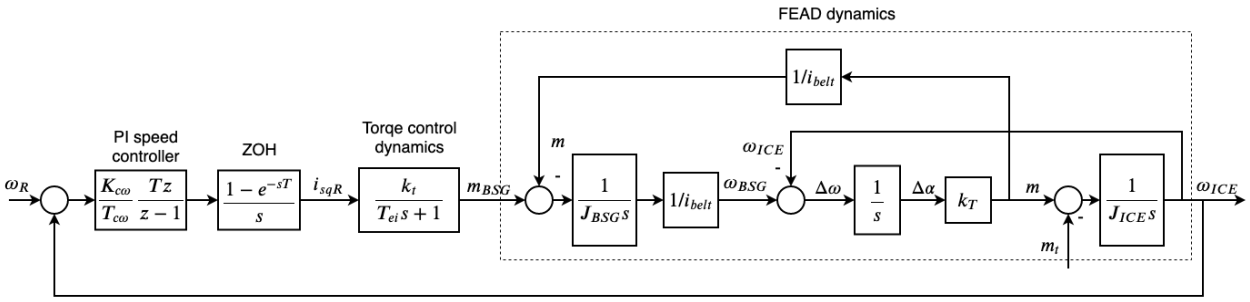


Fig. 41 BSG speed control loop with discrete speed controller

The quasi-continuous approach to controller parameter synthesis is again utilized because of the discrete nature of the speed controller. Also, the current control dynamics is lumped into the parasitic PT_1 term defined by its time constant $T_{\Sigma\omega}$, approximating the effects of discretization and current control dynamics. The BSG speed control loop with these modifications is shown on figure 42.

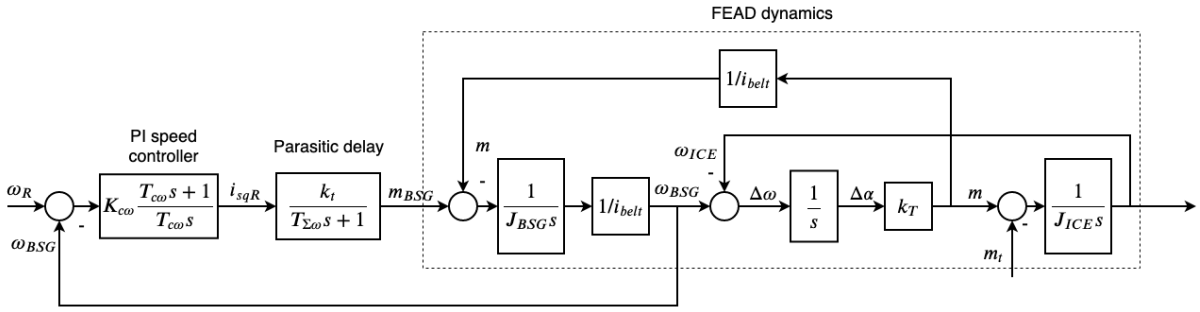


Fig. 42 BSG speed control loop with continuous speed controller

The parasitic time constant $T_{\Sigma\omega}$ is defined by:

$$T_{\Sigma\omega} = \frac{T}{2} + T_{ei}. \tag{5.45}$$

The natural frequencies of the system from figure 40 read:

$$\Omega_0 = \sqrt{k_T\left(\frac{1}{J_{BSG}} + \frac{1}{J_{ICE}}\right)}. \tag{5.46}$$

$$\Omega_{01} = \sqrt{\frac{k_T}{J_{BSG}\, i_{belt}^2}}, \tag{5.47}$$

$$\Omega_{02} = \sqrt{\frac{k_T}{J_{ICE}}}, \tag{5.48}$$

where Ω_0 is the natural frequency of the accessory drive, Ω_{01} the natural frequency of BSG side vibrations and Ω_{02} the natural frequency of ICE side vibrations [24]. The parameter k_T is the equivalent torsional stiffness of the timing belt, J_{BSG} and J_{ICE} the inertiae of BSG rotor and ICE crankshaft respectively. Before expressing the transfer function of BSG speed control loop from figure 42, it is transformed by utilizing on *(5.40)*. The transformed block diagram is presented on figure 43.

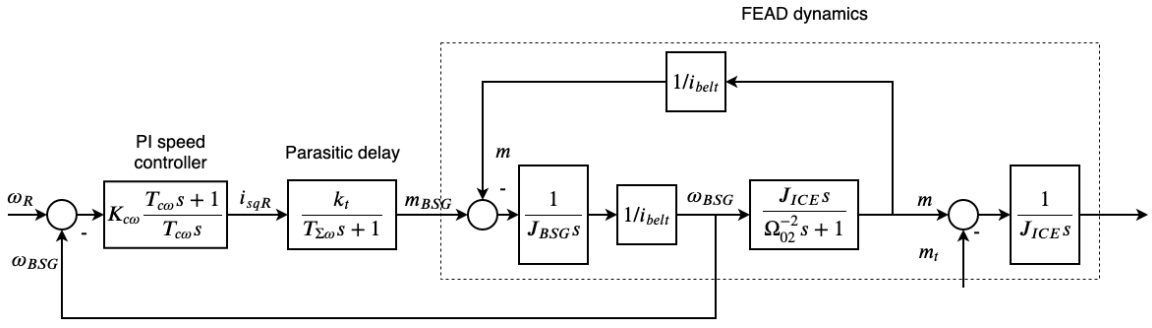


Fig. 43 BSG speed control loop with continuous speed controler favorable for transfer function derivation

The closed loop transfer function of the block diagram from figure 41 reads:

$$G_c(s) = \frac{1}{a_{c5}s^5 + a_{c4}s^4 + a_{c3}s^3 + a_{c2}s^2 + a_{c1}s + 1} \quad (5.49)$$

$$a_{c1} = T_{c\omega}s \quad (5.50)$$

$$a_{c2} = \frac{T_{c\omega}(J_{BSG} + J_{ICE}/i_{belt}^2)}{K_{c\omega}k_t} + \Omega_{02}^{-2}, \quad (5.51)$$

$$a_{c3} = T_{c\omega}\left[\frac{T_{\Sigma\omega}(J_{BSG} + J_{ICE}/i_{belt}^2)}{K_{c\omega}k_t} + \Omega_{02}^{-2}\right], \quad (5.52)$$

$$a_{c4} = \frac{T_{c\omega}J_{BSG}}{K_{c\omega}k_t\Omega_{02}^2}, \quad (5.53)$$

$$a_{c5} = \frac{T_{c\omega}T_{\Sigma\omega}J_{BSG}}{K_{c\omega}k_t\Omega_{02}^2}. \quad (5.54)$$

The controller parameters $K_{c\omega}$ and $T_{c\omega}$ are synthesized by using the damping optimum criterion discussed in chapter 5.2.2. However, this time the system order is greater than the number of free parameters available ($K_{c\omega}$ and $T_{c\omega}$) for placing the system poles on the line of optimum damping $\zeta = \frac{\sqrt{2}}{2}$, i.e. the BSG speed controller is of reduced order [22].

In this case, the best approach is to use the available controller parameters to set the characteristic ratios D_i of the outermost loops of the cascade structure to values of $D_i = 0.5$, that is characteristic ratios $D_2, D_3 \ldots D_{l+1}$, where l is the number of the available controller parameters. This approach results in the dominant poles being placed on the line of optimal damping, owning to the dominant characteristic ratios being $D_i = 0.5$, while the locations of non-dominant poles are determined by the values of non-dominant characteristic ratios which appropriate some values depending on the structure of the process and the controller [22].

So, the characteristic damping optimum polynomial of the fifth order is equated with the characteristic polynomial of the transfer function *(5.41)*.

$$D_5D_4^2D_3^3D_2^4T_{e\omega}^5s^5 + D_4D_3^2D_2^3T_{e\omega}^4s^4 + D_3D_2^2T_{e\omega}^3s^3 + D_2T_{e\omega}^2s^2 + T_{e\omega}s + 1 = a_{c5}s^5 + a_{c4}s^4 + a_{c3}s^3 + a_{c2}s^2 + a_{c1}s + 1. \quad (5.55)$$

Since $l = 2$ the characteristic ratios D_2 and D_3 are set to value 0.5 by using the controller parameters comprising characteristic polynomial coefficents a_{c1}, a_{c2}, a_{c3}:

$$D_3 D_2^2 T_{e\omega}^3 s^3 + D_2 T_{e\omega}^2 s^2 + T_{e\omega} s + 1 = a_{c3} s^3 + a_{c2} s^2 + a_{c1} s + 1. \quad (5.56)$$

Taking into account the frequency ratio,

$$r_{EM} = \Omega_0 T_{\Sigma\omega} = 0.0155 \ll 0.3 \quad (5.57)$$

and the ratio of BSG rotor and ICE crankshaft intertia

$$r_M = \frac{J_{ICE}}{J_{BSG}} = \frac{\Omega_0^2}{\Omega_{02}^2 - 1}, \quad (5.58)$$

the expression for a_{c3} coefficent can be simplified [25]:

$$a_{c3} = T_{c\omega}\left[\frac{J_{BSG}(1 + r_M)T_{\Sigma\omega}}{K_{c\omega} k_t} + \Omega_{02}^{-2}\right] = T_{c\omega}\left[T_{\Sigma\omega}\Omega_0 \frac{J_{BSG}\Omega_0}{K_{c\omega} k_t}\Omega_{02}^{-2} + \Omega_{02}^{-2}\right] \approx \approx T_{c\omega}\Omega_{02}^{-2}. \quad (5.59)$$

Finally, with (5.51) taken into account, the following expressions for the parameters of BSG speed PI controller are obtained:

$$T_{c\omega} = T_{e\omega}, \quad (5.60)$$

$$T_{e\omega} = \frac{1}{D_2\sqrt{D_3}\Omega_{02}}, \quad (5.61)$$

$$K_{c\omega} = \frac{T_{c\omega}}{k_t}\frac{(J_{BSG} + J_{ICE}/i_{belt}^2)\Omega_{02}^2}{D_2 T_{c\omega}^2 \Omega_{02}^2 - 1}. \quad (5.62)$$

Some arbitrary load should be defined before proceeding to simulate the vibrations damping cascade control structure with controller parameters given by *(5.30) – (5.32)* and *(5.52) – (5.54)*.

5.2.6. ICE crankshaft main bearing friction torque

For the sake of simulation analysis, the load acting upon the machine rotor will be on the side of ICE crankshaft in the form of a Stribeck curve given by the following expression:

$$m_{MB}(\omega_{ICE}) = \left[M_C + (M_S - M_C)e^{-\left|\frac{\omega_{ICE}}{\omega_S}\right|^{\delta}}\right] sgn(\omega_{ICE}), \quad (5.63)$$

where M_C is the Coulumb static friction torque, M_S the maximum value of static friction torque, or the breakaway torque, ω_S the Stribeck speed and δ the Stribeck coefficient which appropriates values from on the interval $0.5 \leq \delta \leq 2$. The Stribeck curve defined by expression *(5.55)*, with linear approximation of static friction discontinuity, is shown in figure 44.

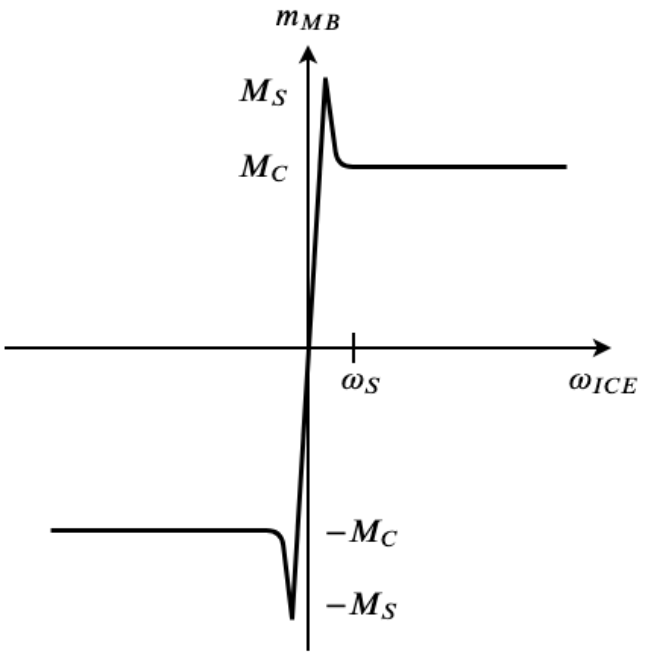


Fig. 44 Stribeck friction curve

The vibrations damping cascade control structure with controller parameters given by *(5.30) – (5.32)* and *(5.52) – (5.54)* modelled in SIMULINK is shown on figure 45. It is coupled with the two-mass accessory drive dynamics from chapter 5.2.4. loaded by the 13 Nm peak Stribeck friction at ICE side. Parameters of the BSG, FEAD and the control system are given in table 1.

In the following chapter simulation results will first be presented for the case of FEAD belt dynamics being described by the torsional model from figure 39 and then compared to the case of longitudinal model from figure 38. For each case, the BSG speed control system response will be presented with its parameters synthesized using the damping optimum criterion taking into account the elasticity of the timing belt, i.e. with the parameters given by *(5.52) – (5.54)*. Next, its parameters will be changed to values also analytically synthesized using the damping optimum criterion, but with the assumption that the coupling between the ISG rotor and ICE crankshaft is rigid. This will be done only for the torsional model case, since the results will be the same, that is, undamped belt vibrations manifesting as torsional vibrations of the BSG rotor and ICE crankshaft. This is done to emphasize the effect of different BSG speed control system tuning to its vibrations damping ability.

After that, the cut-off logic is switched on, which cuts of the BSG torque after it has reached the referent speed, thus simulating the stop/start functionality discussed in chapter 1.4.1. The boosting function won't be simulated using MATLAB/SIMULINK, but AVL CRUISE^{TM} M simulation environment in later chapters.

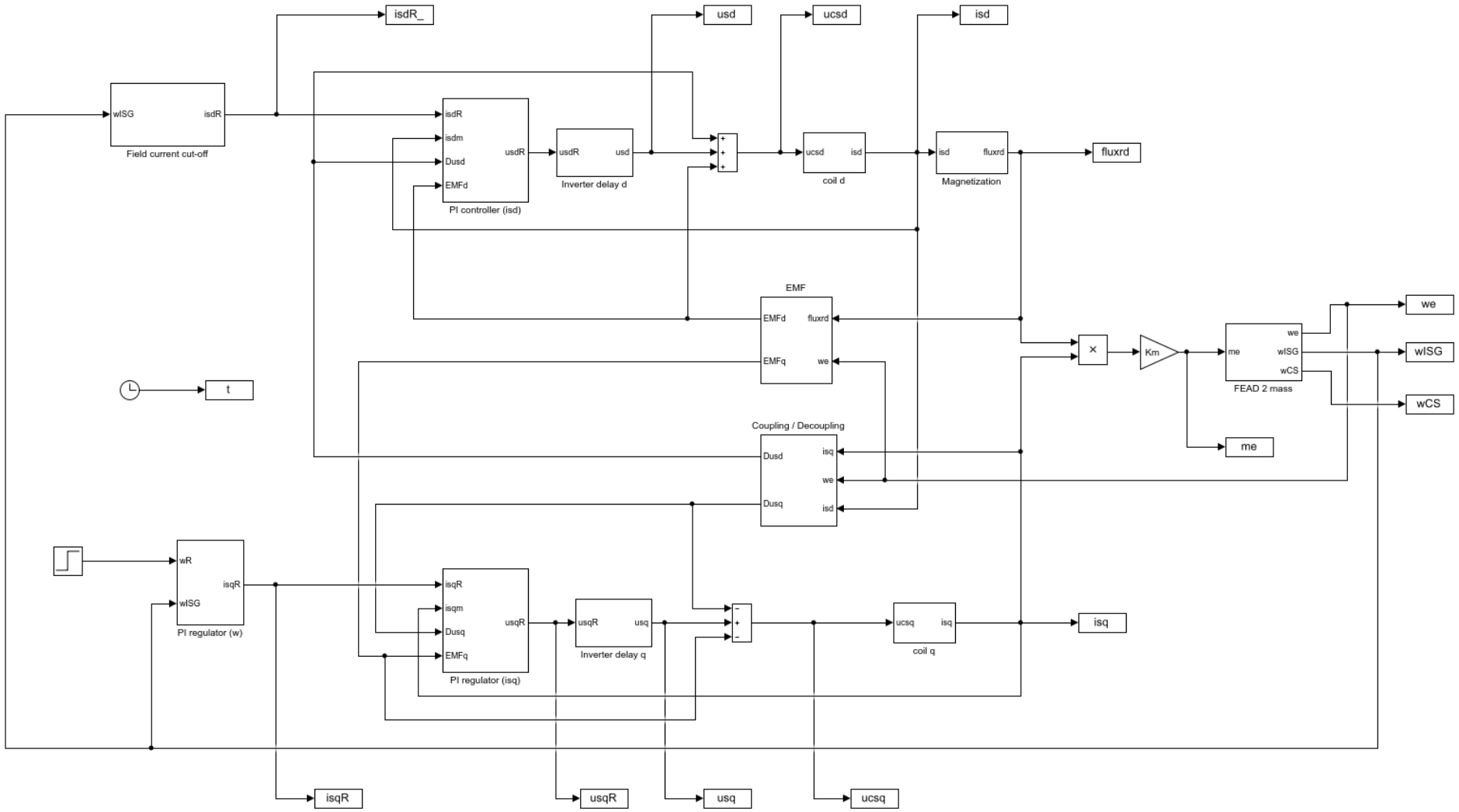


Fig. 45 Simulink model of BSG speed/current cascade control structure, BSG mathematical model in dq coordinate system and accessory drive dynami

Table 2 System parameters

BSG	
Stator winding resistance, R_s , Ω	0,0133
Rotor winding resistance, R_r , Ω	0,0233
Stator inductance L_s, H	7,5*10^{-5}
Rotor inductance L_r, H	7,5*10^{-5}
Magnetizing inductance L_m, H	6,75*10^{-5}
Number of pole pairs, p	4
FEAD	
BSG inertia J_{BSG}, kgm^2	0,003
ICE crankshaft inertia J_{BSG}, kgm^2	0,12
BSG pulley radius r_{BSG}, m	0,0316
ICE pulley radius r_{ICE}, m	0,0753
Belt longitudinal stiffness EA, N	65500
Belt length L, m	1,3784
Damping factor f_d, s	1,4*10^{-5}
Current control system	
Constant field current reference i_{sdR}, A	400
Inverter time constant T_{inv}, s	4*10^{-5}
Sample time T_s, s	4*10^{-5}
Voltage limit U_{max}, V	48
Current limit I_{max}, A	500
PI i_q and i_d controller time constant T_{ci}, s	4,4313*10^{-4}
PI i_q and i_d controller gain K_{ci}, Ω	0,1187
Speed control system, elastic tuning, *(5.53) – (5.54)*	
Sample time $T_{s\omega}$, s	4*10^{-5}
PI ω_{BSG} controller time constant $T_{c\omega}$, s	0,0596
PI ω_{BSG} controller gain $K_{c\omega}$, kgm^{2}s^{-1}H^{-1}A^{-1}	6,8113
Speed control system, rigid tuning, *(5.60) – (5.61)*	
PI ω_{BSG} controller time constant $T_{c\omega}$, s	5,6*10^{-4}
PI ω_{BSG} controller gain $K_{c\omega}$, kgm^{2}s^{-1}H^{-1}A^{-1}	543,7978

5.3. Simulation results

5.3.1. Simulation results using the FEAD model with torsional dynamics of the belt

Figure 46 presents the system response with the BSG speed/current control system tuned for accessory drive vibrations damping, i.e. with parameters given by *(5.52) – (5.54)*. Figure 47 gives the responses of BSG field and torque currents, along with the rotor flux generated.

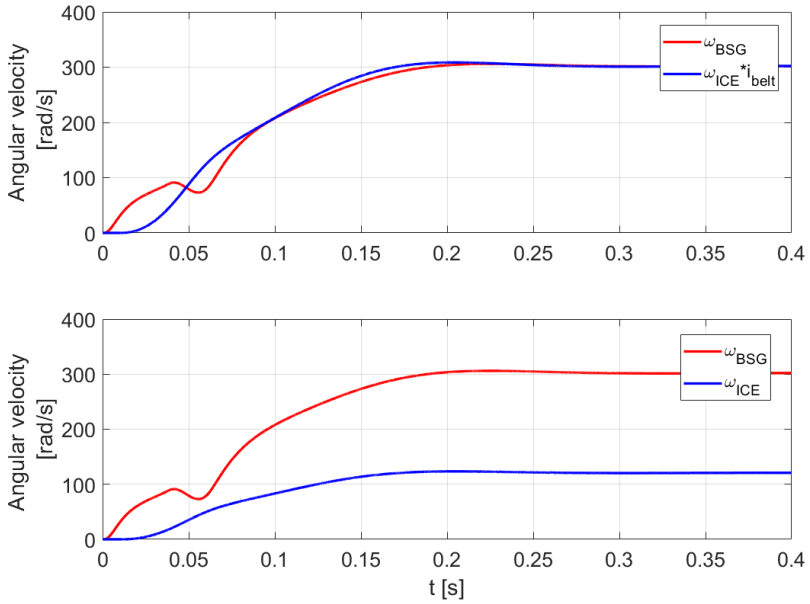


Fig. 46 BSG and ICE speed response with the control system tuned for vibrations damping

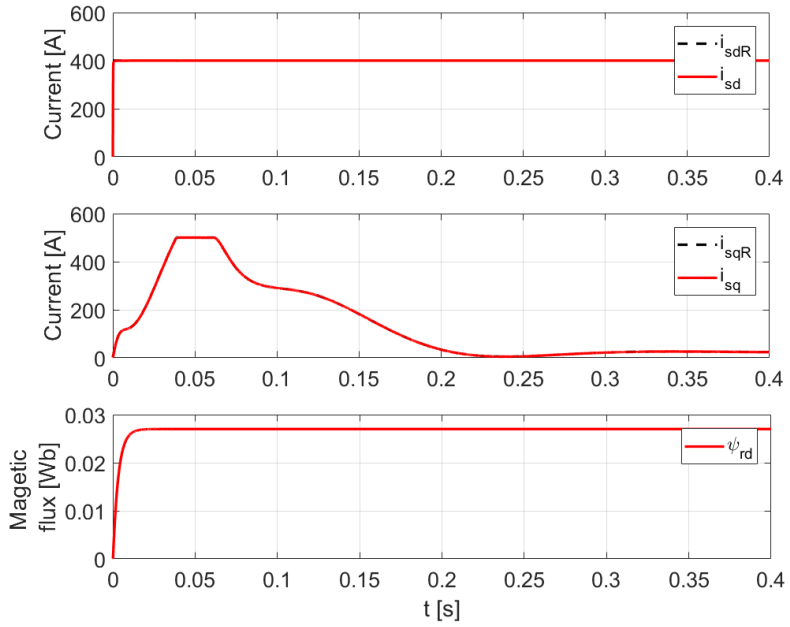


Fig. 47 Torque/field current and rotor flux responses with the control system tuned for vibrations damping

Figure 48 shows the response of the electrical torque m_{BSG} generated by the BSG, along with the response of the belt torque $m_{transferred}$ @ICE transferred from BSG to ICE, which is used to overcome the main bearing friction torque m_{MB} and accelerate the crankshaft. The torque $m_{transferred}$ @ICE is the torque m from expression *(5.38)*. The torque $m_{reactive}$ @BSG opposes the electrical torque m_{BSG}, and is equal to m/i_{belt} as indicated in expression *(5.37)*. These relations are defined by the dynamics of the 2-mass simplification of FEAD from figure 37.

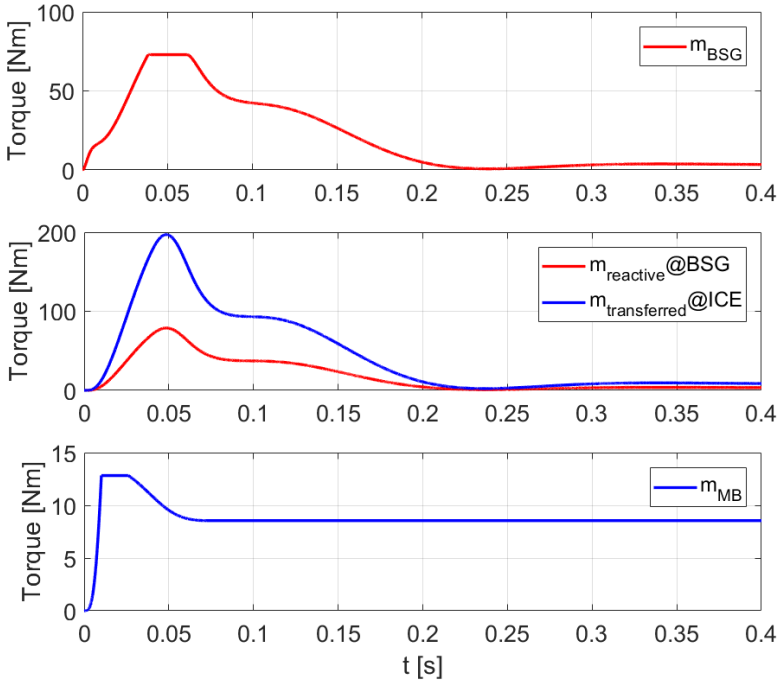


Fig. 48 BSG electrical torque, belt torque and main bearing Stribeck friction torque responses with the control system tuned for vibrations damping

It can be observed from figure 46 that the speed response of both BSG and ICE are well damped and quite fast. This is partially due to the only load being the main bearing friction torque m_{MB}.The torque m transfered by the belt is high, with the peak of 197 Nm owing to high electrical torque being supplied, as well as the transmission ratio of $i_{belt} = 2.5$. This high torque yields a fast ICE crankshaft run-up with only a short delay inherent to the 2-mass elastic model, which differs from the real-life situation, as will be shown by the more precise AVL EXCITE ™ Timing Drive accessory drive model.

Next, the response of the system with the cut-off logic turned on is presented on figure 49. When the BSG reaches the speed reference, the field and torque currents, i_{sd} and i_{sq} are cut

off which results in undamped belt vibrations while the system decelerates, since the electrical torque m_e can no longer be controlled due to the absence of toruqe current.

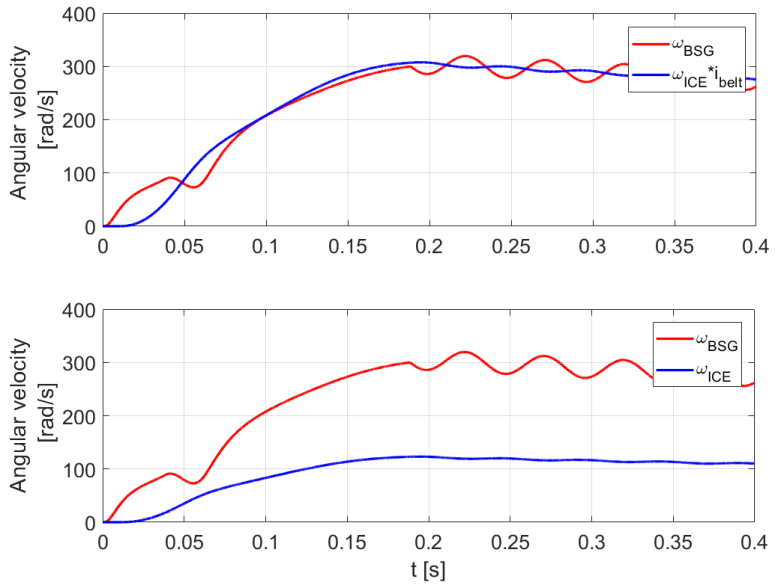


Fig. 49 BSG and ICE speed response with torque cut-off after reaching the referent speed

Now, to illustrate how the system would behave if the damping optimum criterion method wasn't applied to the control system model which takes into account the elasticity of the belt, given by figure 42, but on the model from figure 50, which assumes rigid coupling between the BSG and ICE crankshaft.

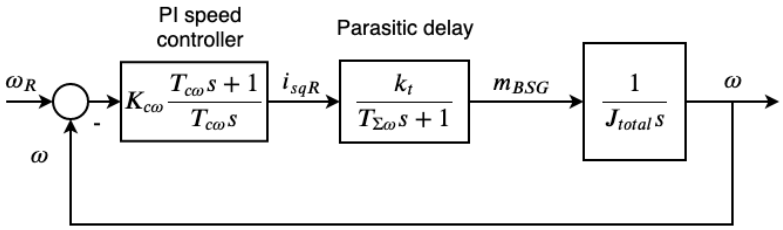


Fig. 50 BSG speed control loop with continuous speed controller and rigid coupling between BSG and ICE crankshaft

Where J_{total} is:

$$J_{total} = J_{BSG} + J_{ICE}/i_{belt}. \tag{5.64}$$

The transfer function of the model from figure 48 is:

$$G_c(s) = \frac{1}{\frac{J_{total}T_{\Sigma\omega}T_{c\omega}}{K_{c\omega}k_t}s^3 + \frac{J_{total}T_{c\omega}}{K_{c\omega}}s^2 + T_{c\omega}s + 1}, \tag{5.65}$$

and after equating the characteristic polynomial of *(5.57)* with the characteristic polynomial of third-order damping optimum criterion:

$$\frac{J_{total}T_{\Sigma\omega}T_{c\omega}}{K_{c\omega}k_t}s^3+\frac{J_{total}T_{c\omega}}{K_{c\omega}}s^2+T_{c\omega}s+1= \\ D_3D_2^2T_{e\omega}^3s^3+D_2T_{e\omega}^2s^2+T_{e\omega}s+1, \tag{5.66}$$

the following expressions for controller parameters are obtained

$$T_{c\omega}=T_{e\omega}, \tag{5.67}$$

$$T_{e\omega}=4T_{\Sigma\omega}, \tag{5.68}$$

$$K_{c\omega}=\frac{J_{total}}{2T_{\Sigma\omega}k_t}. \tag{5.69}$$

The system BSG and ICE speed responses with parameters tuned in this manner are shown on figure 51.

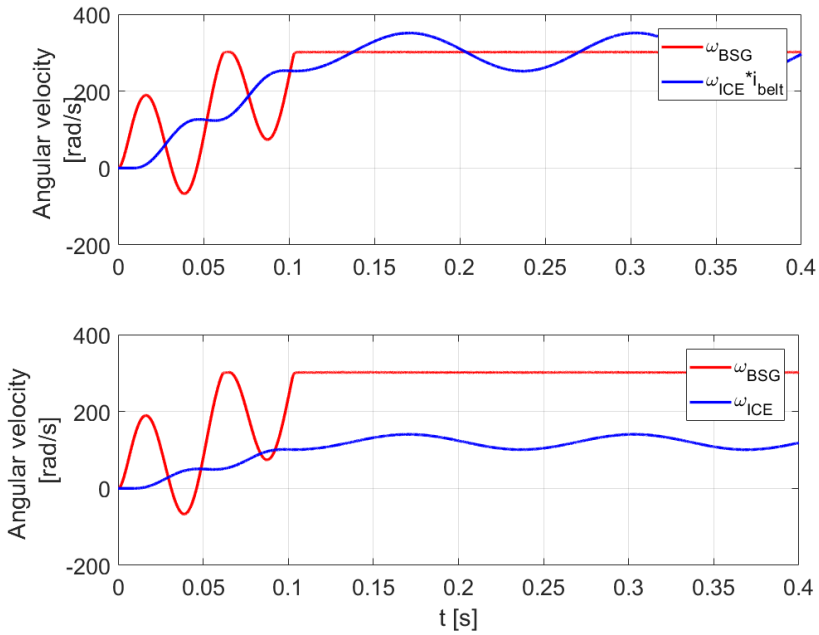


Fig. 51 BSG and ICE speed response with the control system tuned as if the coupling between them was rigid

It can be observed from figure 51 that this kind of tuning results in undamped FEAD belt vibrations which are manifested as torsional vibrations of the BSG rotor and ICE crankshaft. These vibrations occur because the speed of BSG isn't controlled anymore with the emphasis on vibration damping, which propagates its self through the torque current i_{sq} and finally reaching the torque of the machine, causing the response seen on figure 53. Behavior of current and torque responses can be observed on figures 52 and 53.

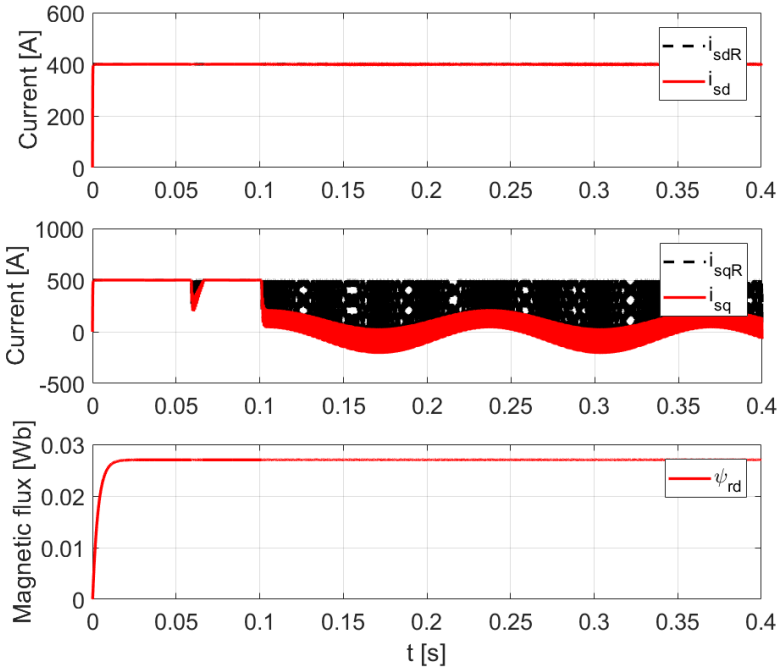


Fig. 52 Torque/field current response with the control system tuned as if the coupling between them was rigid

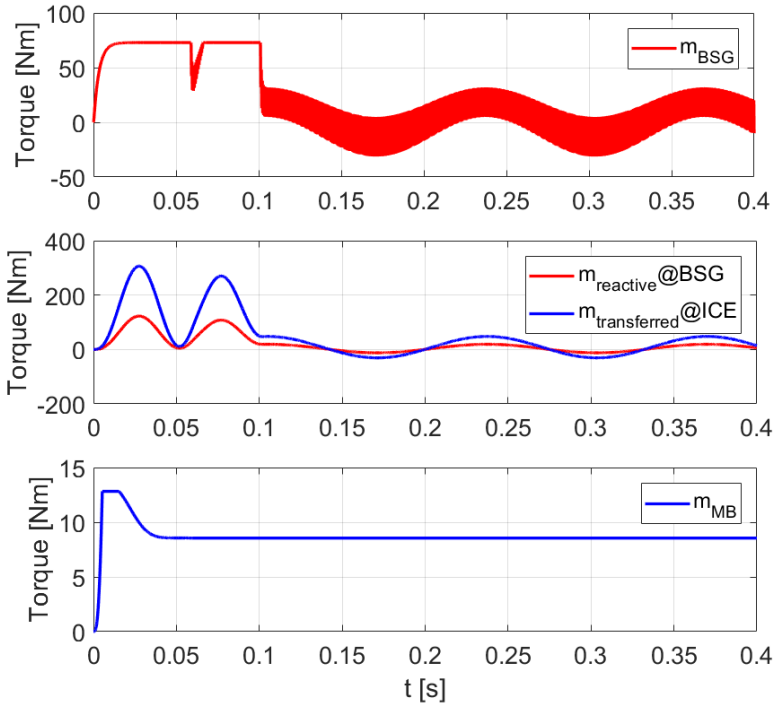


Fig. 53 BSG electrical torque, belt torque and main bearing Stribeck friction torque responses with the control system tuned as if the coupling between them was rigid

5.3.2. Comparison with the response of the system using the FEAD model with longitudinal dynamics of the belt

In this chapter will be shown that the BSG control system tuning yielded from the approximation *(5.42)* made in chapter 5.2.4, in order to obtain a FEAD system model favorable for synthesizing the controller parameters according to the procedure described in [24], results in the same behavior of the FEAD system with the belt dynamics modeled as longitudinal (figure 38) as it does for the torsional model (figure 39).

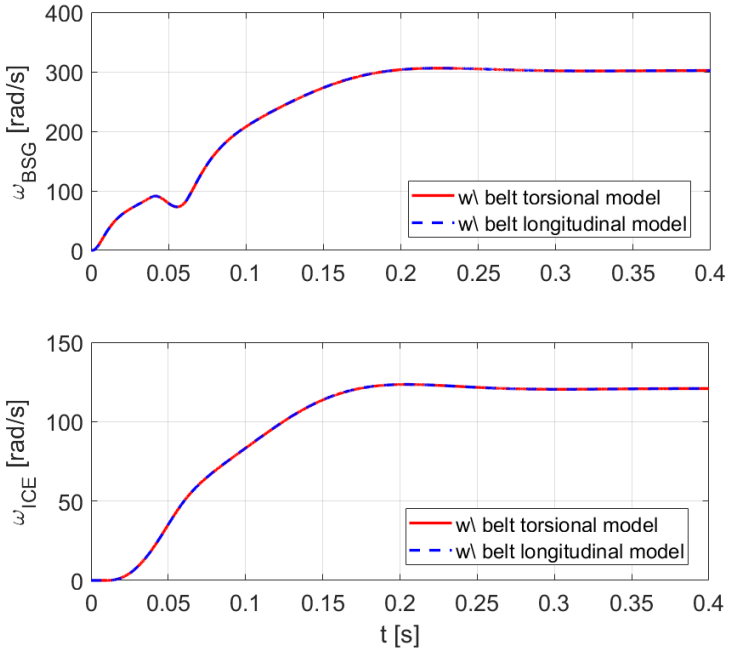


Fig. 54 Speed response comparison for the torsional vs. longitudinal model of the FEAD belt dynamics

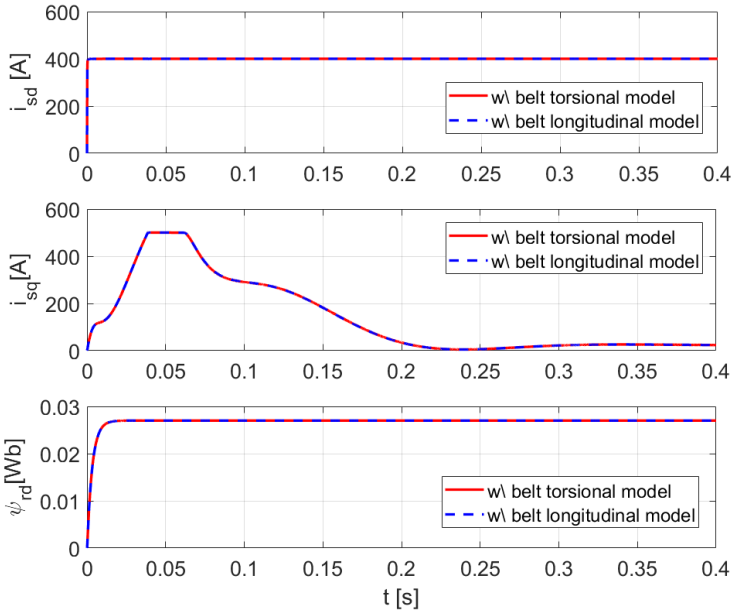


Fig. 55 Current and rotor flux response comparison for the torsional vs. longitudinal model of the FEAD belt dynamics

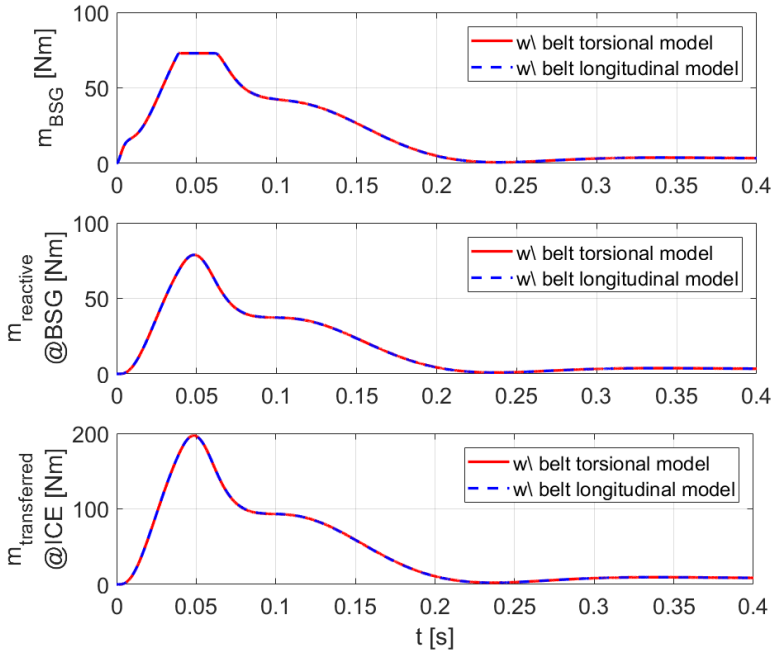


Fig. 56 Torque response comparison for the torsional vs. longitudinal model of the FEAD belt dynamics

There are certain physical phenomena that the dynamics of the 2-mass FEAD simplification doesn't take into account, such as slip between the belt and the pulleys. Due to this, the transient response of the FEAD model is not accurate enough when its dynamics is simplified by equations *(5.34)* – *(5.36)*. In order to obtain a more accurate response, a specialized multi-body dynamics simulation environment must be used.

6. AVL EXCITE ™ FEAD MODEL

6.1. AVL EXCITE ™

AVL EXCITE ™ is a rigid and flexible multi-body dynamics software for powertrain analysis. EXCITE ™ supports the modelling of components, subsystems and complete powertrains with different levels of detail. This ensures that the optimum balance between the simulation effort and accuracy can be achieved in accordance with analysis demands [26]. Figure 57 shows friction analysis in a 4-cylinder engine using EXCITE ™, which represents one of many use cases for this software.

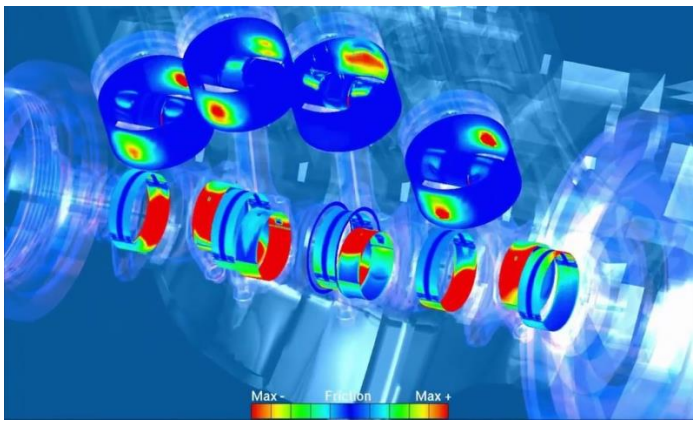


Fig. 57 Friction analysis in a 4-cyliner engine using EXCITE™

Using EXCITE ™ reduces the need for prototyping and helps to avoid expensive troubleshooting. Furthermore, it facilitates short project lead times due to high computational efficiency and application oriented and automated post-processing. Result data evaluation can be customized in a dedicated environment that supports report generation by 3rd party developed apps and workflows [26].

In the scope of this thesis, the Timing Drive module of EXCITE ™ is used to model the FEAD and to couple it with the BSG model from MATLAB in order to perform a cosimulation, which will yield more accurate results than those presented in chapter 5.3. EXCITE ™ Timing Drive is a dedicated module that specializes in the analysis of belt driven system and as such it is able to capture physical phenomena that the dynamics of the 2-mass FEAD approximation used previously could not, namely the slip between the belt and the pulleys. The next chapter presents the accessory drive model from EXCITE ™ Timing Drive.

6.2. EXCITE ™ Timing Drive FEAD model

The accessory drive is modeled using the Non Toothed Belt macro element where all the data relevant to the drive is defined. Firstly, global data is defined as shown by figure 58.

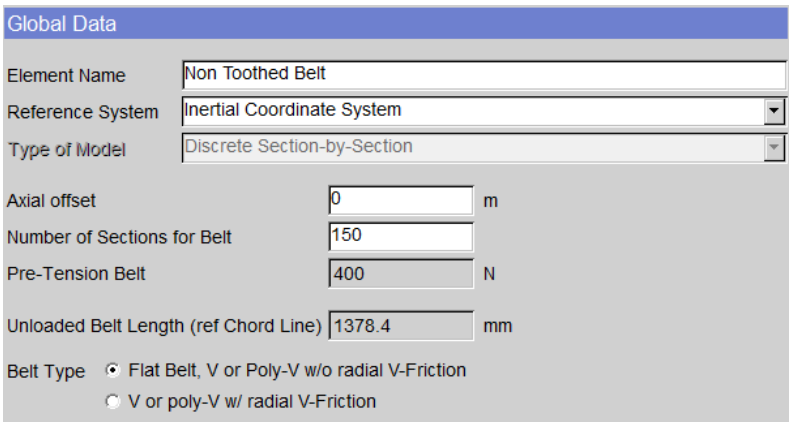


Fig. 58 Global data

After that the drive layout considering the number of pulleys, pitch diameters, absolute coordinates, contact, function and speed at the start of the simulation has to be defined as shown by figure 59.

Drive Layout (Order of Elements along Belt's Running Direction)

Element	Pitch Diam	Y	Z	Contact	Function	Speed
	m	m	m			rpm
1_CS	0.1508	0	0	back	Pulley	1e-5
2_Tens1	0.0621	0.0831356	0.174671	front	Tens. Pulley	-2.42835e-
3_ISG	0.06032	0.1508	0.2262	back	Pulley	2.50001e-0
4_Tens2	0.0621	0.09083	0.27289	front	Pulley	-2.42835e-
5_WP	0.12632	-0.1108	0.2516	back	Pulley	1.1938e-05
6_Idler	0.0721	-0.0377	0.1308	front	Pulley	-2.09154e-

Fig. 59 Drive layout

This is followed by the definition of pulley properties such as DoFs (Degrees of Freedom), mass, moment of inertia and friction factor.

Pulley Properties

Element	DoFs	Mass	Mol A	Mol B	Mol C	μ
		kg	kg.m^2	kg.m^2	kg.m^2	
1_CS	rotary		0.12			Belt
2_Tens1	rotary		2.2e-05			Belt
3_ISG	rotary		0.003			Belt
4_Tens2	rotary		2.2e-05			Belt
5_WP	rotary		0.00177			Belt
6_Idler	rotary		0.00021			Belt

Fig. 60 Pulley properties

Tensioner geometry can also be defined. However, since there will be no active tensioner in the model, this area is left as default. This decision has been made in order to keep the model as simple as possible in order to avoid numerical issues that can arise from two different solvers, i.e. MATLAB solver and EXCITE ™ solver working together. The active tensioner can be added later on when this simpler iteration of the FEAD model has been confirmed to work properly in the cosimulation.

Tensioner Geometry

Motion of Tensioner: Rotational

Pivot Point of Tensioner Arm

e2	e3
m	m
0	0

Sense of Tensioner Arm Rotation to Increase Belt Tension: Positive / Negative

Fig. 61 Tensioner geometry

Belt geometry and mass data must also be defined:

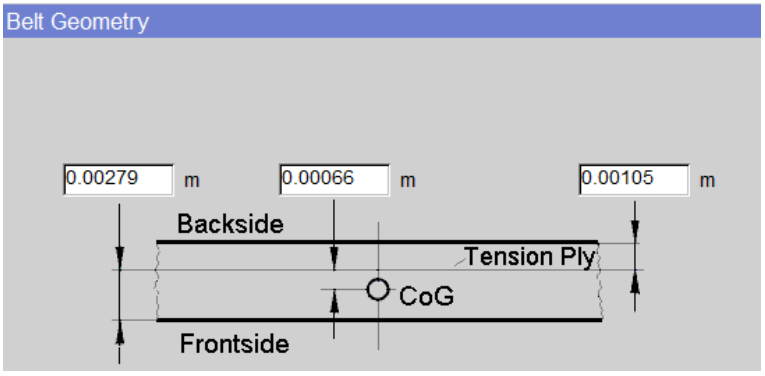


Fig. 62 Belt geometry

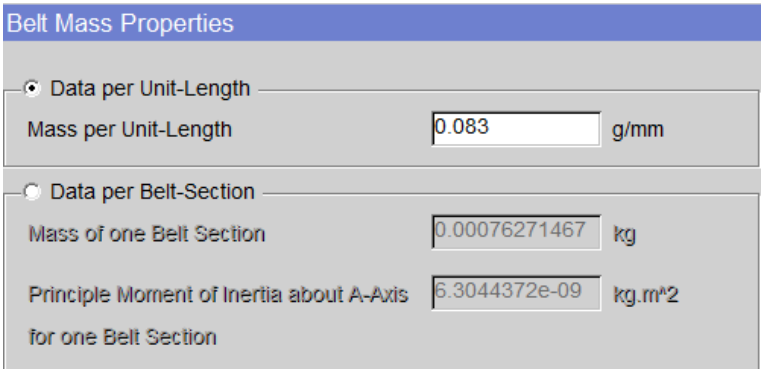


Fig. 63 Belt mass properties

The belt elasticity properties are as follows:

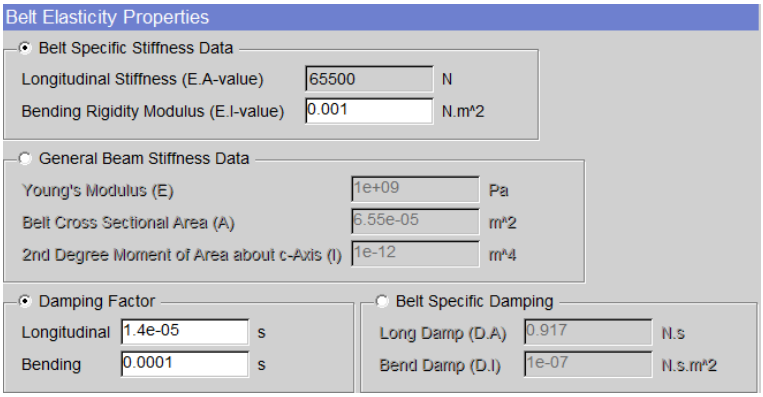


Fig. 64 Belt elasticity properties

The equivalent torsional stiffness and damping coefficients from the 2-mass FEAD approximation from MATLAB were defined from the data presented in the above figure. The expression for axial stiffness of an element undergoing tension or compression is defined by:

$$k_L = \frac{EA}{L}, \qquad (6.1)$$

which is easily obtained from the parameters given in this chapter or from table 2 in chapter 5.2.6. The longitudinal damping factor is obtained according to [27] by using the following expression:

$$d_L = f_d k_L. \qquad (6.2)$$

The last thing to specify in the settings of the Non Toothed Belt macro element is the contact stiffness and damping, as well as the friction parameters of the front and back side contacts between the belt and the pulleys.

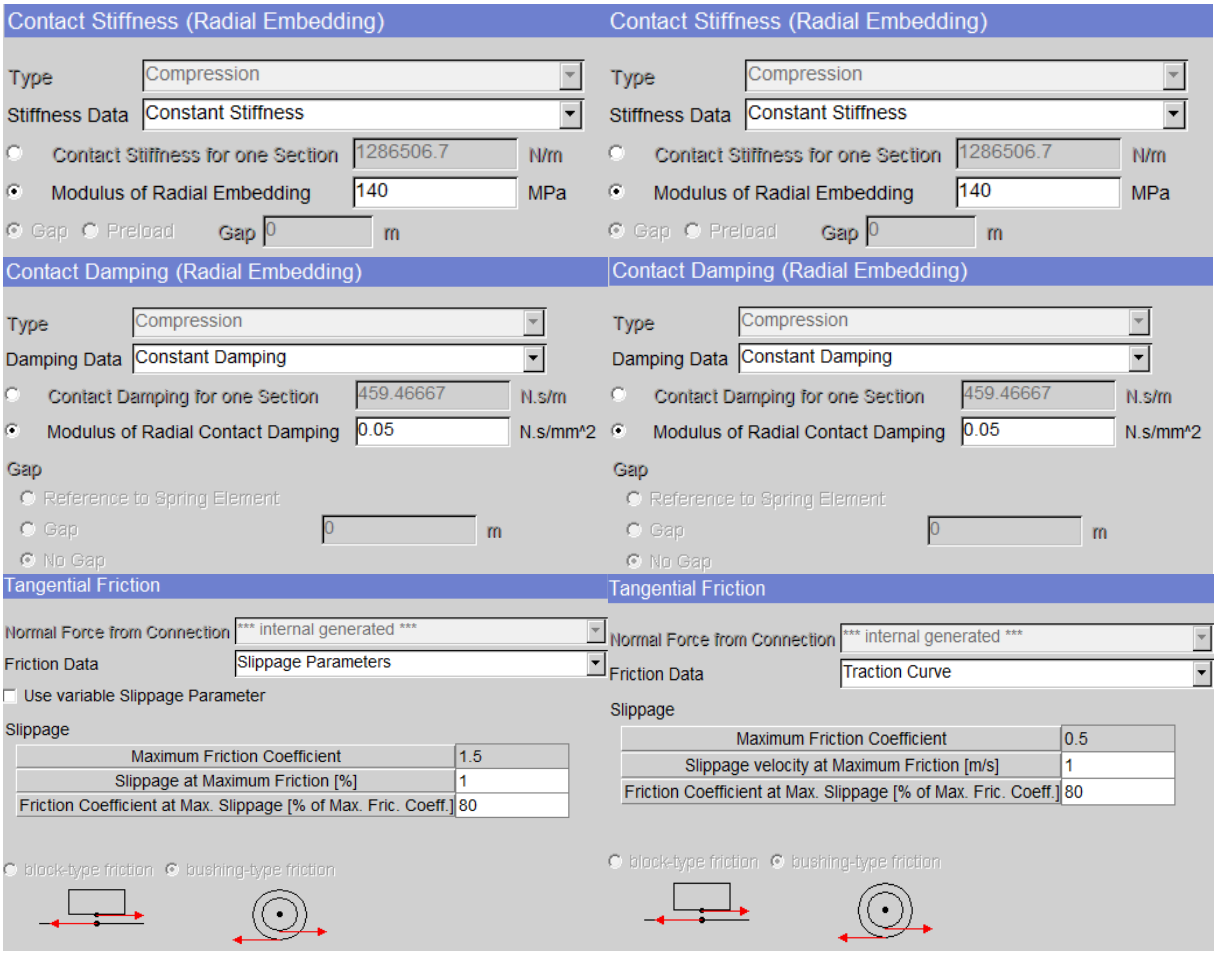


Fig. 65 Stiffness, damping and tangential friction of belt and pulley front and back side contacts

The depicted setup results in the following model

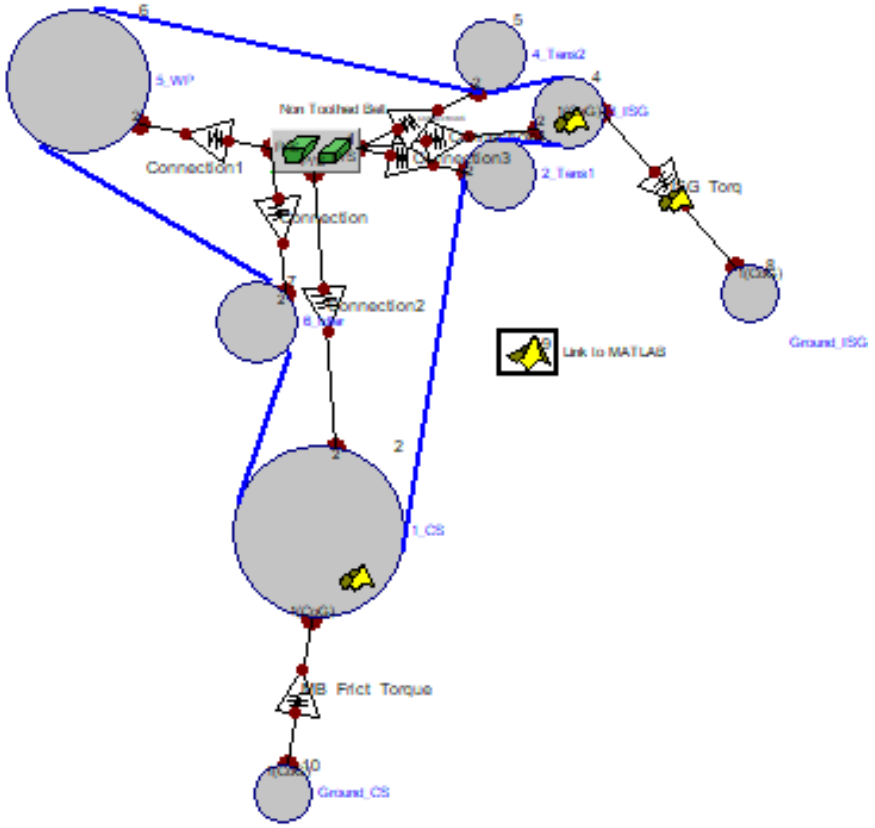


Fig. 66 FEAD Multi Body Model – 2D View

When viewed in 3D, the specialized elements used to discretize the timing belt can be noticed on the left side of the figure.

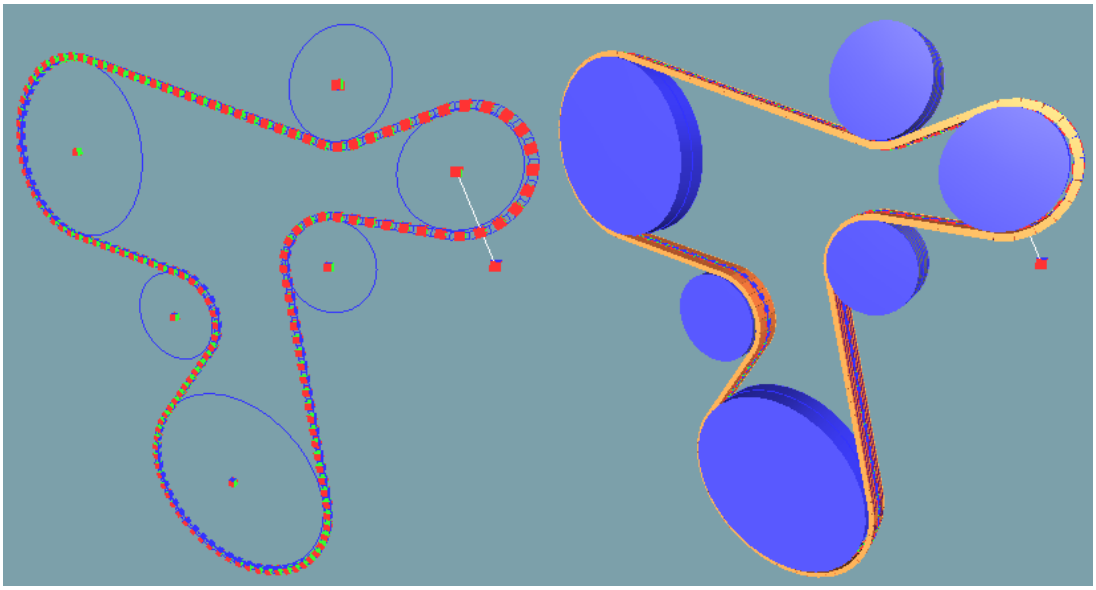


Fig. 67 FEAD Multi Body Model – 3D View

This model will be used in cosimulation with MATLAB in order to test the performance of the BSG speed control system with parameters tuned according to damping optimum

criterion, which mitigates the vibrations of the timing belt manifesting themselves as torsional vibrations of the BSG rotor and ICE crankshaft, as was described in chapter 5. Before proceeding to the coupling of EXCITE ™ and MATLAB, some load needs to be defined in EXCITE ™, since it simulates the mechanical part of the system, that is the FEAD. The same Stribeck curve used in the MATLAB simulation is defined here in order to obtain a similar response. This is the only load acting on the system.

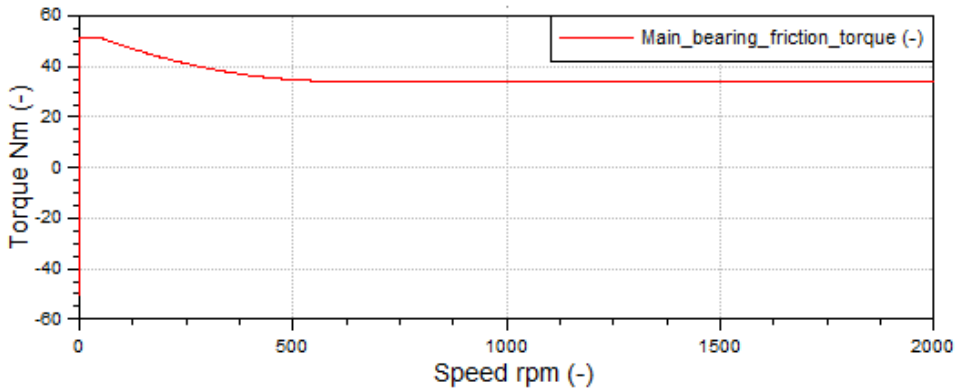


Fig. 68 Friction characteristic of the crankshaft bearing

6.3. MATLAB cosimulation setup

The connection between MATLAB and EXCITE ™ is made with the S-function block in Simulink, serving as an interface between these two software. EXCITE ™ is the master in this connection, which means it controls the time step size and convergency [28]. All results are passed from EXCITE ™ to MATLAB/SIMULINK unchanged via the S-function interface and vice versa. This is the principle on which the cosimulation is based and it's illustrated on figure 69 using a familiar model.

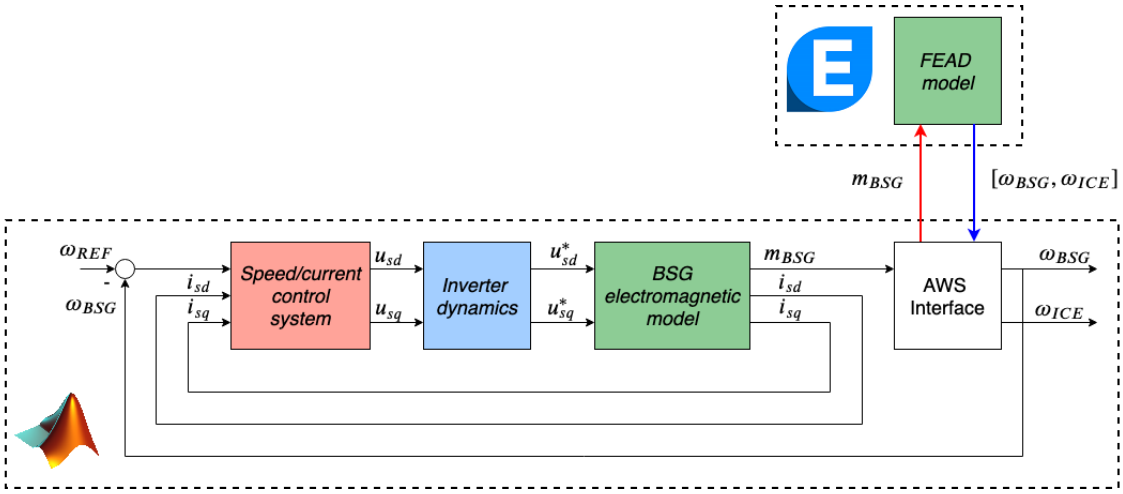


Fig. 69 Scheme of the model for EXCITE ™/MATLAB cosimulation

The interface block in Simulink is shown on figure 70. The number of input vectors (BSG torque, BSG mass element, ICE mass element) and output vectors (BSG torque, BSG speed DOFs, ICE speed DOFs) has to be equal to the number of connections defined in "Link to MATLAB" block on the EXCITE ™ side.

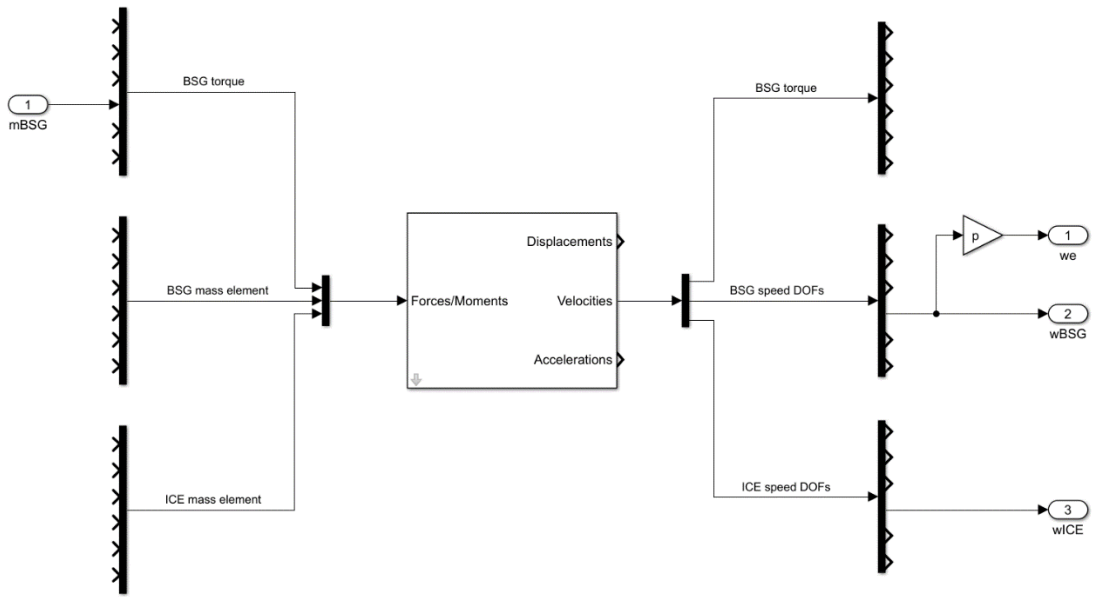


Fig. 70 EXCITE ™ interface block in Simulink

Every vector has 6 elements that describe 6-DoF state of each connection made on EXCITE ™ side. The first three elements of that vector are translational DoF and other three are rotational DoF.

Since there will be three connections on EXCITE ™ side in this cosimulation, which is shown on figure 73, three such vectors carrying the information about the DoF state of each connection will be formed on EXCITE ™ side and combined into a single vector before being sent to MATLAB. This can be observed by looking at the innermost demultiplexer element on the right side of the interface block on figure 70, which has a function of separating that combined vector into three separate vectors carrying information about the DoF of each connection respectively.

The process of sending forces/torques from MATLAB to EXCITE ™ is analogous to this procedure. The number of input vectors defined has to be equal to the number of output vectors received from EXCITE ™, each having exactly six elements, and passed through the innermost multiplexer block before being sent to EXCITE ™ as a single combined vector.

The connection on EXCITE ™ side is made via the "Link to MATLAB" block in which the path to the Simulink model has to be defined along with the elements which are to be connected to the interface and their respective connection type.

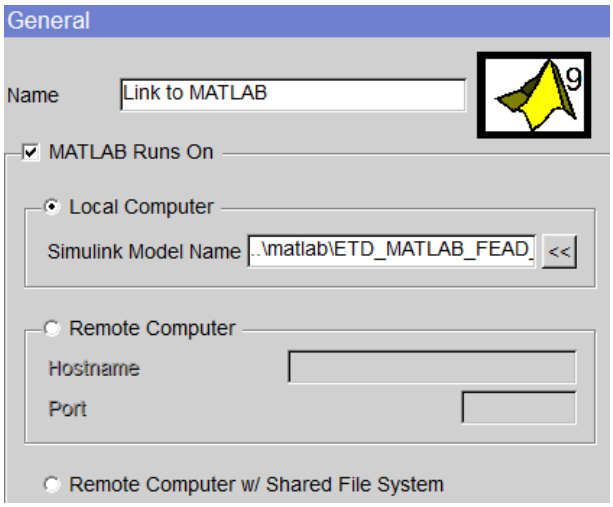


Fig. 71 Setup of Simulink model path in EXCITE ™ "Link to MATLAB" block

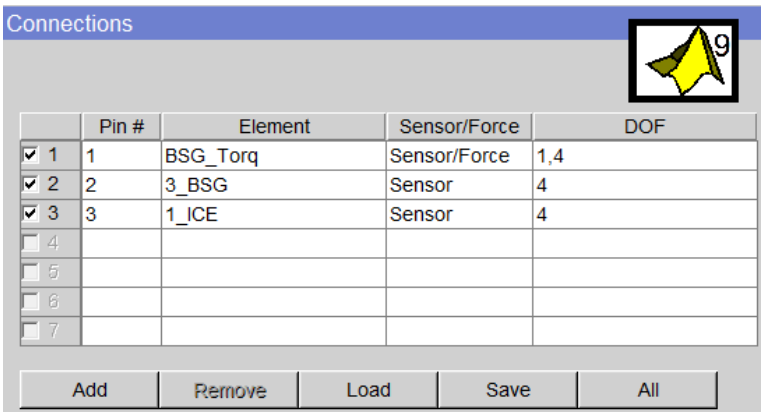


Fig. 72 Setup of elements to be connected to the interface with MATLAB and their respective connection types in EXCITE ™ "Link to MATLAB" block

Available connection types are "Sensor" and "Sensor/Force". The "Sensor" type connection is used for elements that only export motion and "Sensor/Force" type is used for elements that can export motion and receive forces/torques from MATLAB. This concludes the preparation of both EXCITE ™ and SIMULINK model for the cosimuation. The results of the cosimulation are presented in the next chapter.

6.4. EXCITE ™/MATLAB cosimulation results

Figure 73 shows BSG and ICE speed responses, along with the torque received on the BSG side from the MATLAB model through the S-function, as well as the torque transferred to the ICE crankshaft.

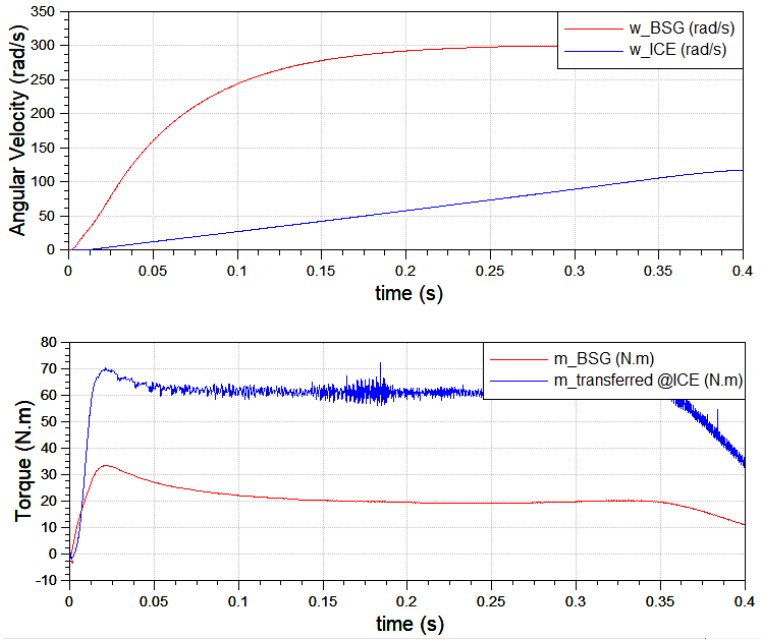


Fig. 73 Cosimulation results

In order to see the difference between the speed responses of the EXCITE ™ model and the two-mass MATLAB approximation from chapter 5, the results from figure 73 are plotted against the results from figures 46.

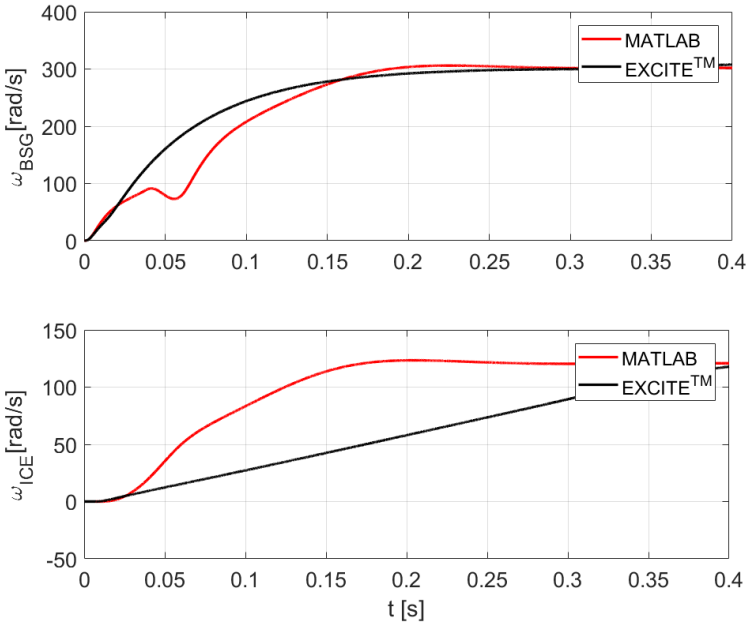


Fig. 74 Speed response comparison between EXCITE ™ and MATLAB

The difference in ICE crankshaft speed is apparent, and in order to investigate the reason behind such result the torques generated at BSG side and torques transferred from the BSG to the ICE in both MATLAB simulation and EXCITE ™ cosimulation must be plotted against one another.

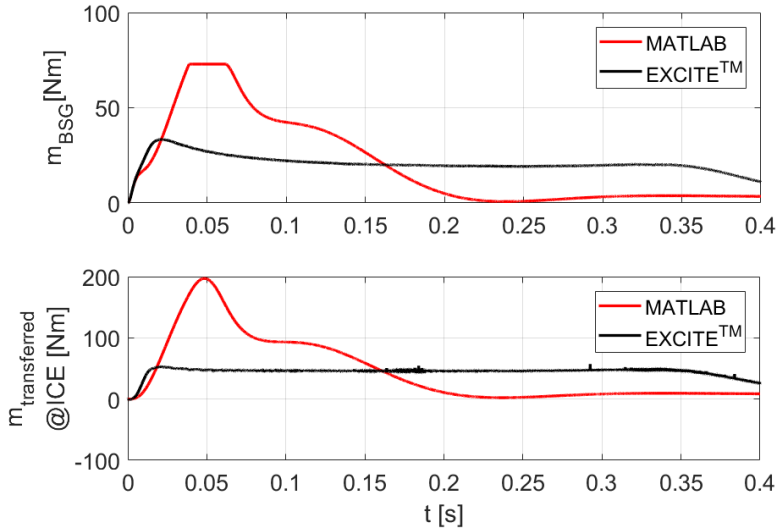


Fig. 75 Torque response comparison between EXCITE ™ and MATLAB

On figure 75 the torques accelerating the BSG and the ICE both in MATLAB simulation and EXCITE ™ cosimulation can be observed. The MATLAB torques seem to be significantly bigger than those generated and transferred in EXCITE ™. So, the large difference in torques transferred to ICE explains the difference in ICE speed responses obtained from MATLAB versus the ones obtained from the cosimulation.

The torque difference is explained by the expressions

$$m = k_T(\alpha_{BSG} - \alpha_{ICE}) + d_T\left(\frac{\omega_{BSG}}{i_{belt}} - \omega_{ICE}\right), \qquad (6.3)$$

which determines the torque transferred from BSG to ICE in MATLAB simulation by a single spring/damper joint defined by its torsional stiffness and damping. This model does not take into account the slippage phenomenon where the velocity of the specialized belt segments transferring torque in EXCITE ™ cosimulation is bigger than the speed of the ICE pulley, which hinders torque transfer from the belt to the pulley. Consequently, the torque transferred to ICE is built up much faster in MATLAB simulation than in the cosimulation where the slippage effect is taken into account, so the ICE accelerates slower in the cosimulation.

Another effect that can be observed from figures 74 and 75 is that although the BSG torque generated in MATLAB simulation is significantly bigger than the one generated in the cosimulation, the speed response does not differ in the same manner. This is explained by the expression

$$J_{BSG}\frac{d\omega_{BSG}}{dt} = m_{BSG} - \frac{m}{i_{belt}}, \qquad (6.4)$$

where the torque transferred from BSG to ICE in MATLAB simulation by a single spring/damper joint is scaled by the transmission ratio of the belt drive i_{belt} in order to express the reactive torque, which the electrical torque m_{BSG} has to overcome in order to accelerate the BSG rotor. The reactive torque is lower in the cosimulation due to the occurrence of slip which prevents this torque from generating quickly, since it is directly proportional to the torque transferred to the ICE. The result of this is that the lower values of m_{BSG} are requested from the control system because the reactive torque is lower. Consequently, the torques available to accelerate the BSG rotor after overcoming the reactive torque are roughly the same in both MATLAB simulation and EXCITE ™ cosimulation, as indicated by figure 76. Since the inertia of the BSG rotor are the same in both cases, it is logical that the speed response will be similar.

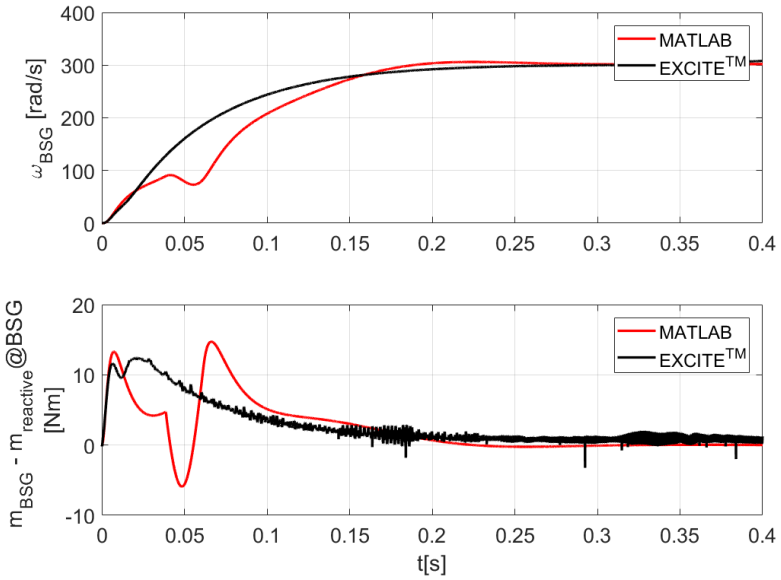


Fig. 76 Response comparison between EXCITE ™ and MATLAB of torque available for BSG acceleration

The slippage of the belt is analyzed by observing specialized finite elements, shown on figure 67, that comprise the discrete representation of the timing belt. The number of these elements was set to be 150. Since many of these elements are in contact with the ICE crankshaft pulley at the same time, which is also seen from figure 67, it would be quite an unpleasant representation to plot the slippage between the crankshaft pulley and all of the discrete elements contacting it during the cosimulation on the same plot. So, in order to present a clear picture, the slippage between the ICE pulley and every 30th finite element is plotted on figure 77. Many of these elements come into contact with the ICE pulley multiple times during the cosimulation, like the ones named MASS 30, MASS 60 and MASS 90, observed from figure 77. It has been

shown that the slippage percentage tends to be bigger at the beginning of the cosimualton, higher than 35 %. This was expected since there is no active tensioner in the system that would keep the belt tightened at all times. The slippage calculation is prone to numerical errors at the beginning of the cosimulation, as is indicated by the bottom chart on figure 77, where slippage percentages of over $-3*10^6$ % are present.

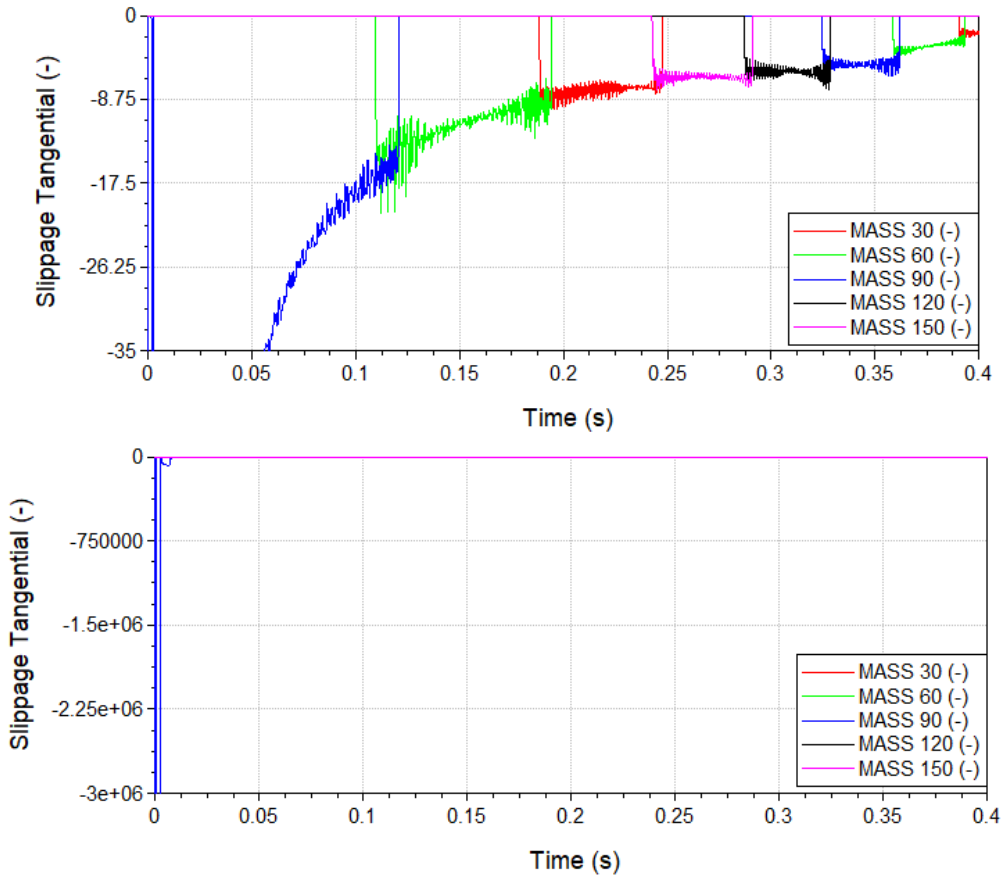


Fig. 77 Analysis of belt slippage by observing specialized finite "MASS" elements contacting the pulleys at given time periods

The overall conclusion is that the EXCITE ™ is better suited for modeling of the FEAD system since it can take into account slippage and other phenomena which would have to be manually modeled if a simulation software like MATLAB would be used instead. The MATLAB model was useful to tune the control system in order to achieve a well damped behavior of the FEAD which was confirmed by BSG speed response without torsional vibrations.

In the next chapter the SIMULINK model of the BSG and its control system shown on figure 45, excluding the FEAD model, is compiled as an FMU (Functional Mock-Up) unit and implemented within AVL CRUISE ™ M simulation environment.

7. AVL CRUISE ™ M SYSTEM SIMULATION

7.1. AVL CRUISE ™ M

AVL CRUISE ™ M is a multi-disciplinary vehicle system simulation tool that can be used for powertrain concept analysis, sub-system design and virtual component integration. It also has the ability to be used for control function development in HiL (Hardware -in-the-Loop) and testbed environments [29].



Fig. 78 Vehicle model in CRUISE ™ M featuring integrated models of different subsystems

The ability to analyze powertrain concepts in AVL CRUISE ™ M enables vehicle makers to predict fuel efficiency and performance early in the concept phase, even when little data is available. CRUISE ™ M enables the modelling of the driveline, electric network and control strategies, while showing their impact upon energy consumption and emissions. The software is very flexible which allows the designer to easily switch between conventional, hybrid and electric powertrain concepts [29].

The sub-system analysis in CRUISE ™ M can be performed in different physical domains by enabling the designer to model thermodynamic, mechanical, chemical, flow and electrical systems and to integrate them in the same simulation. The benefit of this is that the detailed design layout and optimization of numerous sub-systems can be made, such as engine gas exchange and combustion, exhaust gas aftertreatment system, driveline, cooling circuit, electric network, hydraulic and pneumatic networks and HVAC systems [29].

In vehicle simulation on testbeds one of the key benefits of CRUISE ™ M can be utilized. That is, the models made in this software can be used as plant models on engine, powertrain and chassis dyno testbeds. This is favorable for controller validation and component testing [29].

In the scope of this thesis the CRUISE ™ M system simulation environment will be used to integrate the induction motor and control system model from Simulink, compiled as an FMU, into an existing manual transmission ICE vehicle architecture, that can be found in the examples library of the CRUISE ™ M. In this way the aforementioned model of the manual transmission ICE vehicle will be transformed into a P0 hybrid vehicle.

The reason for adopting the manual transmission model, even though the assumption made in chapter 5.1. requires an automatic transmission, is that the shifting points, at which the driver model will switch gears, can be explicitly defined for the manual gearbox, effectively having the same effect on the BSG as if a real automatic transmission were used. This decision enabled the P0 MEHV model to be obtained with as little modifications necessary to the CRUISE ™ M example model, thus eliminating possible errors.

This obtained model is shown on figure 79. The stop/start and boosting mode of operation will be tested on given driving cycles, firstly with the rigid coupling between the BSG and ICE and then with the elastic coupling defined by equivalent torsional stiffness and damping coefficients.

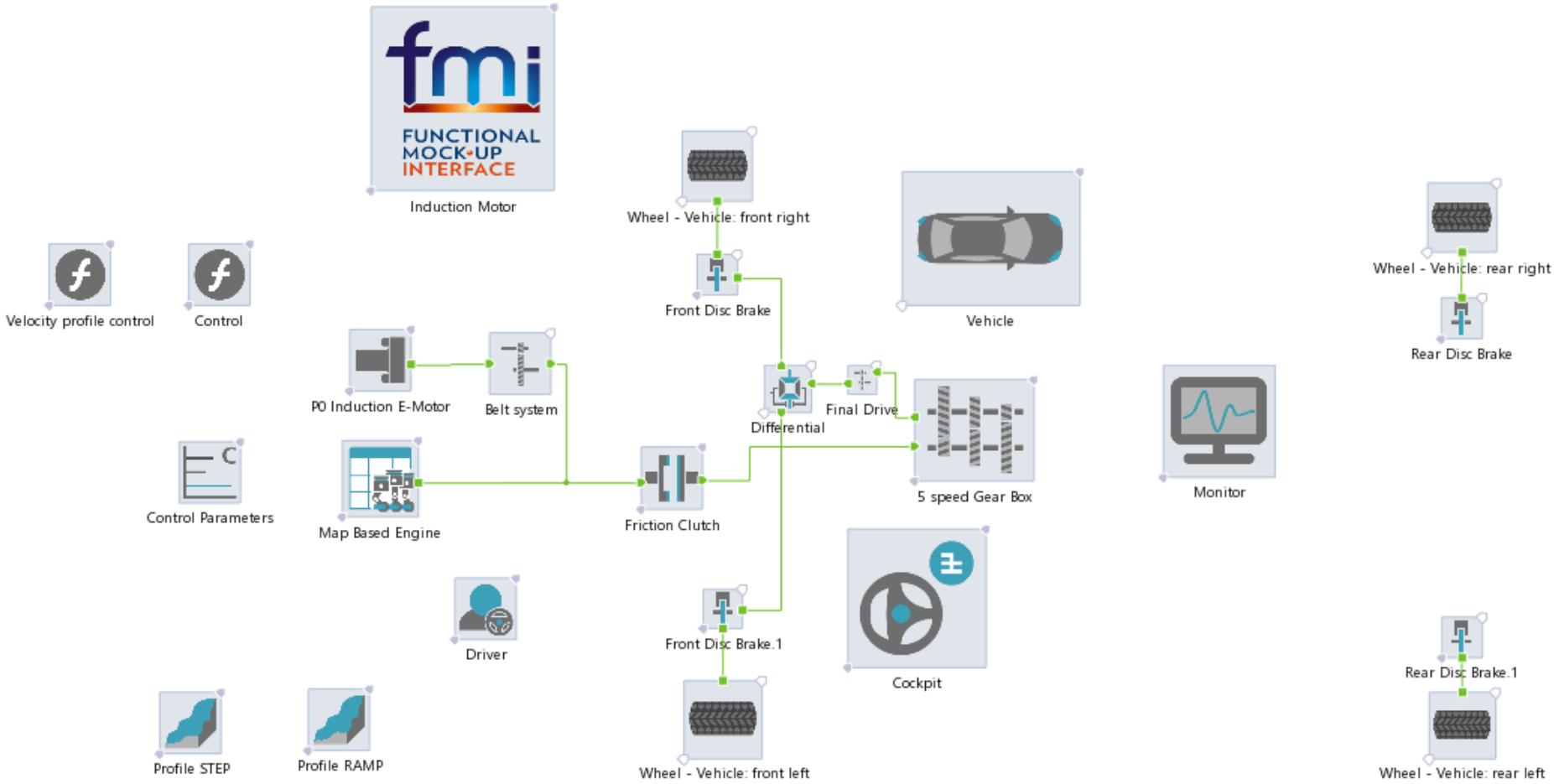


Fig. 79 CRUISE ™ M P0 hybrid vehicle model

7.2. CRUISE ™ M P0 hybrid vehicle model

7.2.1. The vehicle

Figure 79 shows the P0 hybrid vehicle architecture obtained by adding the BSG and control system SIMULINK model compiled as FMU and coupling it with the ICE rigidly through the single ratio transmission named "Belt system". The vehicle component is one of the main objects in the model. It contains parameter data of the vehicle, such as dimensions and weights. The vehicle model needs to somehow be connected to the road and this is done by implementing the wheel model which considers variables influencing the rolling state of the vehicle. In order to brake the vehicle, the brake component is required. It is described by brake data and dimensions and it is possible to opt between drum brakes and disc brakes. The brake model computes the torque considering the braking dimensions and the input brake pressure.

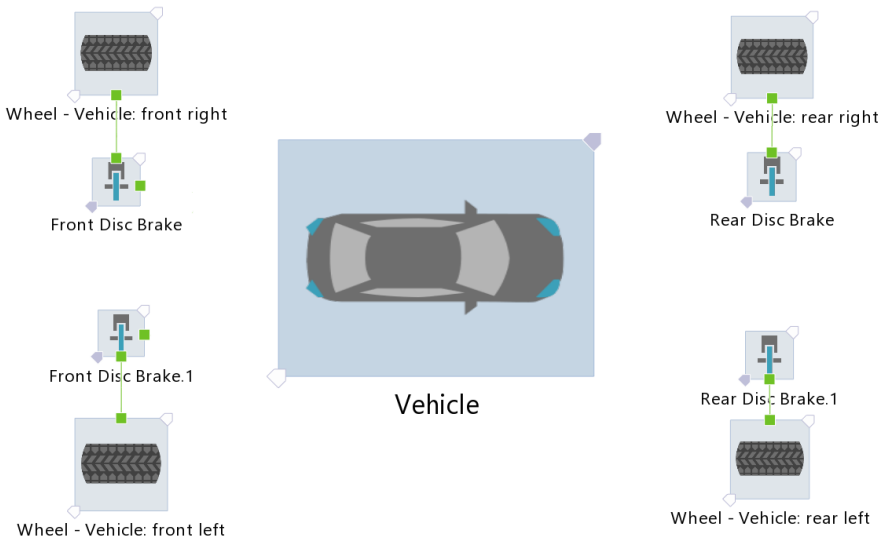


Fig. 80 Vehicle model with brakes and wheels

7.2.2. The driveline

The driveline in this model consists of the map-based ICE, induction motor FMU, flange which outputs the BSG torque generated by the FMU, friction clutch, gear box, belt drive and the differential that is connected to the front wheels.

The map-based ICE simulates the basics of the internal combustion engine. It is essentially a black box that handles maps and characteristic which it interpolates to reproduce the physical behavior of the ICE. Being such, it can only calculate the static torque delivered at

the crankshaft and estimate fuel consumption from available map data. Fuel consumption won't be considered in this simulation.

Induction motor FMU contains the BSG model and its control system from SIMULINK shown on figure 45. The FMU is essentially a function that contains an embedded model made using a third-party software which enables that model to be imported into CRUISE ™ M and ran within a cosimulation, without simultaneously running the third-party software, as opposed to the case of EXCITE ™ cosimulation from chapter 6.

The flange is the energy "output port" of the induction motor FMU, that is the BSG, which outputs its torque to the rest of the model. The flange is connected to the rest of the model via the friction clutch controlled by the driver through the cockpit. The maximum torque of 350 Nm can be transferred by the clutch and it is controlled by the clutch release signal.

The gear box used in this vehicle model is a 5-speed manual gear box with different gear ratios. The efficiency is of each gear is 0.95.

The single ratio transmission block named "Belt drive" represents the FEAD system approximation with only two pulleys, that of the BSG and that of the ICE. It takes no elasticity into account and has an efficiency of 0.97. In order to introduce elasticity into this crude approximation of FEAD, an additional block will be added later on to complement the single ratio transmission. The described driveline is shown on figure 81.

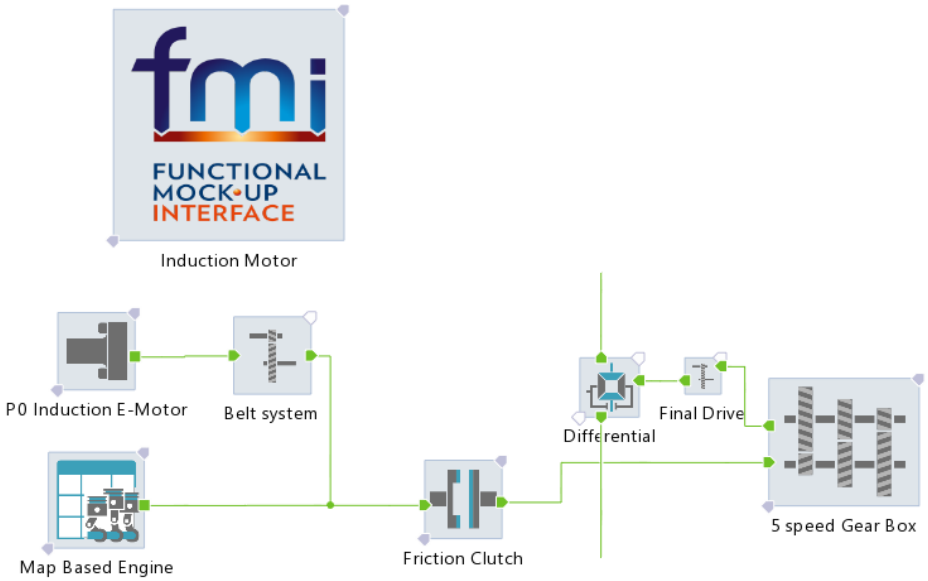


Fig. 81 Driveline model

7.2.3. Driver and cockpit

The driver of the vehicle is a system comprised of two PI controllers equipped with a shifting procedure algorithm. These are the PI velocity controller and PI launching controller. This system is designed to mimic the behavior of an actual driver, and to achieve this, it uses input data that can be categorized into three different groups, each corresponding to a different type of driver behavior:

1) Data defining the driving behavior
2) Data defining the launching behavior
3) Data defining the shifting behavior

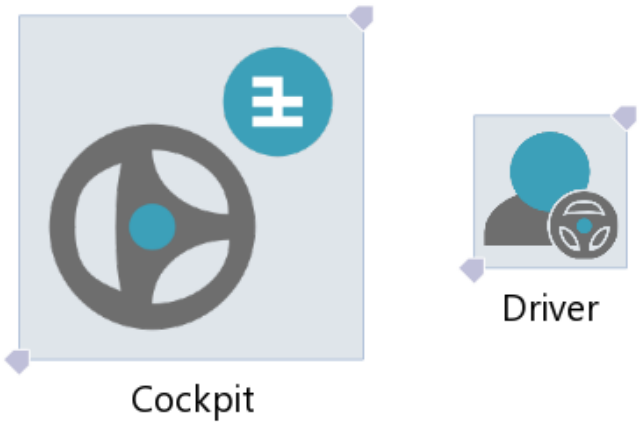


Fig. 82 Cockpit and driver blocks

The cockpit serves as a linkage between the driver and the vehicle. Through the cockpit the driver receives information on desired and current vehicle velocity, which are used by the controllers mentioned previously. The components connected to the cockpit receive through it information considering the accelerator, clutch and brake pedal signals, coming from the driver. In this way, the cockpit serves as a communication medium between the driver and the rest of the vehicle.

This completes a brief description of the CRUISE ™ M manual transmission ICE vehicle model, modified with the induction motor FMU and a rigid single ratio transmission, which together make up a simple model of a P0 hybrid vehicle. Before proceeding to simulation results with the emphasis on stop/start and boosting functionalities, a quick word considering the driving cycles to be simulated is given, along with the scheme of the control logic for start/stop and boosting functions.

7.2.4. Driving regimes

Two driving regimes have been generated for the purpose of testing start/stop and torque boosting functions of the P0 hybrid vehicle modelled in chapter 7.2.3. These regimes are represented by the desired vehicle velocity profile plotted against time, which serves as the referent speed for the driver.

The first regime has been designed to emphasize the response of the BSG in the boosting mode of operation by using the step change of the desired vehicle velocity signal. This will provoke the control system to request the maximum torque output from the BSG in order to accelerate the vehicle. In this regime the start/stop function is performed only once since desired vehicle velocity profile doesn't repeat itself, i.e. it is not cyclic.

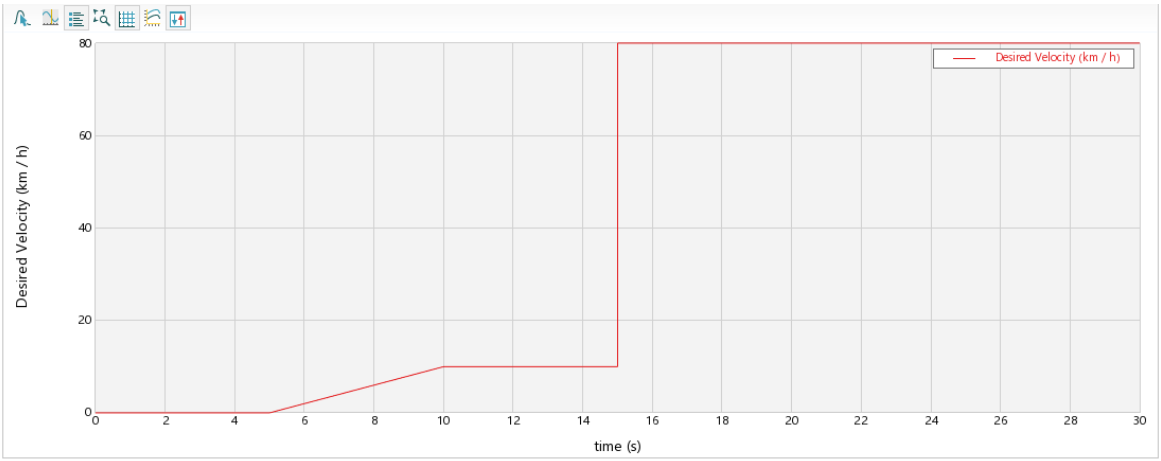


Fig. 83 Driving regime #1

The second regime has a character of a real driving cycle since the vehicle velocity profile repeats itself. This regime provokes the boosting mode of operation several times, however this time by means of ramp desired velocity change. The star/stop function is preformed several times since the vehicle is brought to a halt repeatedly.

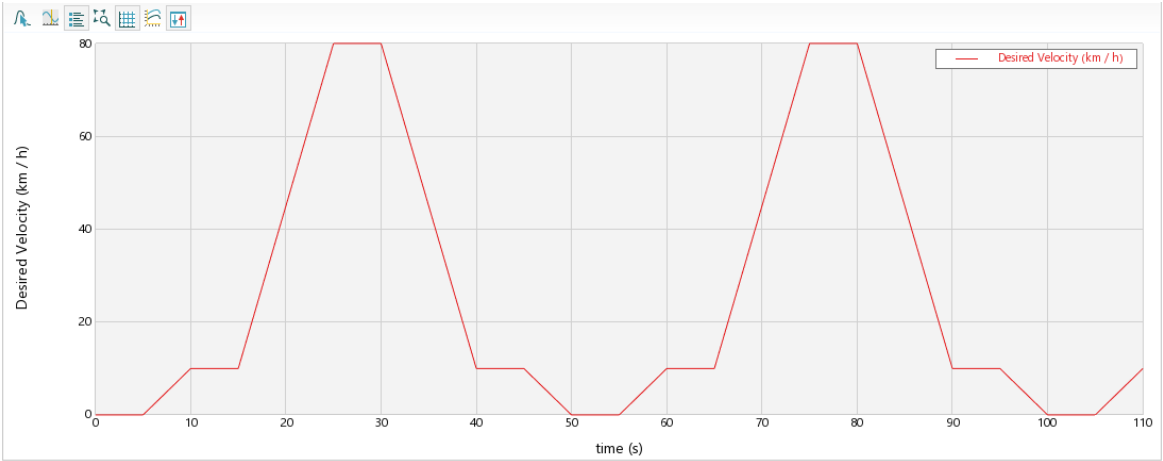


Fig. 84 Driving regime #2

7.2.5. Stop/start and boost control logic

The stop/start and boost control logic is implemented in CRUISE ™ M as a separate control function block, which regulates the aforementioned operation modes of the vehicle. This control function takes inputs from CRUISE ™ M components, such as the cockpit block (load signal, clutch release signal) or the map-based engine block (ICE speed), which are then run through the statements presented on the flowchart in figure 85 in order to check if the required conditions for start-up or torque boosting of the vehicle by the BSG have been met. The control function block evaluates its inputs against the IF statements in figure 85 once per timestep, which therefore makes that function a FOR loop with the number of iterations being equal to the number of timesteps in the simulation.

The legend at the top left part of the figure 85 provides the definition of every input and every output of the control function, as well as instructions on how to read the flowchart. The flowchart is divided into four control sections which are connected in series with respect to one another: "STOP/START CONTROL", "ICE SWITCH CONTROL", "BSG SPEED CONTROL" and "BOOST REQUEST CONTROL". Brief explanation of those sections is given below.

"STOP/START CONTROL" - switches the start/stop bit (SS) bit ON or OFF depending on the current conditions of the vehicle and sets the BSG referent speed, which is then proceeded to the BSG in the FMU.

"ICE SWITCH CONTROL" - section switches the map-based engine torque output ON or OFF depending on the ICE speed and the state of the SS.

"BSG SPEED CONTROL" - section shuts down the BSG speed control system in the FMU after certain conditions have been met, so that it doesn't interfere with the commands of the driver.

"BOOST REQUEST CONTROL" - section commands the FMU to output the maximum torque when the conditions for it have been met.

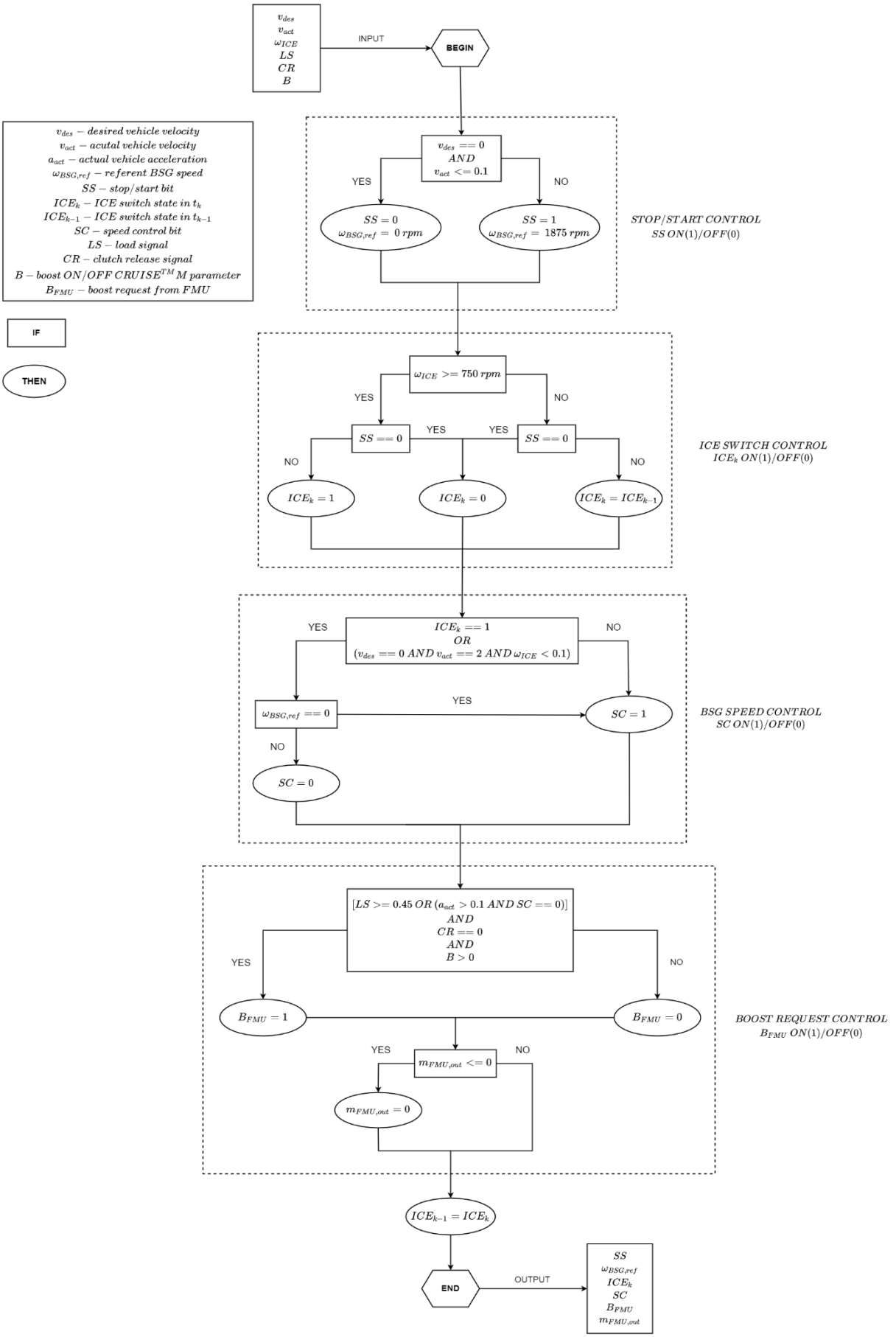


Fig. 85 Stop/start and boost control logic in CRUISE™ M

7.2.6. CRUISE ™ M simulation results

7.2.6.1. Driving regime #1 simulation results

The simulation results of the P0 hybrid vehicle model described in the previous chapters, for the case of desired vehicle velocity profile according to driving regime #1, are presented on figure 86.

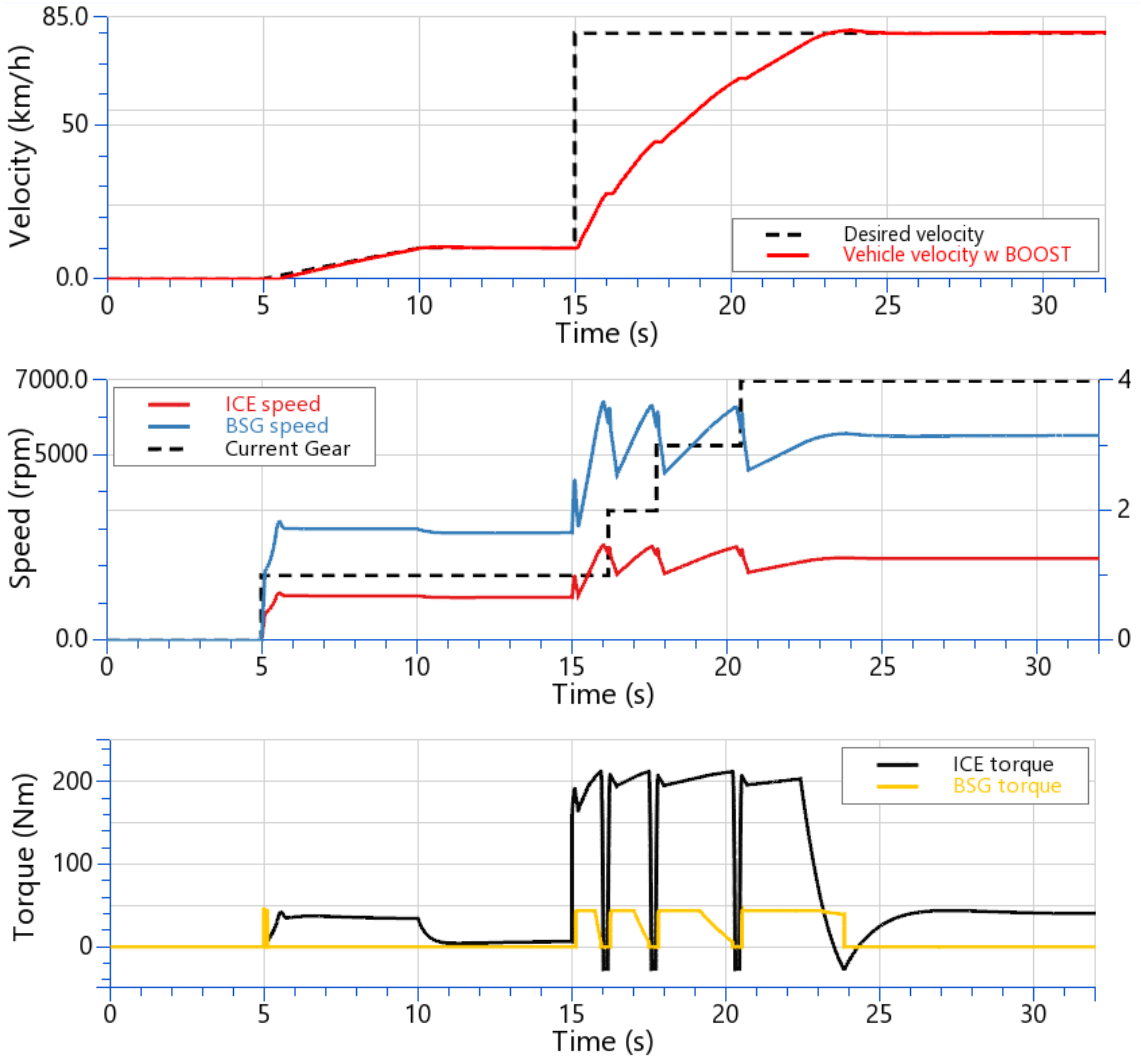


Fig. 86 Driving regime #1 simulation results

In order to analyze the simulation results of the whole driving regime #1, shown on figure 86, the detail views of those results are presented on the following figures, to give better insight into stop/start and boosting functions performed. Considering this, figure 87 presents vehicle velocity, BSG and ICE speed and torque responses in a timeframe during which start-up of the engine occurs.

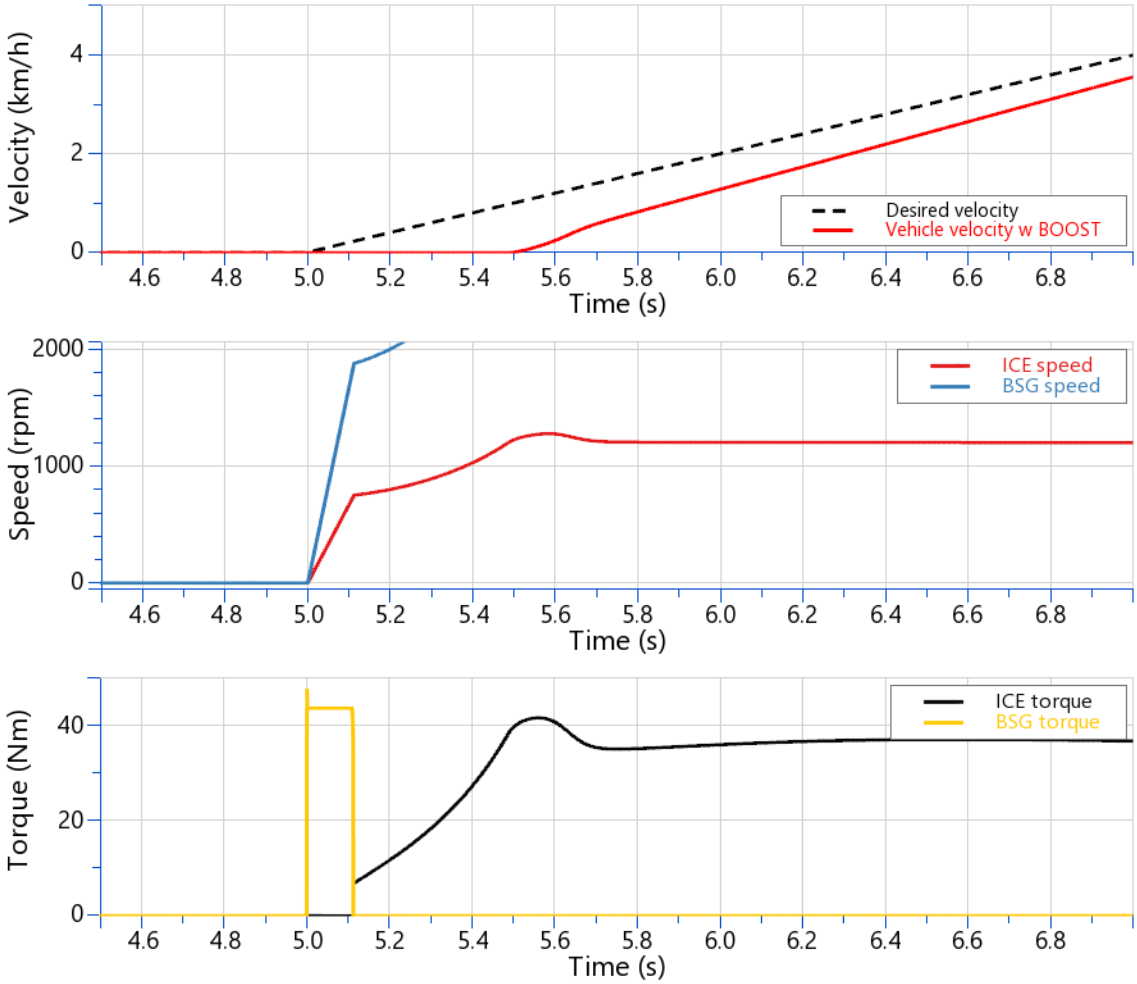


Fig. 87 Detailed view of Driving regime #1 simulation results emphasizing stop/start function

From figure 87 can be observed that stop/start function of the BSG is working properly, since the ICE starts outputting torque only after it has been run-up to a speed of 750 rpm, which is the speed set as the point at which the control system switches the ICE from OFF to ON, as indicated by the control logic scheme on figure 85. Since the coupling between BSG and ICE defined by the single ratio transmission block, which is placed there instead of the FEAD, is rigid, there are no transient oscillations in their speed responses that would be caused by the elasticity of the drive, which means that the ICE speed response follows without any lagging the speed response of the BSG, with the transmission ratio naturally taken into account.

To emphasize the boosting function, figure 88 presents vehicle velocity, BSG and ICE speed and torque responses in a timeframe during which torque boosting of the engine by the BSG occurs.

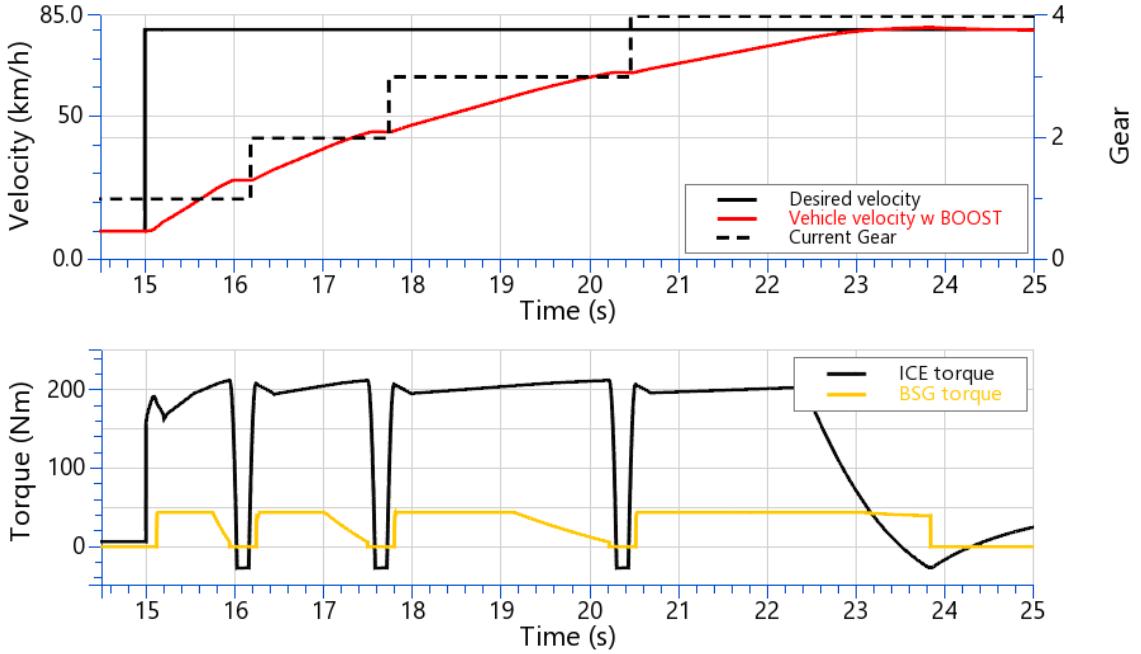


Fig. 88 Detailed view of Driving regime #1 simulation results emphasizing boosting function

The boosting mode of operation is cyclic for BSG, depending on the request from the driver and other conditions described in the control logic scheme from figure 85. From figure 88 can be observed that once the vehicle velocity grows above a certain value during acceleration, the BSG torque starts to decrease. This is due to the electromagnetic occurrences in the BSG dependent on its speed, which is directly related to the vehicle velocity since BSG is rigidly coupled with the ICE crankshaft via the singe ratio transmission block approximating the FEAD. This relation between BSG speed and its torque is illustrated on the upper diagram on figure 89.

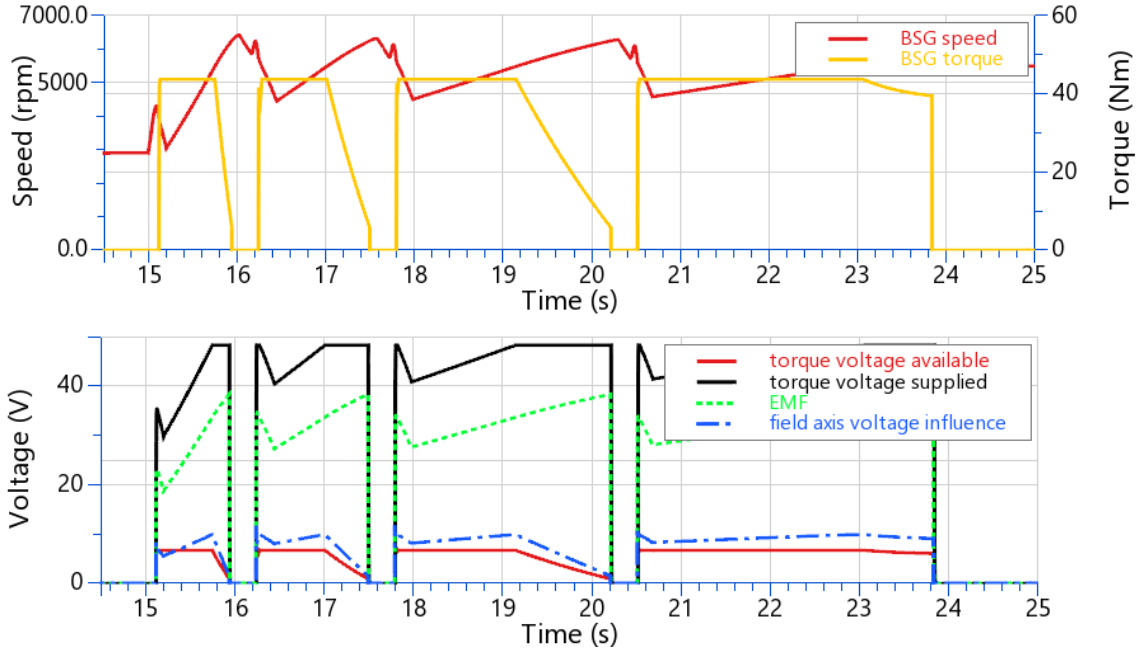


Fig. 89 BSG torque and speed response, along with its electromagnetic response during boosting periods

The lower diagram on figure 89 clarifies why the BSG torque starts to decrease after a certain speed is reached. Namely, it has to do with the equation governing the voltage of the virtual q coil, that is, the torque coil, of the induction machine given in chapter 4.3.4. which is repeated here:

$$u_{sq} + \Delta u_{sq} = R_q i_{sq} + L_q \frac{di_{sq}}{dt}, \tag{7.1}$$

$$u_{sq} - \left(\omega_{mr} \frac{L_m^2}{L_r} i_{mr} + \omega_{mr} \sigma L_s i_{sd} \right) = R_q i_{sq} + L_q \frac{di_{sq}}{dt}. \tag{7.2}$$

After decomposing the left side of equation *(7.2)* the picture becomes clear:

$$\underbrace{\underbrace{u_{sq}}_{\text{torque voltage available}} - \left(\underbrace{\omega_{mr} \frac{L_m^2}{L_r} i_{mr}}_{\text{EMF}} + \underbrace{\omega_{mr} \sigma L_s i_{sd}}_{\text{field axis voltage influence}} \right)}_{\text{torque voltage supplied}} = R_q i_{sq} + L_q \frac{di_{sq}}{dt}$$

From the above decomposition it is seen that the torque voltage supplied has to overcome both the EMF and the field axis influence in order to have some voltage available for generation of the positive torque current i_{sq}, that is, the current governing the torque response of the machine. Since the EMF and field axis voltage influence are both functions of BSG speed, their increase is inevitable as the vehicle gains velocity. The control system has information about this increase and responds by supplying higher voltage, that is, until it hits the limit of 48 V, since this is a 48V MHEV. Due to this voltage limit, the machine torque starts to decrease because the vehicle is still accelerating, that is, the BSG speed is still rising. This problem is resolved by shifting the gear when a certain BSG speed is reached, which brings its speed back down and enables the maximum accelerating torque to be outputted once again from the machine. It is important to note that the selection of speeds at which the gears are shifted is a compromise between obtaining the maximum torque output of the ICE or that of the BSG. In the scope of this simulation it has been decided that the choice shifting speed will be inclined towards obtaining the maximum torque output of the BSG since the total torque output of the system, that is, combined output of the ICE and BSG, is greater in this case than in would be if the shifting procedure were optimized according to the speed/torque characteristic of the ICE.

Before proceeding to the next chapter, the difference in the vehicle velocity and the total system torque response is presented for the case of boosting function being disabled. The aforementioned can be observed on figure 90.

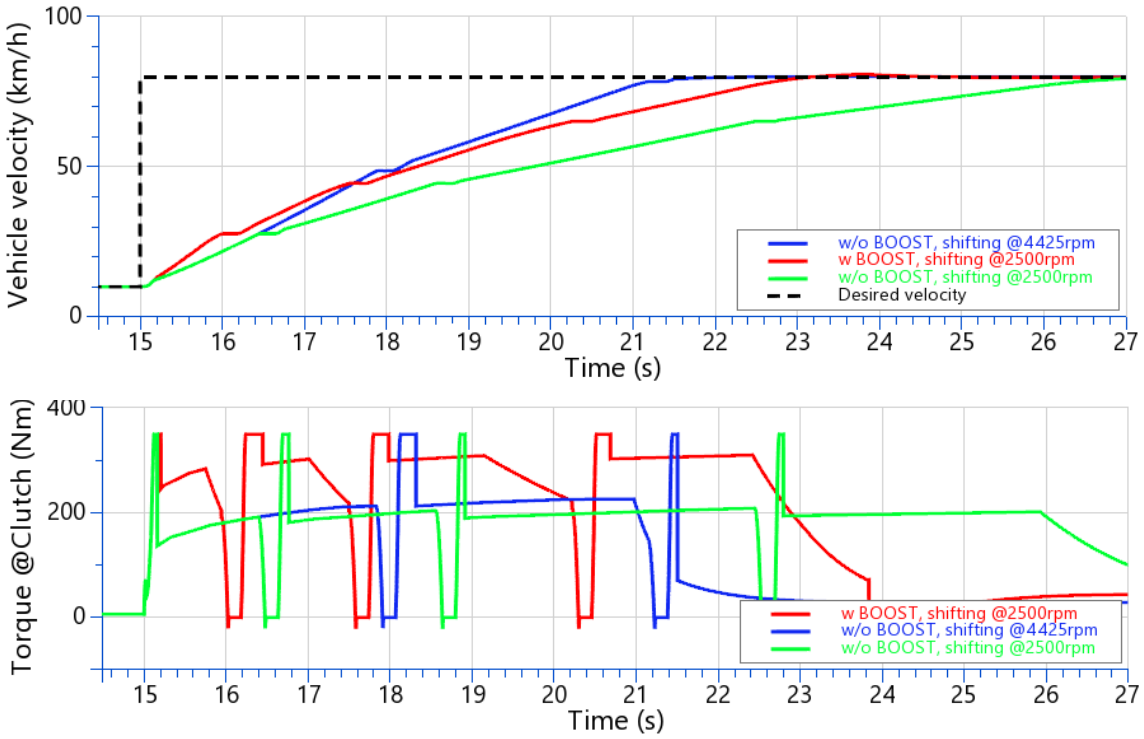


Fig. 90 Comparison of vehicle velocity and total torque at clutch for the cases with and without boosting

From figure 90 can be observed that the vehicle accelerates faster when the boosting function is enabled, that is, when both the BSG and ICE provide torque, as opposed to the case when the ICE is accelerating the vehicle by itself, with gear shifting point being set at 2500 rpm. However, this is a suboptimal gear shifting point for the ICE, chosen as a compromise for a joint operation mode between ICE and BSG, that is for the boosting regime. To get a better picture of the performance of the system when it is driven by ICE alone, the gear shifting point is set to 4425 rpm, which is the point of ICE maximum torque. When gear shifting is tuned this way, it is shown that the case without ICE boosting outperforms the case when the ICE is boosted by the BSG. This better performance is only in respect to vehicle acceleration, without considering fuel economy since that is out of the scope of this thesis.

This concludes the analysis of the stop/start and boosting function of the CRUISE ™ M P0 hybrid vehicle model from figure 79 for the case of desired velocity profile defined by driving regime #1. In the next chapter the performance of the same model is presented on cyclic desired velocity profile defined by driving regime #2, where stop/start and torque boosting is performed multiple times. The objective of this driving regime was to show that the start/stop and boosting functions work robustly on multiple provocations from the driver, as he tries to follow the desired velocity profile.

7.2.6.2. Driving regime #2 simulation results

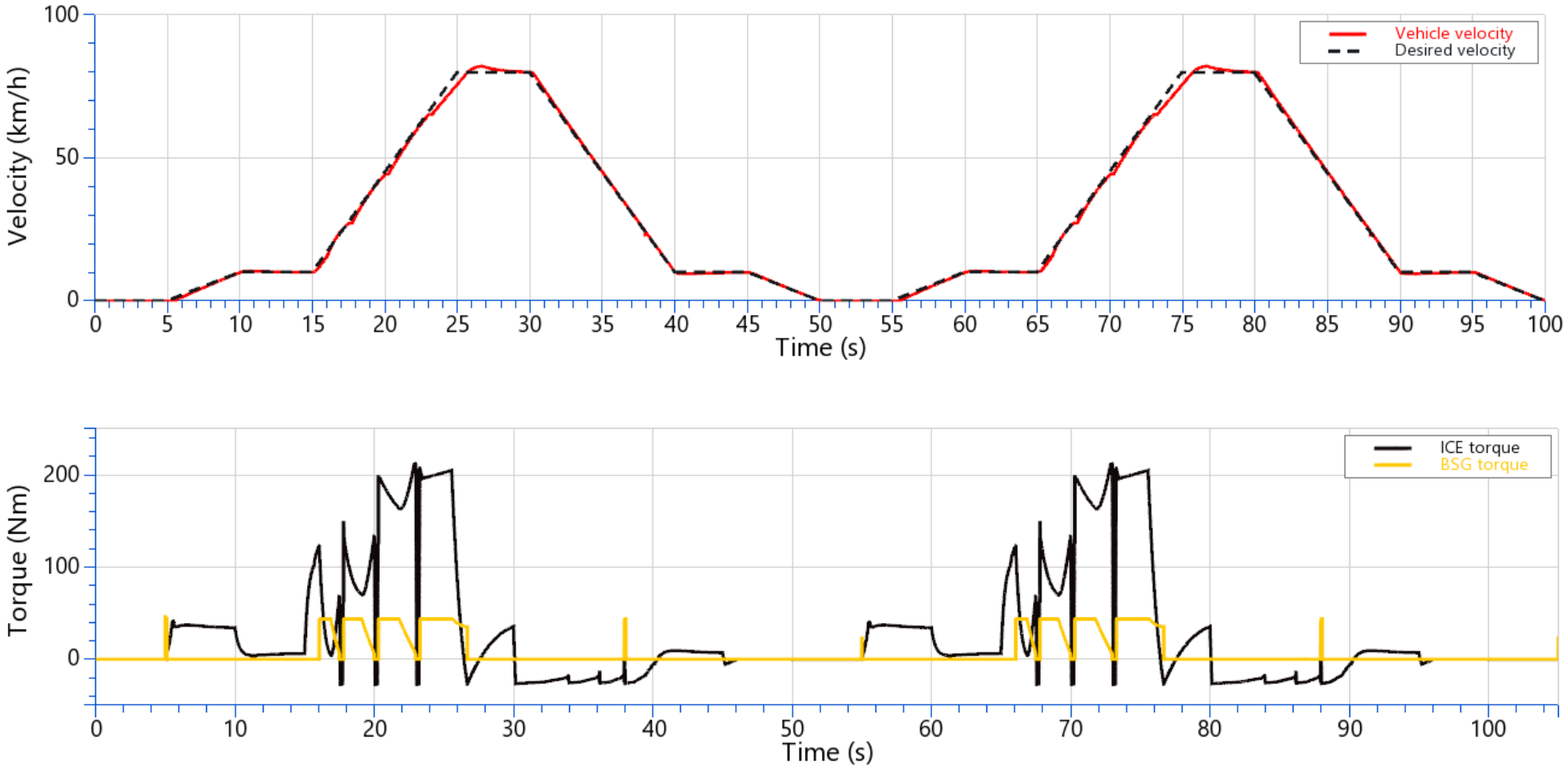


Fig. 91 Driving regime #2 simulation results

Simulation results from figure 91 show that the start/stop and boosting systems provide stable outputs when provoked multiple times. The detailed analysis of the simulation results for driving regime #2 won't be performed since it would lead to repeating the conclusions made in chapter 7.2.6.1.

Finally, the objective of next chapter is to make the coupling between the ICE and BSG elastic in order to capture transient oscillations that are present in the real physical system. This will be done in the next chapter by modifying the single ratio transmission currently coupling them rigidly by adding an additional element in the model.

7.3. CRUISE™ M P0 hybrid vehicle model with elastic coupling between the BSG and the ICE

The elastic coupling is introduced into the system model by adding a shaft element into the driveline as shown on figure 92. The elastic behavior of the shaft element is defined by the equivalent torsional stiffness and damping calculated from EXCITE ™ Timing Drive data as indicated by equations *(5.43)*, *(5.44)*, *(6.1)* and *(6.2)*.

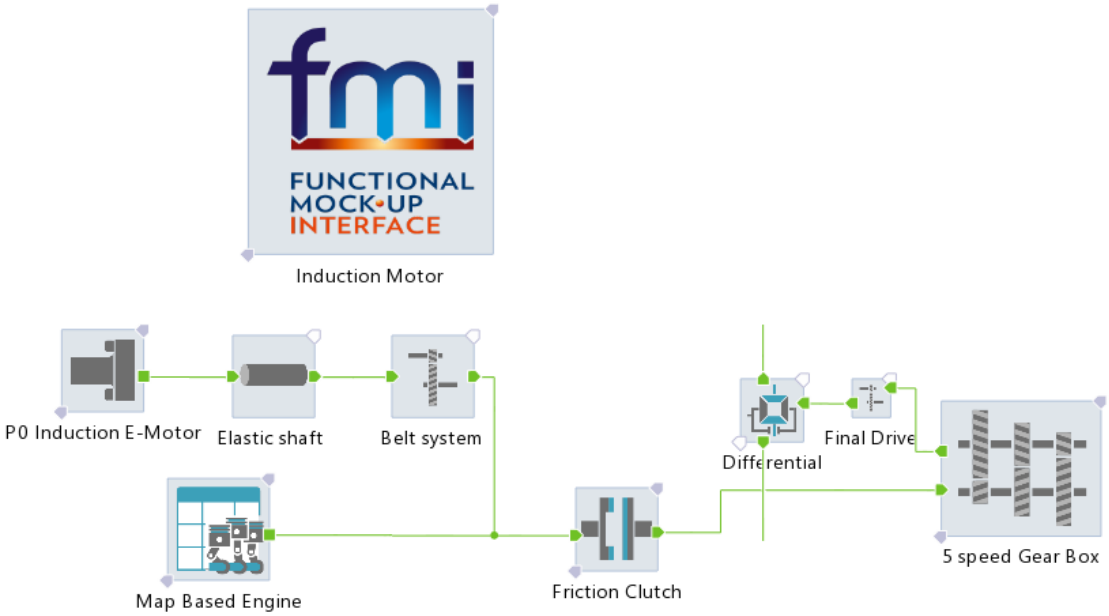


Fig. 92 Driveline model extended with an elastic shaft

The results of the system simulation with the driveline from figure 92 are shown on figure 93. The vibrations in BSG speed are now present in the transient response during the start-up mode of operation. It is observable from figure 93 that the control system damps the BSG speed

oscillations relatively fast, namely within 0.1 seconds after they start occurring. After that, the BSG speed continues to steadily approach the start-up point at which the torque supplied by the BSG is cut-off. At that time the ICE is "turned-on" and starts outputting torque which continues to accelerate the system. Since the torque of the ICE is not governed by a control system tuned to damp the vibrations of the elastic accessory drive, but by the driver sending torque demand signals by "pressing" the acceleration pedal, the system starts to oscillate.

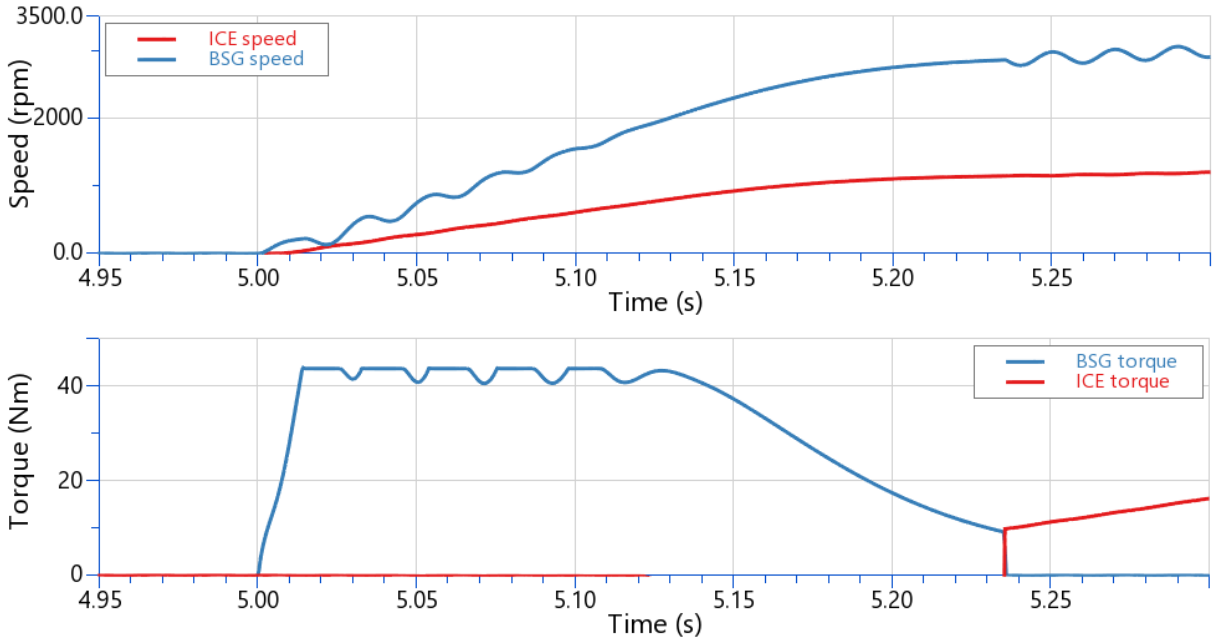


Fig. 93 BSG and ICE speeds and torques during start-up period with the elasticity of the belt included in the driveline model

The vehicle velocity response on a desired velocity profile according to driving regime #1 can be observed on figure 94, along with the BSG and ICE torque responses indicating that the vehicle is being boosted successfully when the driveline is elastic. However, if the speed responses of the BSG and ICE are observed on figure 95, it is noticeable that the BSG speed response is somewhat oscillatory in the boosting region and especially oscillatory after the desired velocity of the vehicle is reached. It is important to note that these oscillations occur in simulation periods during which the control system for mitigation of FEAD vibrations designed in chapter 5 is turned off, firstly for the sake of boosting, when the BSG has to output its maximum torque and secondly after the boosting period is finished and desired velocity reached, since there are no events that would trigger the control logic from figure 85 to turn the control system on again.

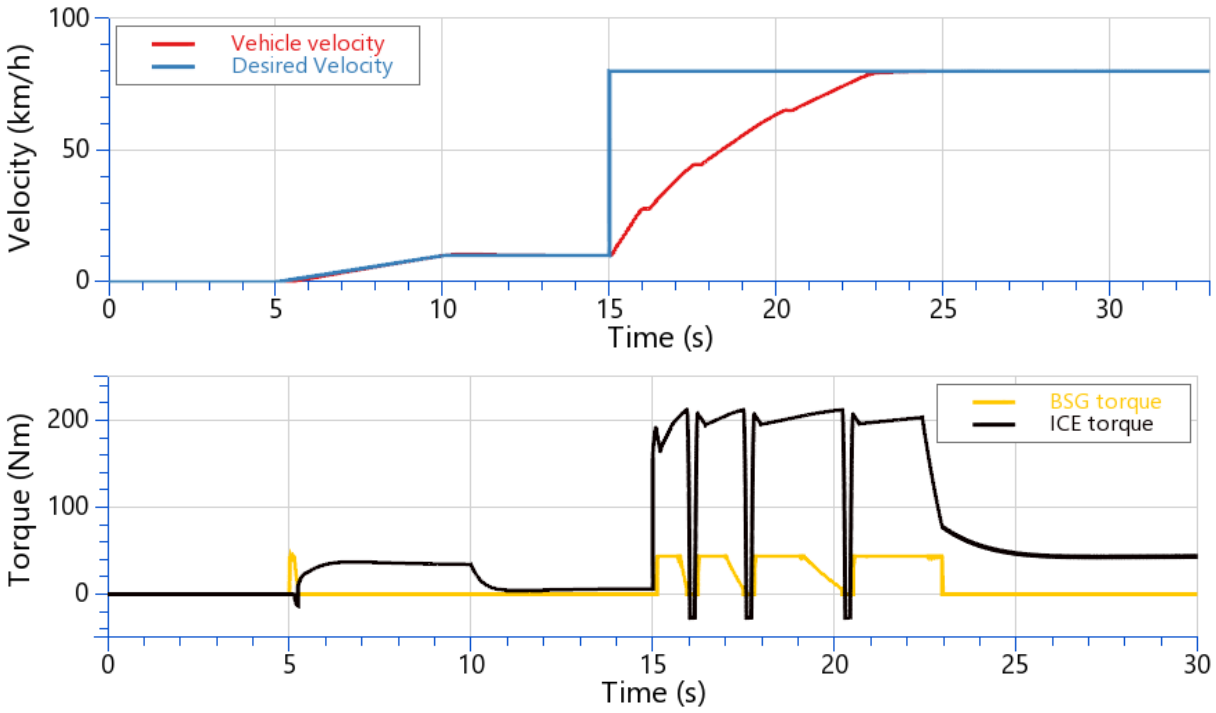


Fig. 94 Vehicle velocity, BSG and ICE torque responses on driving regime #1 desired velocity change, with the driveline of the system being elastic

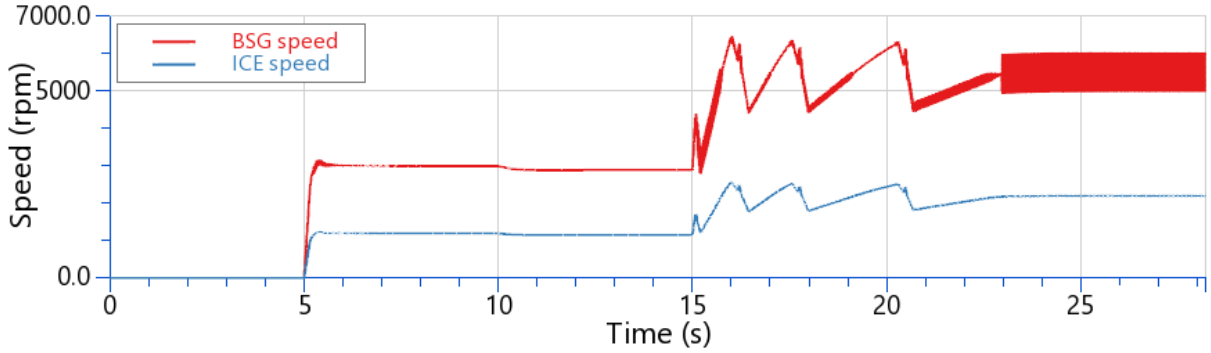


Fig. 95 BSG and ICE speed responses on driving regime #1 desired velocity change, with the driveline of the system being elastic

These high amplitude-high frequency BSG speed oscillations in the period after the desired velocity of the vehicle is reached ($t_{simulation} > 23\ s$) occur due to the oscillations in ICE torque, which are being transferred to the BSG through the elastic shaft. The ICE torque oscillates in the first place because of the attempts of the driver to maintain the desired velocity by sending high frequency load demand signals to the ICE in order to compensate for the shaft torque. This is the equivalent of the driver pressing and releasing the gas pedal with a frequency observed on figure 96.

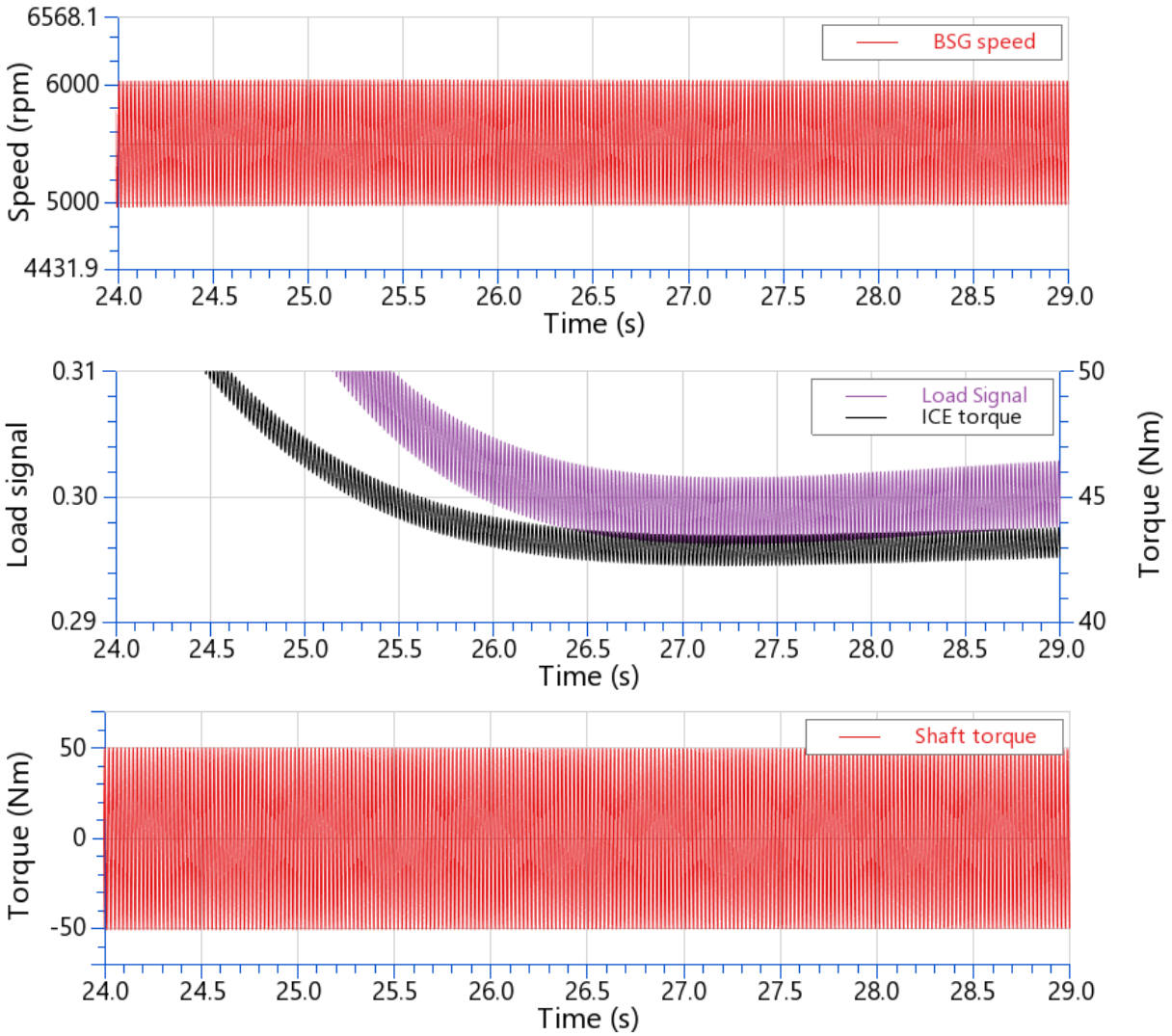


Fig. 96 Detail views of BSG speed response, driver load signal, ICE torque and shaft torque

Since this kind of compensation is impossible in reality, another strategy needs to be adopted. The idea is to use the BSG torque to compensate for the shaft torque during the period after which the desired velocity of the vehicle is reached, that is after $t_{simulation} = 23\ s$. In this period the BSG supplies torque for a few seconds until the oscillations in its speed are sufficiently damped. In another words, the BSG is used as a compensator which supplies torque equal to the shaft torque, but of opposite direction. The limitation of this compensator is the maximum amount of torque which it can supply. The meaning of this is that the speed oscillations will be damped during a relatively longer time interval if the shaft torque is higher than the maximum torque output of the BSG when compared to the time interval that would be required for their damping if the BSG wasn't limited by its maximum torque. The BSG speed response, along with the ICE and BSG torque responses after turning on the compensator are

shown on figure 97. When the detail view of the driver load signal, ICE torque and shaft torque responses is observer on figure 98, it can be noticed that the driver no longer tries to compensate for the shaft torque by sending high frequency load signals to the ICE, since the shaft torque shown on the same figure is compensated by the BSG torque.

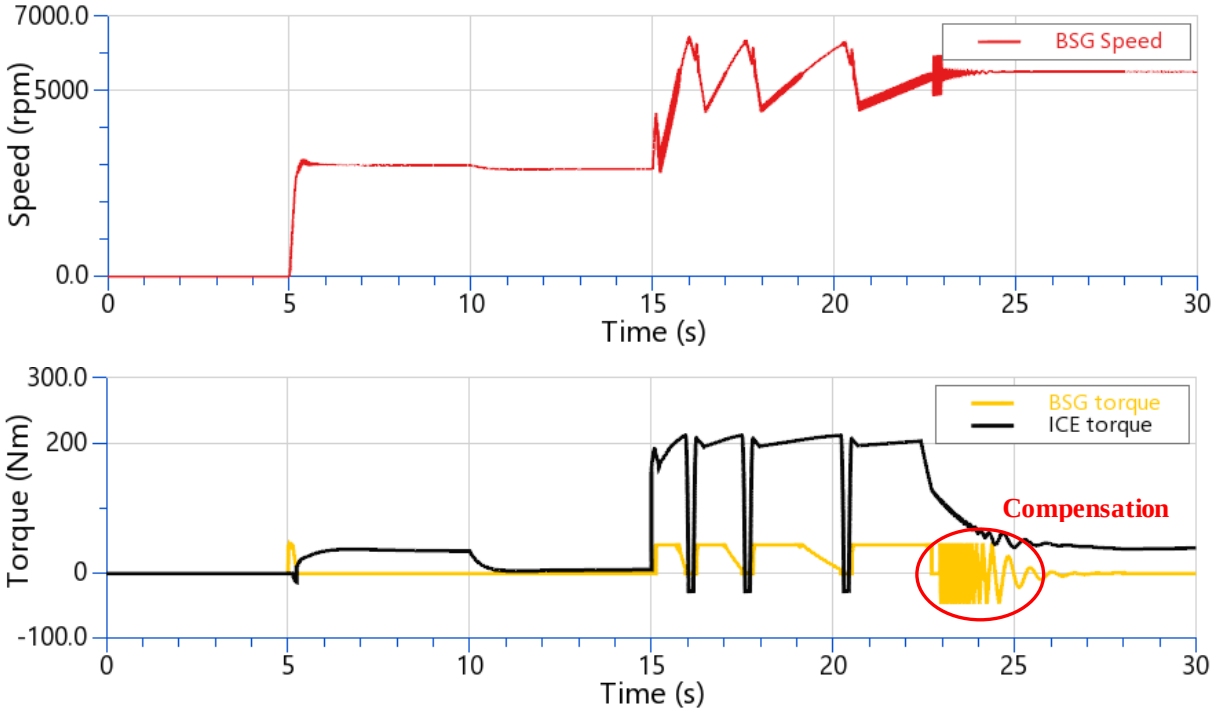


Fig. 97 BSG speed, BSG torque and ICE torque responses with compensation of shaft torque by the BSG

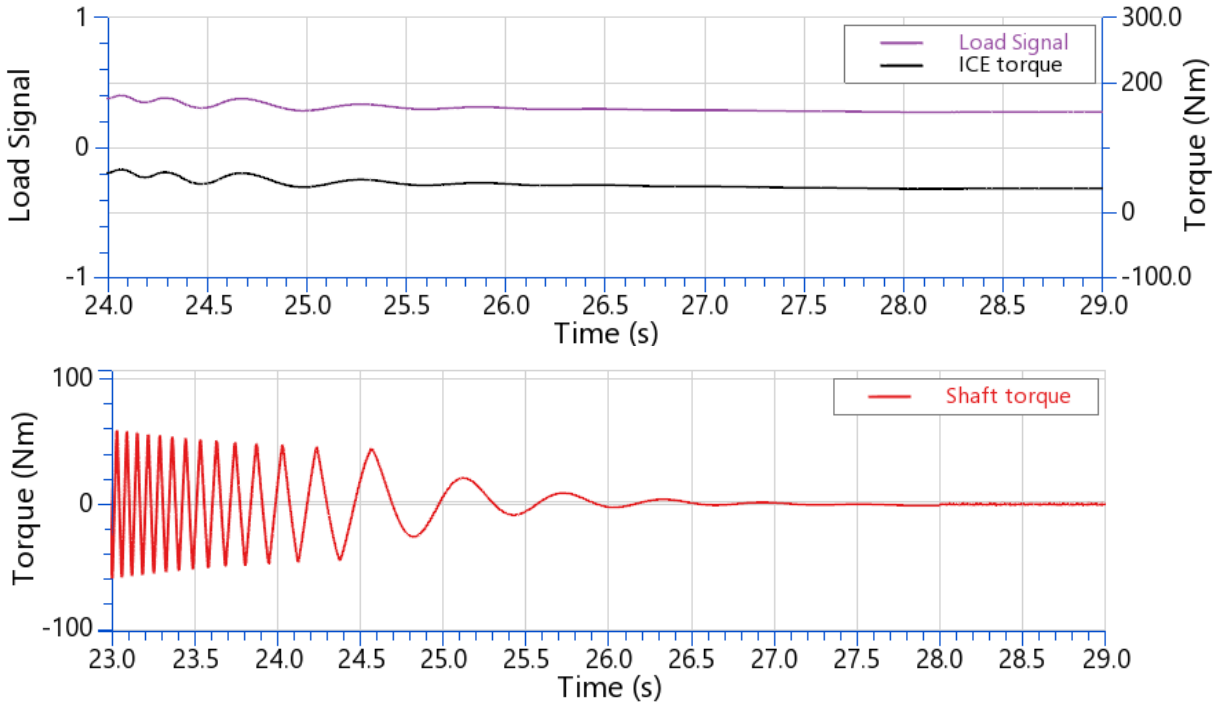


Fig. 98 Detail view of the driver load signal, ICE torque and shaft torque responses

To finish things off, since three different simulation environments, MATLAB, EXCITE ™ Timing Drive and CRUISE ™ M, have been used to simulate the run-up of the ICE crankshaft by the BSG, the speed responses of this run-up made in the three aforementioned software are plotted against one another on figure 99.

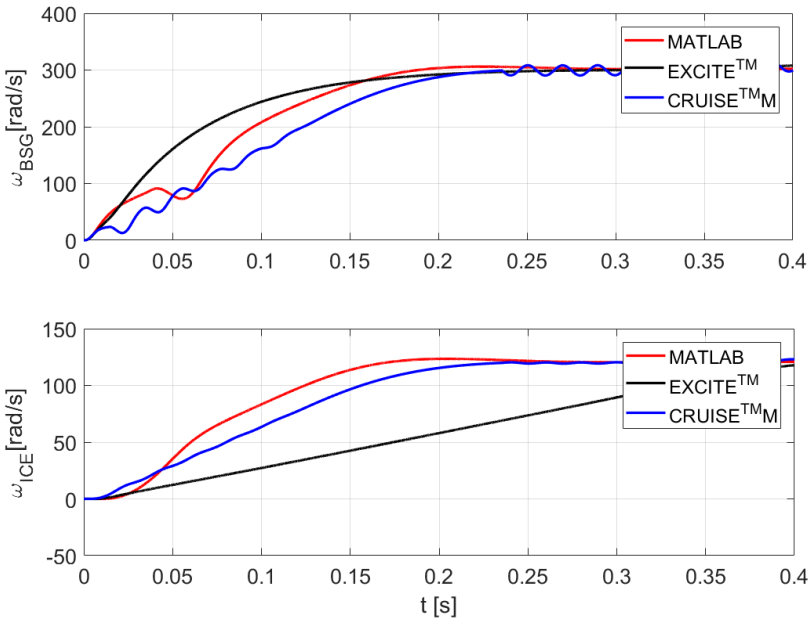


Fig. 99 Speed response comparison of BSG and ICE during run-up in three different simulation environments

8. CONCLUSION

The goal of this thesis was to derive the mathematical model of a 48 V asynchronous belt starter-generator suitable for vector control and to design its speed control system with the emphasis on the mitigation of timing belt vibrations. The performance of the derived BSG model and its control system was to be tested on micro level in EXCITE ™ Timing Drive, a multi-body dynamics simulation environment specialized for powertrain analysis, and on the macro level in CRUISE ™ M, a simulation environment specialized for multi-disciplinary system simulations.

After a brief introduction concerning the effects that the ever increasingly stricter requirements on exhaust gas emissions are having on the automobile industry, the 48 V MHEV is presented as a practical solution for car manufacturers. It has been explained that the utilization of the 48 V architecture maximizes the total power of the MEHV without additional costs associated with safety regulations that have to be minded when using a voltage over 60 V.

Following this, the mathematical model of a BSG, with the assumption that it is a squirrel-cage machine, is derived in its natural 3-phase stationary coordinate system. Next, vector control is introduced as a method that enables independent control of the magnetic flux and torque of the BSG, which in turn enables linear control methods to be used, analogous to the case of the DC machine. Clarke and Park transformations were used to transform the BSG model from the 3-phase stationary coordinate system into the rotating orthogonal $d-q$ system. After assuming the voltage-source inverter is used to supply the machine, further modifications were made to the mathematical model, finally yielding its form favorable for the application of linear control methods.

Next, the two-mass simplification of the FEAD longitudinal dynamics was derived and its equivalent torsional form was obtained. The synthesis of the cascade BSG speed-current control system has been performed by means of closed-loop system pole placement methodology according to the damping optimum criterion, yielding a system tuning favorable for the mitigation of timing belt vibrations. Simulation results from MATLAB indicated that

this control system tuning, which takes into account the elasticity of the drive, indeed shows a good performance when coupled with the two-mass simplification of FEAD.

In order to test the performance of the system on a more precise model of the accessory drive, the cosimulation between MATLAB and EXCITE ™ Timing Drive has been performed, within which the FEAD system was in EXCITE ™ and the BSG/control system in MATLAB. The cosimulation results have shown that the slippage phenomenon, the dynamics of which the two-mass simplification of FEAD does not capture, had a profound effect on system performance. The slippage hinders torque transfer from BSG to ICE, which means that the torque for accelerating the ICE crankshaft is build up considerably slower when compared to its equivalent in MATLAB, within which the slippage isn't modelled. The consequence of this was that the ICE, within the EXCITE ™/MATLAB cosimulation, reached its nominal speed roughly 0.2 seconds later than in the MATLAB simulation, yielding a total of about 0.4 seconds run-up time to 1145 rpm.

Following this, the CRUISE ™ M system simulation environment was used to integrate the induction motor and control system model from SIMULINK, compiled as an FMU, into an ICE vehicle architecture, thus transforming it in to a P0 MHEV, within which the BSG and the ICE are coupled rigidly. The system simulations of two different driving regimes have indicated that the BSG can perform stop/start and torque boosting functions on demand and have clearly outlined the limitation of the 48 V system when it comes to high-speed performance, along with the need for an optimal design of the gear shifting strategy in respect to the BSG speed/torque curve. Finally, the elasticity of the FEAD was introduced into the CRUISE ™ M model, which yielded the results of start-up part of the driving cycle similar to those from MATLAB and EXICTE ™ shown previously. The boosting part of the simulation showed oscillations of BSG speed, which were expected considering that the boosting regime requires the control system tuned for vibrations damping to be turned off, and instead the maximum available torque of the BSG must be outputted. It has been shown that the compensation of the shaft torque by the BSG is needed for a few seconds after the vehicle reached its desired speed of 80 km/h in order to damp the high frequency-high amplitude oscillations in BSG speed.

The future work along the lines of this master's thesis could include the following areas:

- Implementation of the generating mode of operation for the induction machine
- Modelling of the power supply with the dynamic model of the battery
- Performing the test of the control system on a virtual testbed
- Hardware-in-the loop simulation

Bibliography

[1] European Comission, "A European Strategy for low-emission mobility," [Online]. Available: https://ec.europa.eu/clima/policies/transport_en#tab-0-0. [Accessed 5 March 2020].

[2] European Comisssion, "Reducing CO" emissions from passenger cars - before 2020," [Online]. Available: https://ec.europa.eu/clima/policies/transport/vehicles/cars_en. [Accessed 5 March 2020].

[3] The International Council on Clean Transportation, "European Vehicle Market Statistics," 2018. [Online]. Available: https://theicct.org/sites/default/files/publications /ICCT_Pocketbook_2018_Final_20181205.pdf. [Accessed 6 March 2020].

[4] P. Els, "What electric vehicle and electrification strategies are available to manufacturers," 10 February 2020. [Online]. Available: https://www.automotive-iq .c om/electrics-electronics/articles/automotive-iq-guides-electric-vehicles. [Accessed 5 March 2020].

[5] x - engineer, "Understanding micro, mild, full and plug-in hybrid electric vehicles," [Online]. Available: https://x-engineer.org/automotive-engineering/vehicle/hybrid/ micro-mild-full-hybrid-electric-vehicle/. [Accessed 5 March 2020].

[6] W. Schöffmann, H. Sorger, A. Ennemosser, C. Priestner, M. Hütter and B. Klarin, "The impact of 48V to friction and efficiency optimization of the base engine - Approach for quantification in future driving cycles," in *5. ATZ - Fachtagung "Reibungsminimierung im Antriebsstrang"*, Esslineg am Neckar, Germany, 2016.

[7] Continental AG, "Low Voltage, High Performance: Full-Hybrid Vehicle with 48-Volt High-Power Techology," 2 July 2019. [Online]. Available: https://www.continental .co m/en/press/press-releases/2019-07-02-48v-high-power-176 814 . [Accessed 5 March 2020].

[8] B. Klein and O. Maiwald, "48 Volt Technology For more efficiency and fun to drive," *Die Bibliothek der Technik,* vol. 388, p. 74, 2016.

[9] C. Schröder and A. Stuffer, "P0 Mild Hybrid With System Competence to Maximum Efficiency," in *Schaeffler Symposium 2018 - Mobility for Tomorrow,* Baden-Baden, Germany, 2018.

[10] M. Jadrić and B. Frančić, Dinamika električnih strojeva, Zagreb: Graphis Zagreb - Udžbenici Sveučilišta u Splitu (Manualina Universitatis studiorum Spaletensis), 2004.

[11] B. Skalicki and J. Grilec, Električni strojevi i pogoni, Zagreb: Fakultet strojarstva i brodogradnje, Sveučilište u Zagrebu, 2011.

[12] J. Liu, Modeling, Analysis and Design of Integrated Starter Generator System Based on Field Oriented Controlled Induction Machines, Doctoral disertation, The Ohio State University, 2005.

[13] G.-H. Lee, G.-S. Choi and W. Choi, "Design Considerations for Low Voltage Claw Pole Type Integrated Starter Generator (ISG) Systems," *Journal of Power Electronics,* pp. 527-532, 2011.

[14] M. Wardach, "Hybrid excited claw pole generator with skewed and non-skewed permanent magnets," *Open Physics,* vol. 15, no. 1, pp. 902-906, 2017.

[15] D. Sumina and I. Šandor, "Matematički model asinkronog stroja prilagođen vektorskom upravljanju," Fakultet elektrotehnike i računarstva, Sveučilište u Zagrebu, Zagreb, 2018.

[16] J. Rodriguez and P. Cortes, Predictive control of power converters and electrical drives, Chicester, United Kingdom: John Wiley & Sons, 2012.

[17] M.-F. Rahman, D. Patterson, A. Cheok and R. Betz, "Motor Drives," in *Power Electronics Handbook,* Butterworth-Heinemann, Elsevier, 2007, pp. 857-933.

[18] L. Bocii and V. Müller, "Mathematic model of three-phase induction machine connected to advanced inverter for traciton system for electric trolley," *Annals of the Brazilian Academy of Sciences,* vol. 85, no. 2, pp. 849-858, 2013.

[19] D. W. Novotny and T. A. Lipo, Vector control and dynamics of AC drives, Oxford, Great Britain: Oxford University Press, 1996.

[20] D. Sumina, "Vektorsko upravljanje - Prostorni vektori, transformacije," Sveučilište u Zagrebu, Fakultet elektrotehnike i računarstva, Zagreb, 2018.

[21] D. Pavković, "Regulacija trofanznog invertera na izmjeničnoj mreži i u sustavu regulacije izmjeničnog servomotora, prezentacija," Sveučilište u Zagrebu, Fakultet strojarstva i brodogradnje, Zagreb, 2018.

[22] N. Perić and J. Matuško, "Upravljanje elektromotornim pogonima, predavanja," Sveučilište u Zagrebu, Fakultet elektrotehinke i računarstva, Zagreb, 2014.

[23] D. Pavković, "Vršni pogon sa serijskim DC motorom, studija," Sveučilište u Zagrebu, Fakultet strojarstva i brodogradnje, Zagreb, 2015.

[24] D. Pavković, J. Deur and A. Lisac, "A torque esitmator-based control strategy for oil-well dril-string torsional vibrations active damping including an auto-tuning algorithm," *Control Engineering Practice,* vol. 19, pp. 836-850, 2011.

[25] D. Pavković, "Projektiranje sustava regulacije brzine vrtnje servopogona s izraženim efektima elastičnosti u prijenosnom mehanizmu. prezentacija," Sveučilište u Zagrebu, Fakultet strojarstva i brodogradnje, Zagreb, 2011.

[26] AVL List GmbH, "Streamline your structure dynamics simulations. AVL EXCITETM.," 27 March 2020. [Online]. Available: https://www.avl.com/web/guest/simulation?uj=2487222&ujName=AVL%20EXCITE%E2%84%A2. [Accessed 27 March 2020].

[27] AVL List GmbH, "4.13.7.2.6. Belt elasticity properties," in *EXCITE Timing Drive Users Guide*, Graz, AVL List GmbH, 2020.

[28] AVL List GmbH, "3.5.1. Connection to MATLAB/Simulink," in *EXCITE Timing Drive Users Guide*, Graz, AVL List GmbH, 2020.

[29] AVL LIst GmbH, "Pioneer. For a new mobility. AVL CRUISE ™ M," 3 April 2020. [Online]. Available: https://www.avl.com/advanced-simulation-technologies ?uj=2499026&ujName=AVL%20CRUISE%E2%84%A2%20M. [Accessed 3 April 2020].